Optical Quartz Crystal Microbalance (OQCM) For Dual-Mode Analysis

by

Zhizheng Zhang

A dissertation submitted in partial fulfillment
of the requirements for the degree of
Doctor of Philosophy
(Electrical Engineering)
in the University of Michigan
2018

Doctoral Committee:

Professor Xudong Fan, Co-Chair
Professor Duncan G. Steel, Co-Chair
Professor Lingjie (Jay) Guo
Professor Jennifer Ogilvie
Professor Herbert Winful

Zhizheng Zhang

zvzhang@umich.edu

ORCID iD: 0000-0003-4048-863X

Acknowledgements

I cannot express enough thanks to my advisors: Prof. Xudong Fan and Prof. Duncan Steel, for the learning opportunities and their support and guidance through my Ph.D. study. My deep appreciation is not only for their rigorous approach to research and valuable advice, but also as caring, kind mentors to help me to become a better scientist.

I am very grateful to Prof. Jay Guo, Prof. Jennifer Ogilvie and Prof. Herbert Winful for serving on my dissertation committee and providing insightful suggestions for my proposal and final defense.

I am also very grateful to Prof. Xiangqun Zeng and Ian Archbold from Oakland University for their help and use of their lab equipment for the device characterization.

Many thanks to the engineers at the Lurie Nanofabrication Facility – Rob Hower, Greg Allion, Dave Sebastian, Nadine Wang, Matt Oonk, Brian Armstrong, Katherine Beach, Shawn Wright, Vishva Ray, Tony Sebastian, Kevin Owen … for helping me through the fabrication process, fixing the machine problems, and many other things.

I would like to express my great appreciation to my colleagues from the Fan Lab (Qiushu Chen, Hongbo Zhu, Menglian Zhou, Xiaotian Tan, Malcolm Khaing Oo, Hengky Chandrahalim, Yu-Cheng Chen, Kyu Hyun Kim, Jiwon Lee …) and from the Quantum Optoelectronics Lab (John Schaibley, Cameron Nelson, Alex Burgers, Adam Katcher, Aaron Ross, Uttam Paudel, Midhat Farooq …). Not only for the many discussions we had or the help on my research, but other small

things – the cordial chats during a long day, the group lunches on Fridays, or the shared snacks (at any time) – that made life more enjoyable through the days, months and years.

My gratitude also goes to my colleagues and friends from the Optical Society at UM, Elizabeth Dreyer, Cheng Zhang, Chengang Ji, Qiaochu Li, Heather Ferguson, Mark Dong ... for their support and friendship.

Last, and the most, I want to thank my parents for your love, guidance, encouragement and support in whatever I pursue and always there for me.

Table of Contents

List of Tables

List of Figures

Abstract

Label-free biosensors allow for real-time measurements of the target molecule, providing valuable kinetic data about the unperturbed biological system. Yet, they generally rely on a single transduction mechanism that reflects a single aspect of a system. In order to have a more complete understanding of the system, many aspects of the system need to be examined simultaneously. An integrated multi-mode label-free sensor capable of providing consistent and complementary information about multiple aspects of a system is highly desirable for biomedical research. Currently there are some hybrid sensors utilizing the optical and quartz crystal microbalance (QCM) techniques to measure both the optical and mechanical properties of a system. However, those hybrid sensors have some shortcomings in implementation and performance that limit their applicability.

In this research, we developed Optical Quartz Crystal Microbalance (OQCM) sensors - hybrid sensors utilizing the same techniques for simultaneously measuring both optical and mechanical properties, which also address these shortcomings. Two OQCM structures were designed, fabricated and explored. The first structure is an interferometric OQCM sensor (I-OQCM) with a multilayer planar optical structure. The interference between reflections at the interfaces between layers generates an interference pattern in the optical spectrum that shifts upon accumulation of additional films on the structure. The second structure is a plasmonically-enhanced grating OQCM sensor (PEG-OQCM). The theory and simulation analyses indicate that

the PEG-OQCM can achieve near zero bulk refractive index sensitivity by optimizing the incidence angle. Simulation results show that at an incident angle of 47 degrees, the bulk RI sensitivity becomes near zero around bulk RI = 1.33. Experimental results for vapor deposition, water and biosensing (solution of streptavidin) match well with the simulation results. With this PEG-OQCM structure, an optical linewidth of 25 nm was obtained in air, 15 nm in water – up to 6 times narrower than that of SPR/LSPR (50-100 nm in water).

The OQCMs were characterized separately to demonstrate the operation in each mode for each structure, and tests were performed to show biosensing capability. Dual-mode tests were conducted for both the I-OQCM and PEG-OQCM to show the capability of simultaneous measurement of both optical and mechanical properties and responses of a system. The test results validate the simulation analyses and correlation between the optical and mechanical responses that would provide corroborating information for more reliable, robust cross-examination/confirmation for the evaluation of test systems.

The OQCM-A sensor with 3 single I-OQCM sensors on a single wafer was also designed, fabricated. Each I-OQCM sensor can be characterized independently of the others. Mechanical response tests performed on the OQCM-A indicate that each sensor responds independently of the other sensors and the cross-talk between on adjacent sensors is negligible.

Chapter 1: Introduction

1.1 Label-free Biosensors

The interactions between different molecular [bio] recognition elements, such as protein-protein interactions, are central to biological processes in living systems. The analysis of these interactions is crucial for understanding biological systems and for developing biotechnologies including microarrays and biosensors to study these systems.

Biosensors generally fall into one of two categories based on their detection mechanism: *label-based detection* and *label-free detection*. Label-based detection relies on the attachment of fluorescent, enzymatic, etc. labels to the target molecules or other recognition elements, and the fluorescence intensity indicates both the target presence and interaction strength between target and biorecognition molecule[1]. Label-free detection, in contrast, leaves the target molecule free of labels or alterations, and able to be detected in its natural form[1].

Labelled sensors have been in use for a long time due to their low limit of detection (LOD), availability of instruments for sensing, and standardized labelling protocols[2]. However, there are several key disadvantages to labelled sensors: (1) labelling is time-consuming and has a higher cost due to the large number of steps required; (2) in addition, label-based sensors cannot be used for real-time detection, and (3) the labels themselves can affect the kinetics of the system under study[3]. For these reasons, much research is being done on the development of label-free sensors.

Label-free sensors allow for real-time measurements of the *unlabeled* target molecule, which provide valuable kinetic data about the unperturbed biological system. Label-free sensing is also relatively less time consuming and less expensive compared to its label-based counterpart due to the smaller number of steps needed.

Label-free biosensors can be classified into five classes[4] based on their transduction mechanism:

- Electrochemical
- Electrical
- Optical
- Piezoelectric (Mechanical)
- Thermal.

In this thesis, the focus will be on **optical** and **mechanical/piezoelectric** sensors per our direction. A brief review of each class is given in the next section.

1.2 Overview of Optical Sensors

Optical sensors rely on the changes in the optical signal that occur upon interaction of the optical field with the system and the environment. These sensors have the advantages of 1) immunity to electromagnetic interference; 2) capability for remote sensing; and 3) ability to perform multiplexed measurements[1, 5]. As a result, optical sensors find wide application in the fields of biomedical research, environmental monitoring, and military field testing. Only label-free optical sensors will be discussed in this thesis.

For optical biosensors, many different structures have been studied and utilized for analyzing biological systems. These structures can be roughly categorized based on the mechanism

used to generate the optical signal: surface plasmon resonance (SPR), interferometry, waveguide, ring resonator, optical fiber and photonic crystals[1]. The sensors developed in this thesis will be based on one or both of the following mechanisms: surface plasmon resonance (with a grating coupler) and interferometry.

1.2.1 Surface Plasmon Resonance (SPR)

A surface plasmon polariton (SPP) is a charge oscillation at the interface of two media with the real parts of the dielectric constant having opposite signs. In natural materials, this occurs between a dielectric and certain metals such as gold, silver, or copper. The wavevector of the SPP at the interface is given by equation (1):

$$\beta_{SP} = k_0 \sqrt{\frac{\varepsilon_{metal}\varepsilon_{Dielec}}{\varepsilon_{metal}+\varepsilon_{Dielec}}} \tag{1}$$

Where ε_{metal} is the dielectric constant of the metal, ε_{Dielec} is the dielectric constant of the dielectric, and k_0 is the wavenumber of the light in vacuum.

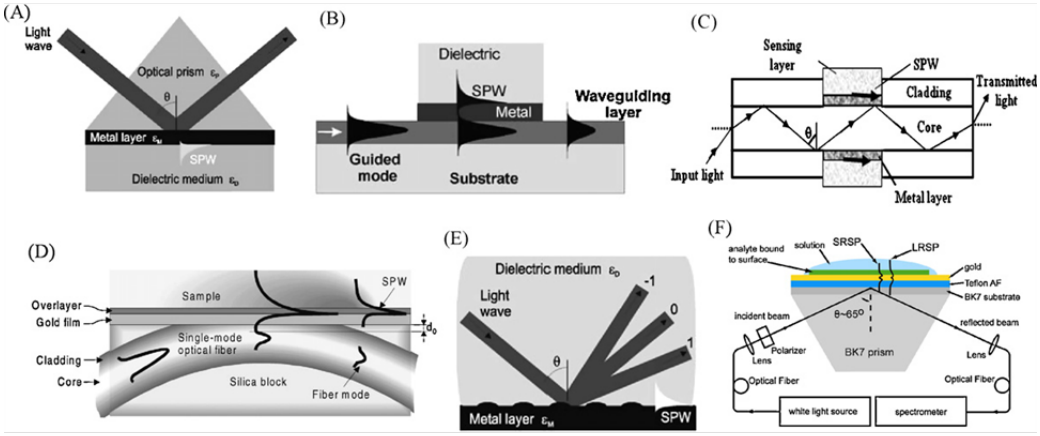

Figure 1-1 SPR sensor coupling configurations[1] – (a) Prism coupling, (b) waveguide coupling, c) optical fiber coupling, (d) side-polished fiber coupling, (e) grating coupling, (f) long-range and short-range surface plasmon

At the resonant wavelength or angle, the parallel component of the wavevector of the incident light on the interface matches that of the SPP. As a result, the light is coupled into the SPP. Coupling into the SPP is usually achieved via one of several methods: prism coupling, waveguide coupling, fiber coupling, or grating coupling[6]. The different methods for coupling to a SPP are shown in Figure 1-1.

Plasmonic devices have been implemented based on the surface plasmon polariton (SPP) in planar devices, or the localized surface plasmon resonance (LSPR), which uses small metal-dielectric nanostructures such as nanospheres or metal nanostructures to amplify the optical response[7, 8].

1.2.2 The Interferometric Sensor

The interferometric sensor relies on the interference of beams between two or more beams from the different interfaces in the optical structure, resulting in an interference spectrum with fringes whose linewidth and wavelength peaks/troughs depend on the thicknesses and refractive indices of the different optical layers in the material.

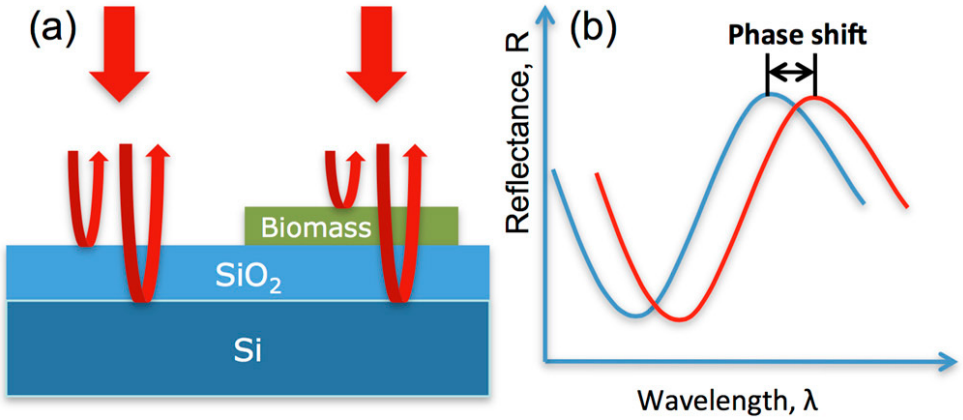

Figure 1-2 Principle of Interferometric Sensor and corresponding intensity spectrum[9]

The simplest interferometric sensor consists of a single optically transparent layer (in the desired wavelength range), which determines the initial interference pattern. The phase difference between the reflected beams changes upon absorption of a thin film, which results in a red shift in the interference spectrum (see Figure 1-2). This technique has been implemented by many research groups (Gao et al. [7], Cheng et al.[10], Avci et al.[9], Özkumur et al.[11] (Figure 1-3) and Hänel et al.[12]).

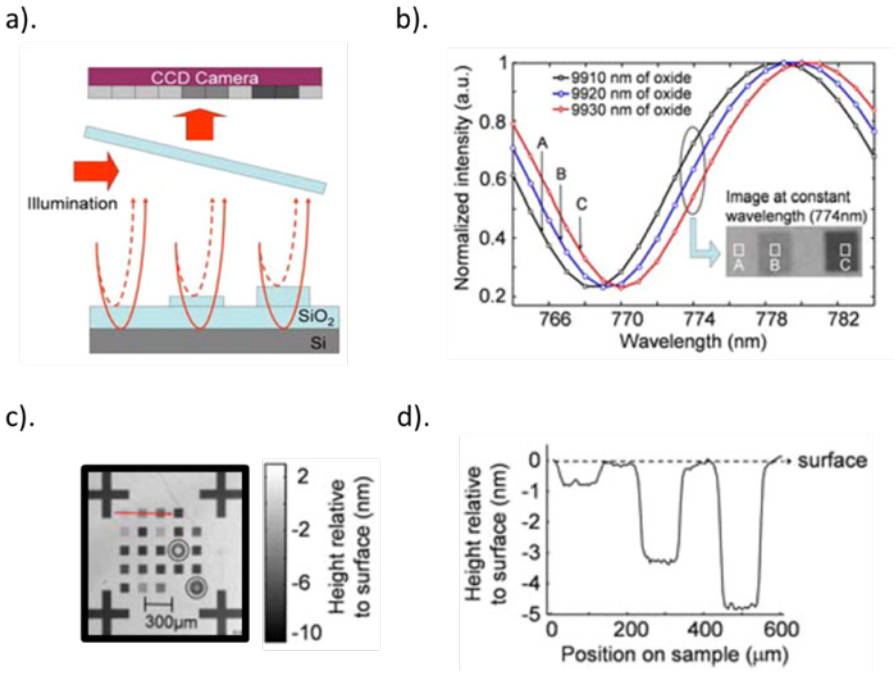

Figure 1-3 Interferometric sensor utilizing a thick SiO2 film to generate the initial interference pattern[11]

1.3 Overview of Mechanical Sensors

Mechanical sensors rely on a change in the mechanical property of the sensor as a result of changes in its environment (e.g. adsorbed layer or bulk medium). To monitor the property change, the sensor material is usually chosen to be a piezoelectric material that exhibits mechanical oscillation due to an applied electric field, and vice versa via electromechanical coupling. A change

in the adsorbed mass or bulk medium results in a change in the mechanical response which is converted to an equivalent electrical response via the piezoelectric effect.

1.3.1 Types of Mechanical Label-Free Sensors

Mechanical label-free sensors generally belong to one of two categories: cantilever-based or resonator-based:

The **cantilever-based sensors**[13] are partly-suspended structures, fixed at one end, which oscillate at a frequency determined by the device parameters. Accumulation of mass or change in the viscosity of the bulk medium results in a change in the oscillation frequency. Since the sensor oscillates vertically, this type of sensor is heavily damped in liquid, and as a result, generally is not as suitable for real-time mechanical sensing.

The **resonator-based sensors** fall into one of 4 subcategories – surface acoustic wave (SAW), acoustic plate mode (APM), flexural plate mode (FPM), and quartz crystal microbalance (QCM) [14]. All four subcategories of resonator-based sensors rely on the crystal being driven by two electrodes and resonating at an oscillation frequency determined by the device parameters. The QCM is chosen as the mechanical sensor for this work due to its robustness, availability, and affordable electronics, as well as suitability for a liquid environment for real-time biosensing.

1.3.2 The Quartz Crystal Microbalance Sensor

The quartz crystal microbalance is a mass sensor based on the piezoelectric effect [15] , which converts the mass of the analyte into an electrical signal. An alternating electric field is applied via electrodes on both sides of a quartz wafer, generating a mechanical oscillation in the thickness shear mode (TSM) [16], a transverse mechanical wave with the propagation vector normal to the crystal surface. An AT-cut quartz crystal (35° to the optical axis) is usually chosen for its high

frequency stability ($\frac{\Delta f}{f} \approx 10^{-8}$) and a temperature coefficient of near zero in the 0-50°C range. A photograph of a QCM sensor from Inficon EDC is shown in Figure 1-4.

Due to the electromechanical coupling resulting from the piezoelectric effect, the electrical characteristics of the QCM are affected by mechanical changes arising from interactions between the QCM and any media in contact with the QCM. The electrical admittance/impedance is the characteristic most often chosen for monitoring the QCM frequency response[17].

Figure 1-4 A photograph of a QCM sensor from Inficon EDC

The behavior and characteristics of the QCM crystal are usually described using the Butterworth-Van-Dyke (BVD) model, an equivalent circuit model consisting of an electrical and a mechanical arm. The electrical arm has a static capacitance $\mathbf{C_0}$, while the mechanical arm contains three elements: a mechanical capacitance $\mathbf{C_1}$, inductance $\mathbf{L_1}$, and resistance $\mathbf{R_1}$, which are

given by the equations from Martin et al[17] and depend on the QCM device area, crystal thickness and peak oscillation frequency.

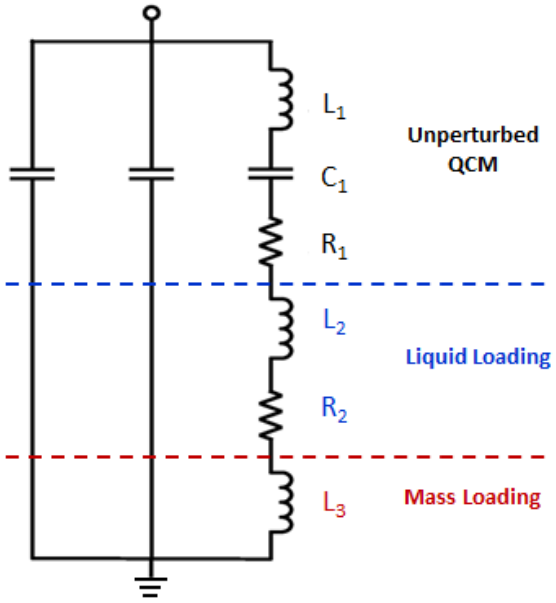

Figure 1-5 Modified Butterworth-Van Dyke (BVD) equivalent circuit[17]

The effect of mass (rigid) and liquid loading on the QCM can be modelled[17] by the addition of 3 electrical elements to the unperturbed BVD circuit: **L_2, R_2** and **L_3** (Figure 1-5). **L_2** and **R_2** model the liquid loading effect and are functions of the density-viscosity product of the liquid, as well as the original device parameters **C_1, L_1,** and **R_1**[17]. **L_3** models the accumulation of rigid mass on the QCM wafer as a function of the film density.

For small mass and liquid loading (**$L_2 + L_3 << L_1$**), the change in frequency can be written as a function of the mass and liquid properties and crystal resonant frequency, and is given by equation (2)[17]

$$\Delta f_s \approx -\frac{2f_s^2}{N\sqrt{\bar{c}_{66}\rho_q}}\left[\rho_s + \left(\frac{\rho\eta}{4\pi f_s}\right)^{\frac{1}{2}}\right] \quad (2)$$

Where ρ_s is the solid layer density, f_s the QCM resonant frequency, N the overtone number,Δm the total change in mass, ρ the liquid density, η the liquid viscosity, and A the electrode area.

The first term on the RHS is equivalent to the Sauerbrey equation for the change in resonance frequency (equation (3)) due to accumulation of a thin rigid film onto the QCM sensing surface:

$$\Delta f_s \approx -\frac{2f_s^2\rho_s}{N\sqrt{\bar{c}_{66}\rho_q}} = -\frac{2f_s^2}{N\sqrt{\bar{c}_{66}\rho_q}}\frac{\Delta m}{A} \tag{3}$$

The second term in equation 2 gives the effect of liquid loading on the QCM crystal as a function of the density viscosity product $\rho\eta$. The effect of solid and liquid loading on the equivalent BVD circuit is depicted in Figure 1-5. The assumption for this model is that the solid film is very thin and rigidly attached to the QCM[17]. For viscoelastic films of greater thickness, an extended model is given in Arnau et al[18].

The piezoelectric parameters of AT-cut quartz, used to calculate the expected mechanical response of the OQCM, are listed below[17].

Table 1-1 Properties of AT-Cut Quartz

	Property	**Value**
ρ_q	Density	2.651 g/cm^3
$\bar{c}_{66}$	Piezoelectric constant	2.947 × 10^{11} dyne/cm^2
K^2	Coupling constant	7.74 × 10^{-3}
η_q	Stiffness	3.5 × 10^{-3} g/(cm s)
ρ_η	Shear modulus	2.947 × 10^{11} g/cm^{1}s^2

1.4 Optical vs. QCM Based Sensors: A Comparison

Optical and QCM sensors can be used individually to extract different sets of properties [19-21] of a material or system. A comparison of the two techniques, especially the types of data that can be extracted, is listed in Table 1-2 below.

Table 1-2 Comparison between Optical and QCM Measurements

	Optical Measurement	Quartz Crystal Measurement
Operating Frequency	Order of 10^{14} Hz	10^{0}-10^{2} MHz (fundamental frequency)
Measured Signal	Measurement of the change in optical response (reflection, transmission, etc.) of the system	Measurement of the change in the piezoelectric response (impedance, conductance, etc.) of the system
Data which can be extracted	• Film thickness • Film uniformity • "Dry" mass • Index of refraction	• Total film mass • Film density • "Wet" mass – including bulk • Film viscosity
Advantages	• Can be designed to be insensitive to either surface or bulk RI • Completely non-contact	• Higher sensitivity to strong specific binding • Can measure mass directly
Disadvantages	• Measures RI change at surface, does not measure direct mass change • Sensitive to non-specific binding	• Mass measured includes any trapped bulk solution • Sensitivity dependent on film position

The comparison clearly shows 2 key facts:

- Both methods are independent of each other as each has its own significantly different operating frequencies;
- Each method on its own can extract only a certain subset of data.

1.5 Motivation for Developing the Optical Quartz Crystal Microbalance

While label-free sensors allow for real-time monitoring of the biological system under study, they generally rely on a single transduction mechanism (optical, mechanical, etc.), which yields information on only a single aspect of the system. This information may be insufficient and could lead to erroneous conclusions. In order to obtain an accurate picture of the system, multiple aspects need to be examined simultaneously [19, 22-27]. An integrated multi-mode label-free sensor capable of providing consistent and complementary information about bio-interactions is therefore highly desirable for fundamental and applied biomedical research. For this purpose, the optical quartz crystal microbalance (OQCM) is developed in this thesis in order to provide complementary information on the **optical** and **mechanical** properties of a biological system on a single sensor.

1.6 Thesis Roadmap

In this thesis, we designed, fabricated, characterized, tested and analyzed the performance of two different OQCM sensors for dual-mode detection. Chapter 2 gives an overview of previous work done on optical/quartz crystal microbalance hybrid sensors and describes the general structure of the optical quartz crystal microbalance (OQCM) devices. Chapter 3 and Chapter 4 each focus on one type of OQCM device developed in the course of the research. Chapter 3 focuses on the interferometric OQCM (I-OQCM) structure, including the underlying theory, fabrication, characterization and testing of this structure. Chapter 4 focuses on the plasmonic-enhanced grating-based OQCM (PEG-OQCM) structure, designed to address the issue of separating the effects of bulk and surface sensing, and the theory, fabrication, characterization and testing of the PEG-OQCM structure. Chapter 5 discusses the OQCM array, which expands upon the structure

presented in Chapter 3 by integrating 3 of the I-OQCM structures onto a single QCM wafer for multiplexed detection. The design, structure and cross-talk results are presented in this chapter. Finally, Chapter 6 concludes this thesis with a short summary and future directions for this research.

Chapter 2: Optical Quartz Crystal Microbalance – Structure and Principles

2.1 Overview of Optical/QCM Hybrid Sensors

Several hybrid sensors have been developed that combine the QCM sensor with various optical structures for simultaneous optical and mechanical measurements of a system. Those optical/QCM hybrid sensors have utilized **S**urface **P**lasmon **R**esonance (SPR), **O**ptical **W**ave**g**uide (OWG), Reflectometry/Ellipsometry, and Microscopy as the optical sensing method.

2.1.1 Surface Plasmon Based Hybrid Sensors

Shinbo et al. designed a hybrid sensor based on a combination of QCM and SPR[28], which used silver as the electrode material, and a polymer film coating for moisture absorption. This implementation relied on coupling via the side of the wafer into the quartz crystal to excite the surface plasmon (Figure 2-1, right side).

The more common implementation is to etch a corrugation grating into the quartz crystal to couple the incident light into the surface plasmon mode (Plunkett et al.[29], Bund et al.[30], Zong et al.[31], Laschitsch et. al [32] and Bailey et al.[33]). One example is shown in Figure 2-1. The optical sensor response was monitored using angular interrogation in each of these cases.

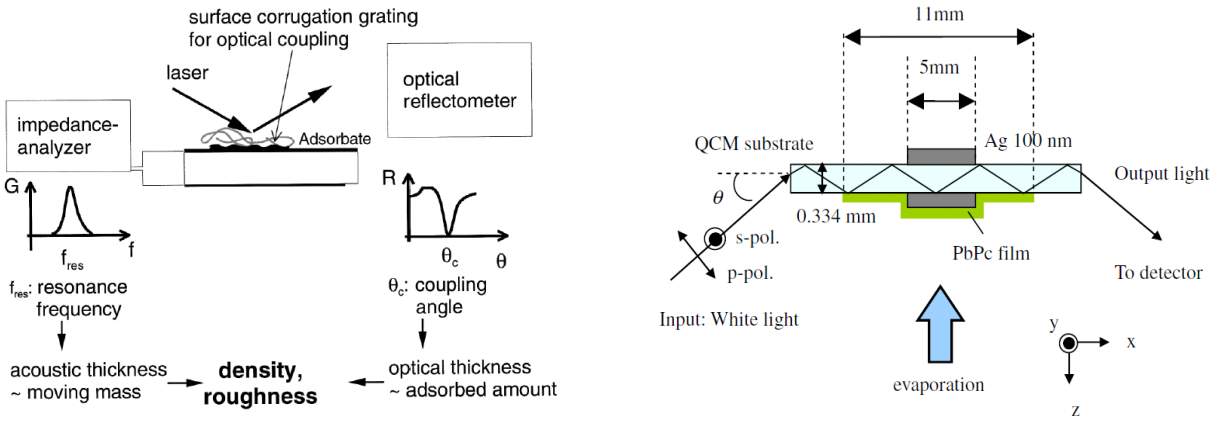

Figure 2-1 Two surface plasmon resonance-based optical/QCM hybrid sensors. Left: a grating-coupled SPR hybrid sensor[32]. Right: a side-coupled SPR hybrid sensor[28]

Grab et al.[34] and Zhu et al.[35] took a different approach and used localized surface plasmon resonance (LSPR) to fabricate LSPR-based hybrid sensors that do not require prism coupling or grating coupling. The optical/QCM hybrid sensor (Figure 2-2, left side) by Grab et al.[34] is made of gold-plated polystyrene core-shell structures self-assembled onto a gold electrode QCM wafer for simultaneous optical and mechanical detection of fibrinogen absorption to determine the solvent content in thin adsorbed layers. Zhu et al.[35] took a different approach and fabricated gold nanorings on a transparent ITO electrode (Figure 2-2, right side), which allowed for measuring the optical spectrum in transmission mode.

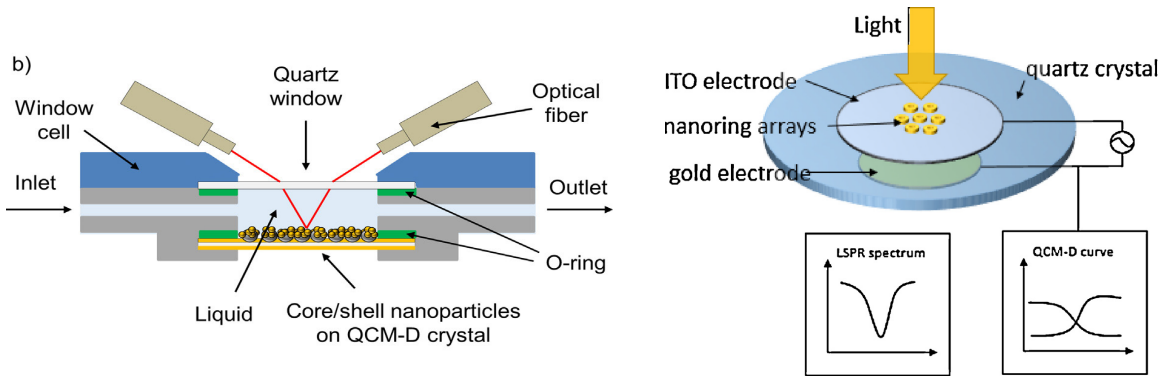

Figure 2-2 LSPR-based hybrid sensors. Left: Core-shell nanoparticle based LSPR hybrid sensor[34]. Right: Nanoring based LSPR hybrid sensor [35]

2.1.2 Optical Waveguide Based Hybrid Sensors

Shinbo et al. also designed a hybrid sensor based on optical waveguide spectroscopy[36, 37]. Their OWG-based sensor used a similar base QCM structure to that of their SPR-based hybrid sensor (differing only in electrode thicknesses and polymer coatings) and was used to monitor the evaporation of lead phthalocyanine. Another two OWG-based sensors[37] were designed by the same group, and used QCMs with gold electrodes. The first configuration consisted of a bilayer of fluorinated polyimides (on top of the electrode) with different refractive indices, which served as the optical waveguide. A prism was placed in contact with the QCM and used to couple light into the slab waveguide. The second configuration consisted of a grating core, which formed a ridge waveguide. These sensors (Figure 2-3) were used for humidity and vapor sensing.

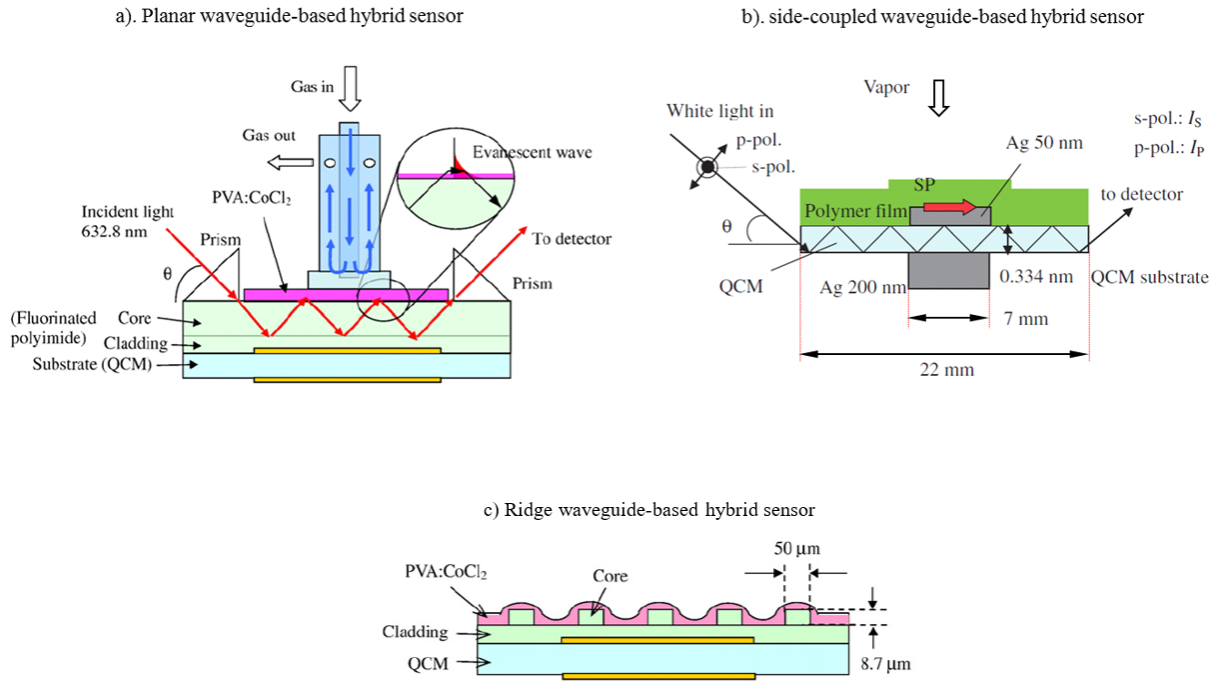

Figure 2-3 Three optical waveguide-based optical/QCM hybrid sensors. Top Left: Planar waveguide-based hybrid sensor[37]. Top Right: Side-coupled waveguide-based hybrid sensor[36]. Bottom: Ridge waveguide-based hybrid sensor[37]

2.1.3 Reflectometry/Ellipsometry Based Hybrid Sensors

Optical reflectometry is a technique in which incident light is reflected off a sample, and the properties of the reflected light are used to characterize the sample. An example of the intensity spectrum generated for increasing film thickness is shown in Figure 2-4. Ellipsometry is a type of reflectometry which measures the change in polarization as light is reflected from a sample. The amplitude ratio Ψ and phase difference Δ of the reflected TE and TM polarized light are measured and used to determine the properties (such as film thickness and refractive index) of the sample[38-44]. The principle of ellipsometry is shown in Figure 2-5.

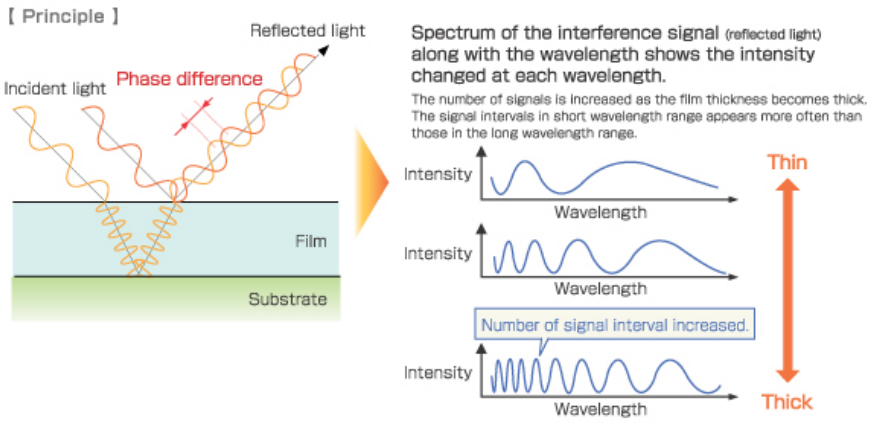

Figure 2-4 Reflectometric measurement from an interference layer and resulting reflectance spectrum[45]

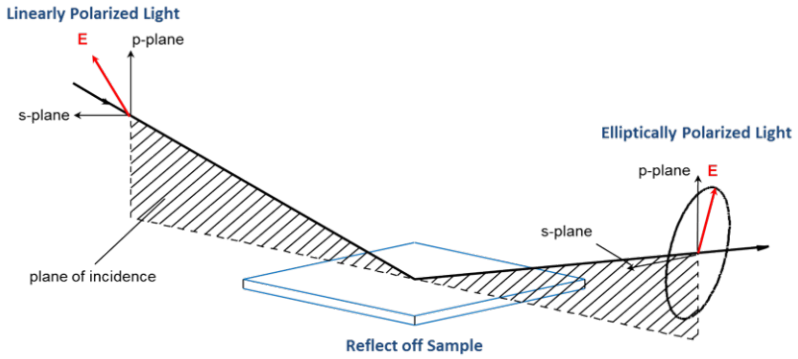

Figure 2-5 Principle of ellipsometry[46]

Rodenhausen et al[38, 39] reported a combinatorial approach using in-situ spectroscopic ellipsometry and quartz crystal microbalance methods to study the formation of ultra-thin organic films. Kananizadeh et al.[47] uses generalized ellipsometry on an unmodified gold electrode QCM to determine the thickness of the absorbed film. Edvardsson et al.[48], Guleryuz et al.[49], and Buron et al.[50] use reflectometry to monitor various layer formation processes. Figure 2-6 shows their initial setup and later modified setup, which utilized a reference beam to correct for material deposited at the prism-liquid interface.

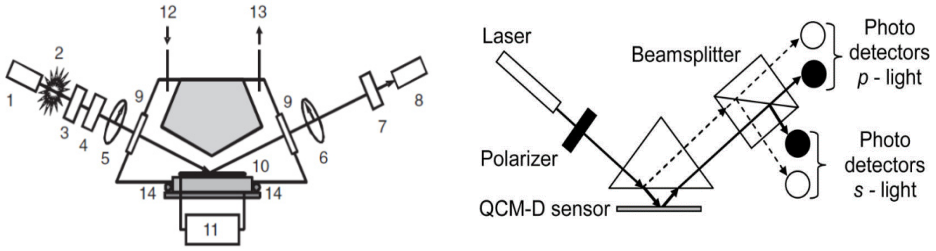

Figure 2-6 Reflectometric and ellipsometric hybrid sensors. Left: Setup for QCM/ellipsometry measurement[39]. Right: Setup for reflectometry hybrid sensor[48].

2.1.4 Optical Microscopy Based Hybrid Sensor

Optical microscopy is a technique where incident light on a sample is modified by a system of lenses to provide a magnified image of the sample surface. Microscopy allows for the full sample surface to be imaged, limited only by the field of view of the system.

Niri et al. utilized a bare gold-coated QCM crystal to monitor the electroformation of phospholipid vesicles[51] by simultaneous optical microscopy and quartz microbalance techniques through an ITO-coated glass window. While the imaging was performed in real time, the film thickness measurements were performed via AFM outside of the optical setup, and not in real time. Their setup and the resulting QCM response and AFM images are shown in Figure 2-7.

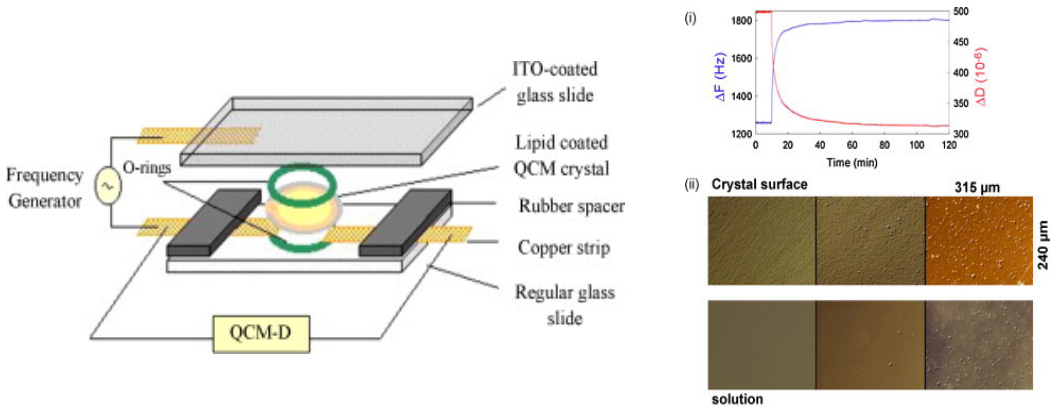

Figure 2-7 Optical microscopy-based sensor[51]

2.2 Motivation for the OQCM Structure

Though each of the structures described in section 2.1 has its own set of advantages, each also has its own set of shortcomings, as discussed below.

2.2.1 Issues with Current Hybrid Sensors

For the **SPR-based hybrid sensors**, coupling to the plasmon is achieved via one of two methods. The first involves placing a prism in contact with the quartz crystal, which can affect the mechanical performance. The second method involves etching a grating into the quartz crystal to phase match the incident light to the surface plasmon mode. This irreversibly changes the crystal and renders it unusable outside of the grating-coupled SPR application. Also, by relying on simple SPR, there is limited room to optimize the optical performance of the device.

In the case of the **LSPR sensor**, the core-shell structures are placed on the surface via self-assembly. It is indicated in the paper that only in the case of complete homogeneous coverage were they able to achieve stable operation of their structure. Also, the polystyrene core-shell structures

still underwent structural changes during the 2-hour stabilization procedure, which is attributed to water penetration[34] into the cavities between the nanoparticles and swelling of the beads upon contact with water.

The **OWG based hybrid sensor** has the same issue as the prism-coupled SPR sensor – the prism in contact with the crystal will affect the mechanical oscillations. Also, the grating structure used in the ridge waveguide device by Shinbo et al.[37] is very deep, potentially leading to large damping issues in liquid.

The **reflectometry/ellipsometry structures** (such as those by Edvardsson et al.[48]) use a gold electrode QCM crystal with no optical structure or an extremely thin coating layer. This makes the interference fringes very shallow due to the large difference in amplitude between the reflection of the gold electrode and the reflection off the detected film.

The **optical microscopy structure** (by Niri et al.[51]) suffers from the same issue as the reflectometry/ellipsometry structures – the absence of 1) a blocking layer to block metallic reflections, and 2) a thicker interference film result in a low contrast optical spectrum.

2.2.2 The Optical Quartz Crystal Microbalance

The Optical Quartz Crystal Microbalance (OQCM) developed in this thesis will seek to address the issues of the above optical/QCM hybrid devices:

First, the quartz wafer of our OQCM does not undergo any modifications – all electrodes and sensing structures will be fabricated on top of a standard wafer with no features etched into the crystal. This ensures that 1) the oscillation of the crystal is not impacted by the crystal mechanical structure; 2) the crystal can be reused more easily since the mechanical structure of the

crystal is not permanently modified. As a result, the OQCM optical structure can be optimized independently of the QCM wafer itself.

Second, the OQCM optical structure is designed for top-side optical interrogation. This allows for monitoring of the distribution of binding material on the sensing surface. This is important since the mechanical frequency response of the QCM is dependent on the surface uniformity of the binding material and bulk medium, but this information cannot be directly extracted from the QCM response by itself.

Furthermore, the OQCM structure can be configured for multiplexed sensing, which cannot be easily implemented for some of the current optical hybrid sensors, especially those in the waveguide configuration.

2.3 OQCM Device for Multi-Mode Analysis

2.3.1 Single Sensor OQCM for Multi-Modal Analysis

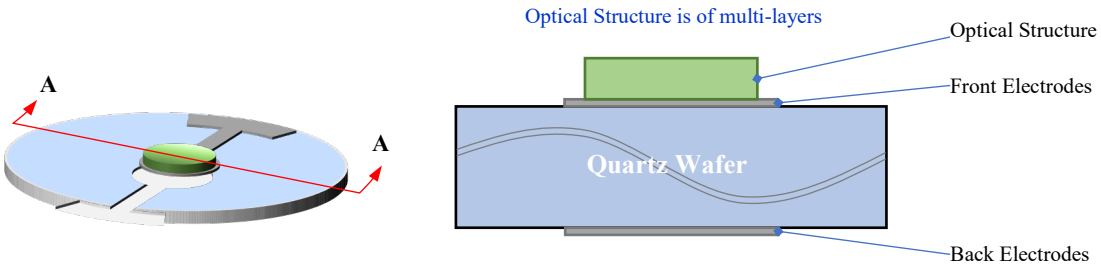

Figure 2-8 General structure of the OQCM

The general OQCM structure we developed is shown in Figure 2-8. The structure consists of a 185 μm thick AT-cut quartz wafer (corresponding to 9 MHz operating frequency). On the top

and bottom surfaces are patterned electrodes. For the structures in this thesis, tantalum is used for the first structure (to reduce metal reflection) and gold for the second (to generate plasmons). An optical structure is fabricated in the center region where the sensing occurs.

Other factors to consider when selecting the appropriate optical structure for the OQCM include the following:

- Total mass – for the mechanical response to remain within the linear regime, the accumulated mass on the OQCM sensor must be less than 2 percent of the total OQCM mass.
- Material viscosity – non-rigidly bound films introduce additional damping into the system.
- Film stress – high-stress films are more susceptible to being peeled off. Adhesion layers must be included to prevent this

In Chapters 3 and 4, the details of the two OQCM structures (the I-OQCM and PEG-OQCM) will be discussed further.

2.3.2 The OQCM Array

One of the advantages of using an optical technique is the capability to monitor multiple sensing areas using a single detector. This has already been exploited in different types of optical sensors, such as interferometric reflectance imaging sensors (IRIS)[9, 10, 52], surface plasmon resonance imaging sensors (SPRi)[7, 53-55], photonic crystal imaging[56], including resonant waveguide gratings (RWG)[57, 58].

The OQCM array seeks to utilize this capability to enable optical imaging of the sample. This provides two additional capabilities not present in the previously described structures. The

presence of multiple sensing areas allows for multiplexed detection. In Chapter 5, an OQCM array consisting of multiple interferometric OQCMs on a single chip is further discussed and tested.

2.4 Summary

We have further reviewed the research works on the Optical/QCM hybrid sensors, especially on the SPR/LSPR, OWG and Reflectometry/Ellipsometry based hybrid devices. Though each of the optical sensing methods has its advantages, but also has its own deficiencies – such as no optical structure, etching a grating into the quartz crystal, having prism in contact with the crystal, etc. A new OQCM concept and the basic structure are presented in this chapter. The OQCMs seek to maintain the positives from the current Optical/QCM hybrid devices while to address their shortcomings. The optical structure of our OQCM does not modify the quartz wafer, so the OQCM optical structure can be optimized independently of the QCM wafer which would lead to better layer design possible. The OQCM optical structure is also designed for top-side optical interrogation. This allows for monitoring of the distribution of binding material on the sensing surface to provide better signal. More details on the two specific OQCM devices will be discussed in Chapter 3 and Chapter 4.

Chapter 3: Optical Quartz Crystal Microbalance Structure 1 – Interferometric OQCM Sensor

3.1 Motivation for the Interferometric OQCM Sensor

The interferometric sensor relies on the interference between reflected [transmitted] beams to generate fringes in the optical spectrum. These fringes can be measured using similar techniques as those used in reflectometry.

In Chapter 2, several reflectometry and ellipsometry based optical/QCM hybrid sensors were discussed. These sensors utilized either a bare quartz crystal or one with a thin sensing film. Due to the high reflectance from the metal electrode (usually gold), the contrast in fringes formed by the reflected beams from the protein-bulk and metal-protein interfaces is very low, especially in liquid. Also, the protein thickness is usually on the order of single nm to a couple 10s of nm. For a single dielectric film of thickness $\boldsymbol{h}$, the wavelengths at which extrema occur in the reflection spectra are given[59] by equation (4):

$$\boldsymbol{h} = \frac{m\lambda_0}{4\cos\theta_{film}} \rightarrow m\lambda_0 = 4h\cos\theta_{film}, m \in Z \tag{4}$$

Where m is the fringe order, θ_{film} is the incidence angle in the film, and λ_0 is the wavelength of light. For a protein film with small $\boldsymbol{h}$, there are no extrema in the UV to IR range resulting from the protein itself. These two factors make it more difficult to detect the spectral or intensity shift indicative of a change in protein thickness.

The interferometric OQCM (I-OQCM) we developed seeks to address both of these issues by (1) including a blocking layer between the electrode and interferometric layers to minimize reflections from the metal electrode, and (2) including a thicker interferometric layer (a few hundreds of nanometers or larger) to reduce the linewidth, and (3) including higher refractive index (RI) layers to increase the reflection contrast in liquid. These help to set a baseline optical spectrum where a change due to thin film thickness changes is much easier to detect.

3.2 Device Structure

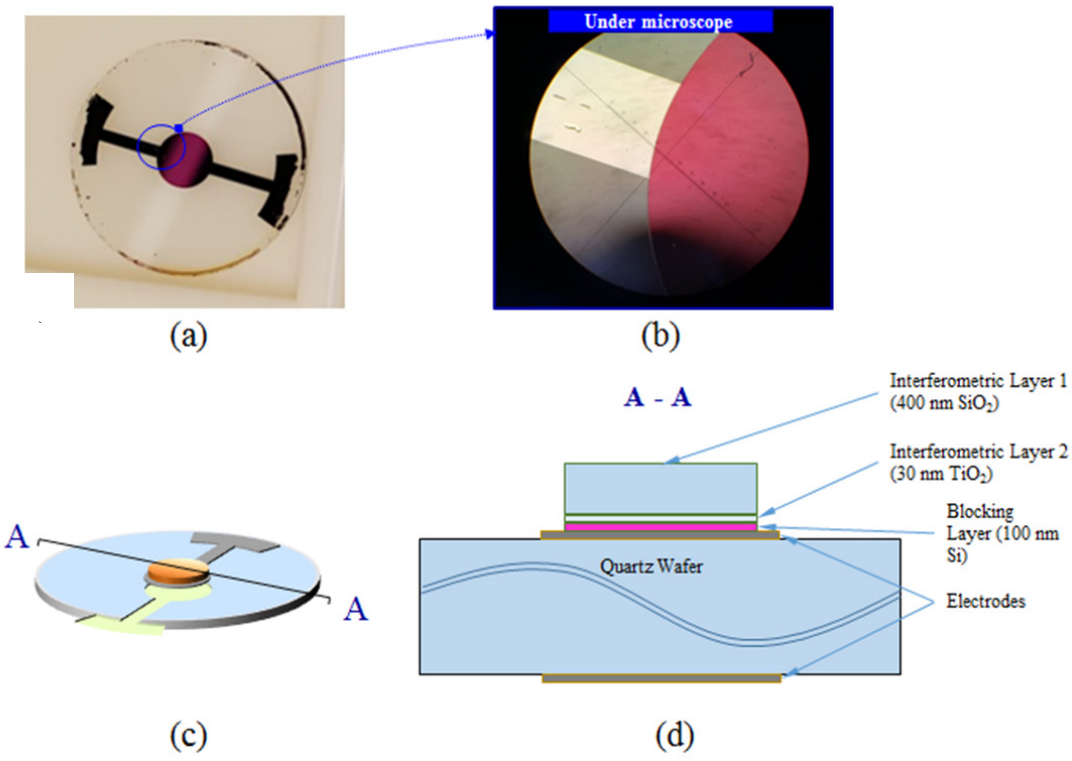

Figure 3-1 Interferometric OQCM (I-OQCM) Structure. a) photograph of I-OQCM prior to wire bonding; b) microscope image of sensing area and electrode c) 3-D schematic of interferometric OQCM; d) cross-sectional view of OQCM showing interferometric and blocking layers

The optical structure used for the I-OQCM sensor is a multiple-beam interference planar structure. The electrode of this sensor was chosen to be tantalum for its low reflectivity as compared to the standard gold electrode. On top of the sensing area is a 100-nm thick p-doped silicon film (with 10 nm titanium adhesion layer) to block reflections from the underlying electrode. The interferometric structure is formed with a 400 nm SiO_2 (n = 1.46) /30 nm TiO_2 (n = 2.30) bilayer on top of the Si blocking layer.

3.3 Theory and Simulation Results

For 1D multilayer structures, the characteristic matrix technique is often used to calculate the response at the output of the structure for a given incident plane wave. Each layer is described by a characteristic matrix (called a transfer matrix in some literature). The characteristic matrices are multiplied together in the order of the layers to generate a characteristic matrix for the entire structure, whose elements can be used to calculate the amplitudes of the reflected and transmitted waves. The theory of the characteristic matrix technique[59] is described in Section 3.3.1.

3.3.1 Theory

The characteristic matrix for a single homogenous thin film of thickness z is given by equation (5):

$$M(z) = \begin{cases} \begin{bmatrix} \cos(k_0 nz\cos\theta) & -\frac{i}{p}\sin(k_0 nz\cos\theta) \\ -ip\sin(k_0 nz\cos\theta) & \cos(k_0 nz\,cos\,\theta) \end{bmatrix}, & p = \sqrt{\frac{\varepsilon}{\mu}}\cos\theta \;\; (TE) \\ \begin{bmatrix} \cos(k_0 nz\cos\theta) & -\frac{i}{q}\sin(k_0 nz\cos\theta) \\ -iq\sin(k_0 nz\cos\theta) & \cos(k_0 nz\,cos\,\theta) \end{bmatrix}, & q = \sqrt{\frac{\mu}{\varepsilon}}\cos\theta \;\; (TM) \end{cases} \quad (5)$$

For a medium composed of a succession of stratified media extending from $z_0 = 0 \leq z_1, z_1 \leq z_2, \ldots, z_{N-1} \leq z_N$, the characteristic matrix for the medium[59] is given by equation (6), with $M(z_N)$ given by equation (7).

$$Q_0 = M_{tot} Q(z_N) \tag{6}$$

$$M(z_N) = \prod_{i=1}^{N} M_i(z_i - z_{i-1}) \tag{7}$$

Where Q_0 is the vector of electric and magnetic field amplitudes at z = 0, $Q(z_N)$ is the vector of field amplitudes at $z = z_N$, and $M(z_N)$ is the characteristic matrix for the entire thin film structure.

The reflection coefficient of the film structure is given[59] by equation (8) below for a TE wave:

$$r = \frac{(m'_{11} + m'_{12} p_l) p_1 - (m'_{21} + m'_{22} p_l)}{(m'_{11} + m'_{12} p_l) p_1 + (m'_{21} + m'_{22} p_l)} \tag{8}$$

Where m'_{ij} are the elements of the characteristic matrix of the medium:

$$p_1 = \sqrt{\frac{\varepsilon_1}{\mu_1}} \cos\theta_1 \qquad \text{(for the incident medium)}$$

$$p_l = \sqrt{\frac{\varepsilon_l}{\mu_l}} \cos\theta_l \qquad \text{(for the exit medium)}$$

For a TM wave, the reflection coefficient is given by equation (9):

$$r = \frac{(m'_{11} + m'_{12} p_l) p_1 - (m'_{21} + m'_{22} p_l)}{(m'_{11} + m'_{12} p_l) p_1 + (m'_{21} + m'_{22} p_l)} \tag{9}$$

Where:

$$q_1 = \sqrt{\frac{\mu_1}{\varepsilon_1}}\cos\theta_1 \qquad \text{(for the incident medium)}$$

$$q_l = \sqrt{\frac{\mu_l}{\varepsilon_l}}\cos\theta_l \qquad \text{(for the exit medium)}$$

3.3.2 Simulation Results

For the device structure in this chapter, the characteristic matrix for the I-OQCM is given by equation (10):

$$M_{tot} = M_{SiO_2} M_{TiO_2} M_{Si} M_{Ti} \tag{10}$$

The physical model used for the calculation is shown in Figure 3-2. The calculated reflection spectra are shown in Figure 3-3. The incident medium is either air (refractive index (RI) = 1.00) or deionized (DI) water (RI = 1.33). The refractive index data for the Si was measured using a Woollam 2000 Ellipsometer, and the data for tantalum was obtained from Werner et al. [60]

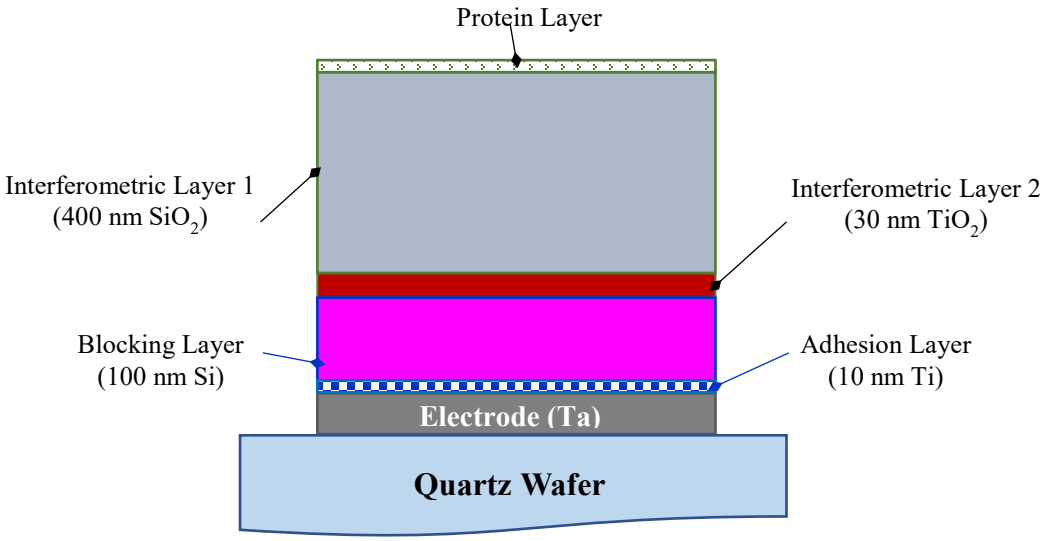

Figure 3-2 Model used for characteristic matrix calculation of reflection spectra for interferometric OQCM sensor

The reflection coefficients of this structure (before any additional thin film deposition) are calculated using the transfer matrix technique[59]. The parameters used in the calculation are listed in Table 3-1.

Table 3-1 Optical and Physical Properties of the Materials Used in the Interferometric OQCM

	Density (g/cm^3)	Index of Refraction n	Thickness z (nm)
SiO_2	**2.20**	**1.46**	**400**
TiO_2	**3.78**	**2.30**	**30**
Si	**2.33**	Dependent on wavelength	**100**
Ti	**4.51**	Dependent on wavelength	**10**

Figure 3-3 shows the calculated reflection spectra of the I-OQCM in air (RI = 1.00) and water (RI = 1.33) at three different incidence angles. The wavelengths at which the reflectance peaks shift towards shorter wavelength with increasing incidence angle, as expected from equation (4). Note that the fringe contrast is decreased significantly in DI water due to the reduced refractive index difference between the SiO_2 layer and the bulk medium. This is explained by the following theory. For two beams with field amplitudes E_1 and E_2 and phase difference ϕ, the intensity of the beam resulting from the interference between them is given by equation (11):

$$\left|E_1 + E_2 e^{i\phi}\right|^2 = |E_1|^2 + |E_2|^2 + 2E_1E_2\cos\phi \tag{11}$$

The third (interference) term determines the fringe contrast for changing phase differences and is dependent on the product of the amplitude between the two beams. This term is maximized when $E_1 = E_2$. With the reduced beam amplitude from the SiO2/bulk medium interface while the beam

from the TiO2/Si layer is increased, the product term is reduced substantially, resulting in a decreased fringe contrast.

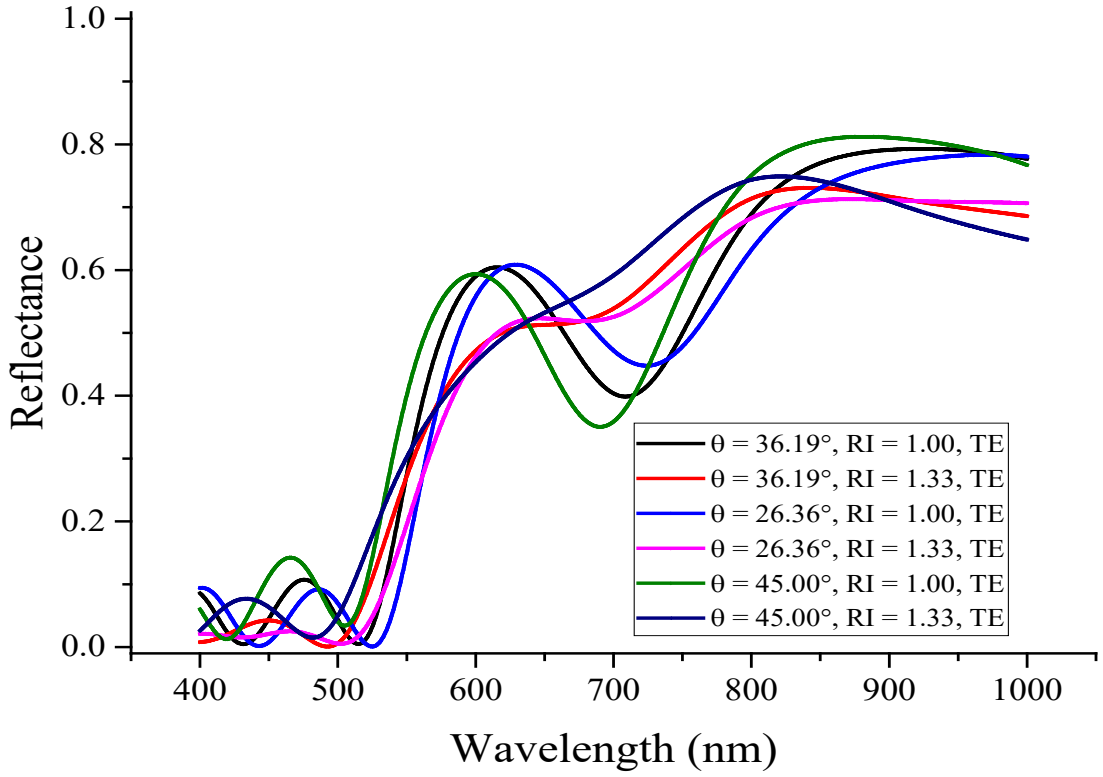

Figure 3-3 Calculated spectra of the interferometric OQCM in air (RI = 1.00) and in DI Water (RI = 1.33) using equations (5) to (7). The properties of the SiO_2 and TiO_2 films used for the calculation are listed in Table 3 and were measured experimentally using a Woollam 2000 Ellipsometer. Given a specific interferometric structure, it is clear that when in DI water (RI = 1.33), the fringe contrast is greatly reduced due to the smaller refractive index difference between the interferometric layer and the bulk medium.

The calculated reflection spectra of the I-OQCM in air (RI = 1.00) for increasing protein (n = 1.51) thickness are shown in Figure 3-4. As the protein thickness is increased, the spectrum shifts toward longer wavelengths due to the increasing phase difference between the reflected beams at the interferometric layer and blocking layer interfaces. Note that the fringe contrast is reduced past 650 nm due to reduced absorption by the Si blocking layer at longer wavelengths, but fringes in the interference spectra are clearly visible.

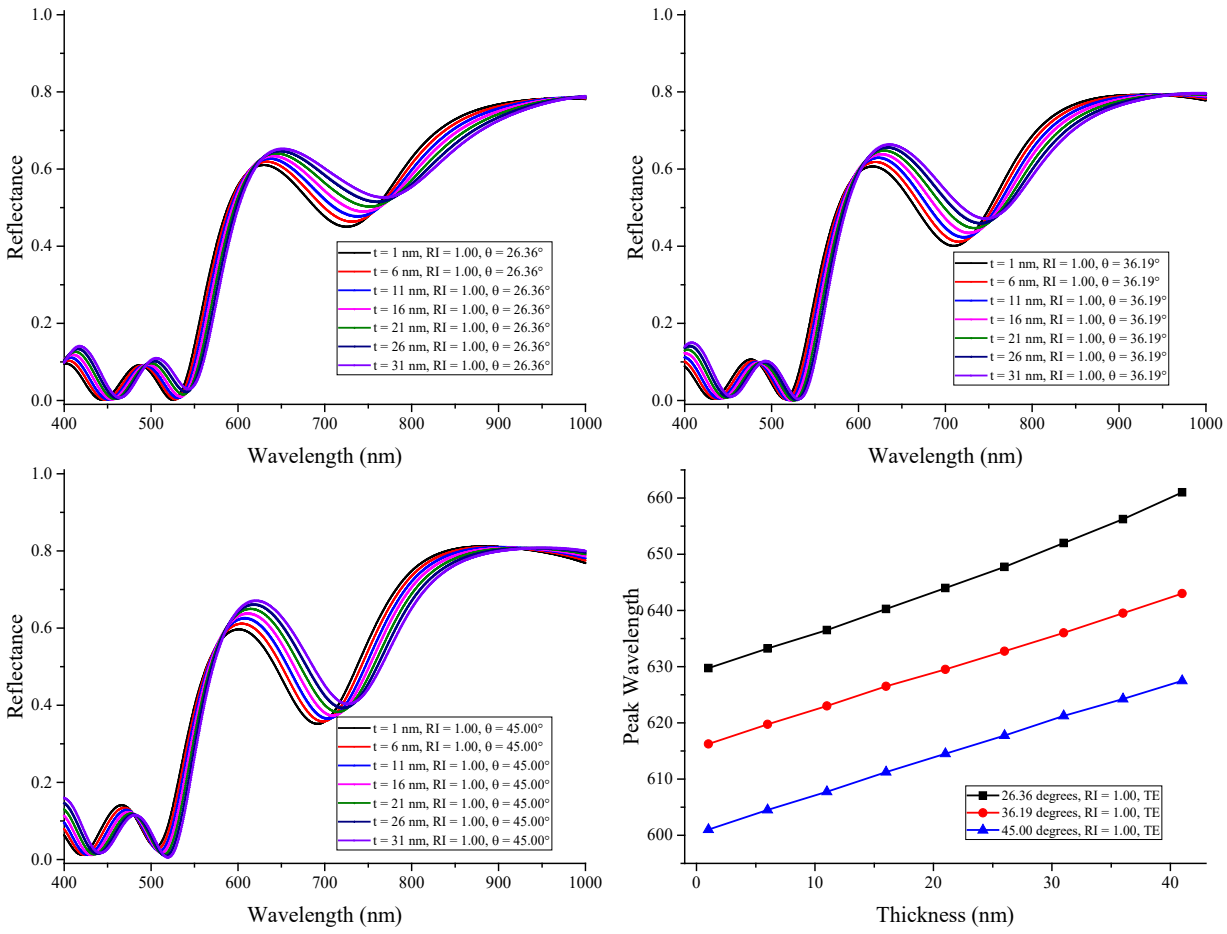

Figure 3-4 Incidence Angle Effects - in Air: Reflection spectra for increasing protein (n = 1.51) thickness at three different incidence angles

The calculated reflection spectra of the I-OQCM in water (RI = 1.33) for increasing protein (n = 1.51) thickness are shown in Figure 3-5. With the reduced fringe contrast, tracking the peak wavelength becomes difficult. An alternative approach is to integrate the dI/I_0 response over a broadband spectral range (450 to 1000 nm) – the resulting quantity is called the integrated response (IR), which is plotted in Figure 3-5, lower right. Similar to in air, the fringe contrast is reduced past 650 nm due to reduced absorption by the Si blocking layer at longer wavelengths, but fringes in the interference spectra are clearly visible.

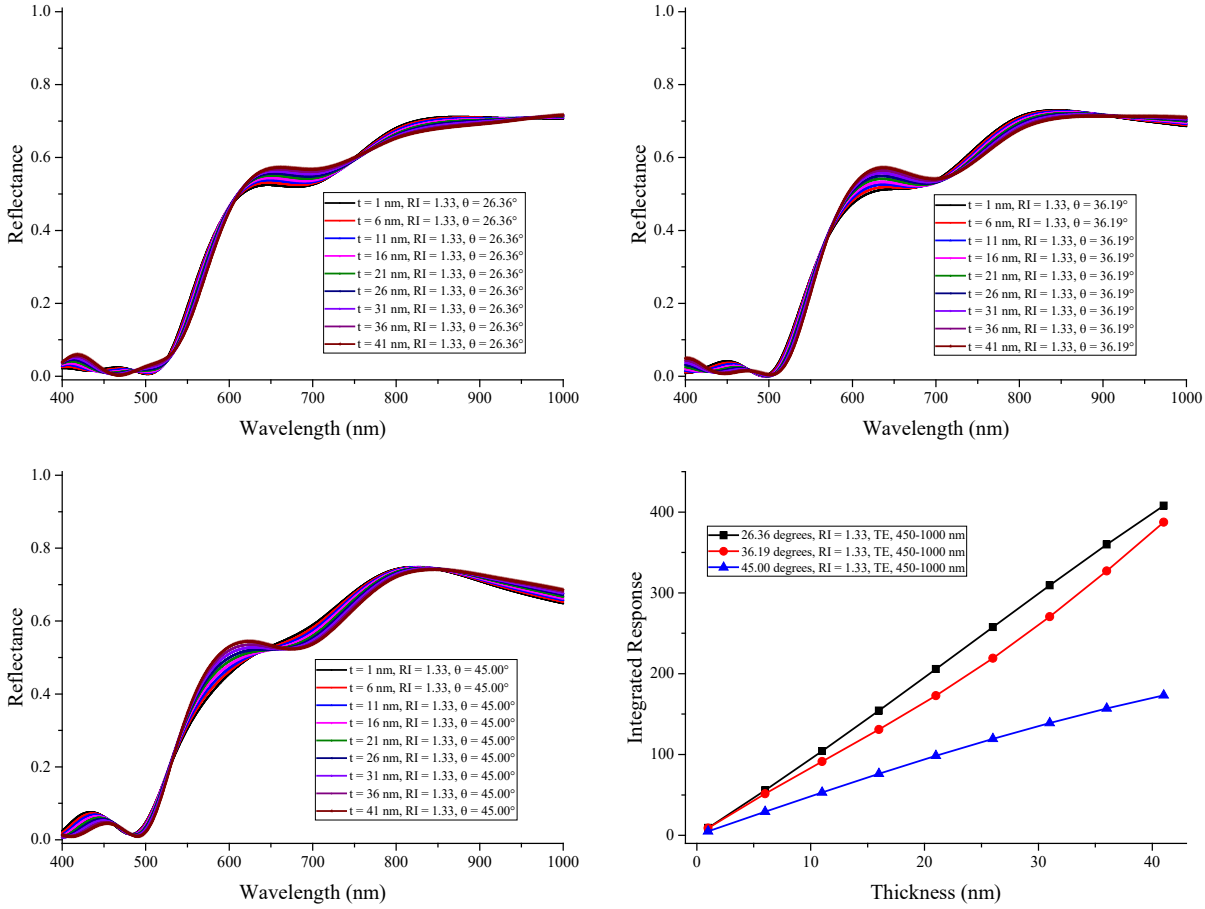

Figure 3-5 Incidence Angle Effects – In Water: Reflection spectra for increasing protein (n = 1.51) thickness at three different incidence angles

The baseline frequency shift due to the optical layers can be estimated by using the Sauerbrey equation to calculate the expected frequency shift for each optical layer and adding the results. Using the material parameters and thicknesses from Table 3-1, and crystal frequency of 9 MHz, the expected frequency difference between the bare Ta and I-OQCM sensor in air is calculated to be 23.27 kHz.

3.4 Device Fabrication

3.4.1 QCM Electrode Fabrication Process

The I-OQCM was fabricated in the Lurie Nanofabrication Facility at the University of Michigan. The fabrication process for the QCM electrodes is shown in Figure 3-6, and described in detail below.

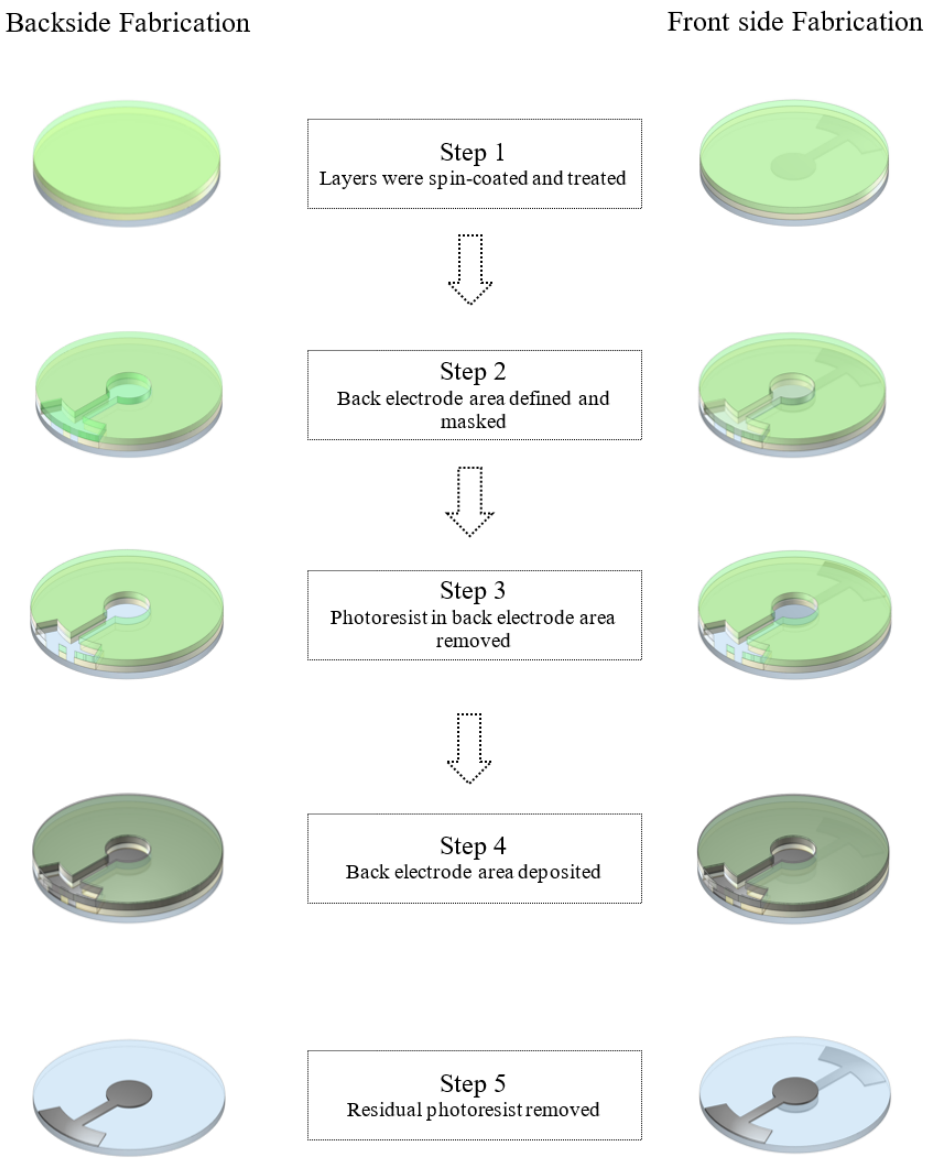

Figure 3-6 Fabrication Process for QCM Electrodes

Preparation:

The 1-inch diameter AT-cut quartz wafers are purchased from Inficon EDC. Wafers used are 185 microns thick, corresponding to a fundamental oscillation frequency of 9 MHz. The wafer is cleaned by sonicating in acetone and IPA, then plasma-treated for a minimum of 180 seconds at 100 W RF power, 35 sccm to remove residual organics.

Fabrication:

Steps 1-5 of the fabrication process shown in Figure 3-6 are described in detail below.

1. The backside is fabricated first. The wafer is baked for 5 minutes at 115 degrees Celsius to dehydrate the surface. LOR 10B photoresist was spin-coated onto the wafer at 4000 RPM for 30 seconds using a CEE 100B spinner, then baked for 6 minutes at 190 degrees Celsius. Next, S1813 is spin-coated at 4000 RPM for 30 seconds, then baked for 5 minutes at 115 degrees Celsius.
2. Exposure is performed using a Karl Suss MA/BA-6 Mask/Bond aligner with hard contact for 20 seconds to define the electrode area.
3. The resist bilayer is then puddle developed for 60 seconds with AZ 726 developer. The sample is then placed in a plasma machine for 20 seconds at 100 W power, 35 sccm O_2 to remove residual photoresist.
4. A 100 nm Ta film with 10 nm Ti adhesion layer was sputtered onto the patterned wafer with a Kurt Lesker Lab 18 PVD tool.
5. The sample is then placed into heated Remover PG after deposition to perform lift-off, leaving the electrode patterned on one side. The sample is cleaned with IPA, then placed

in the YES Plasma stripper for 20 seconds at 60 degrees Celsius, 100 W RF Power, 35 sccm O_2

The wafer is flipped over, and the above process repeated to fabricate the other electrode.

3.4.2 Optical Sensing Area Fabrication

The optical interferometric structure is fabricated in two phases: the blocking layer and the interferometric layer. These layers are deposited directly on top of the electrode, but only in the sensing area, where the electrode is patterned on both sides of the QCM wafer.

1) Fabricate the blocking layer:

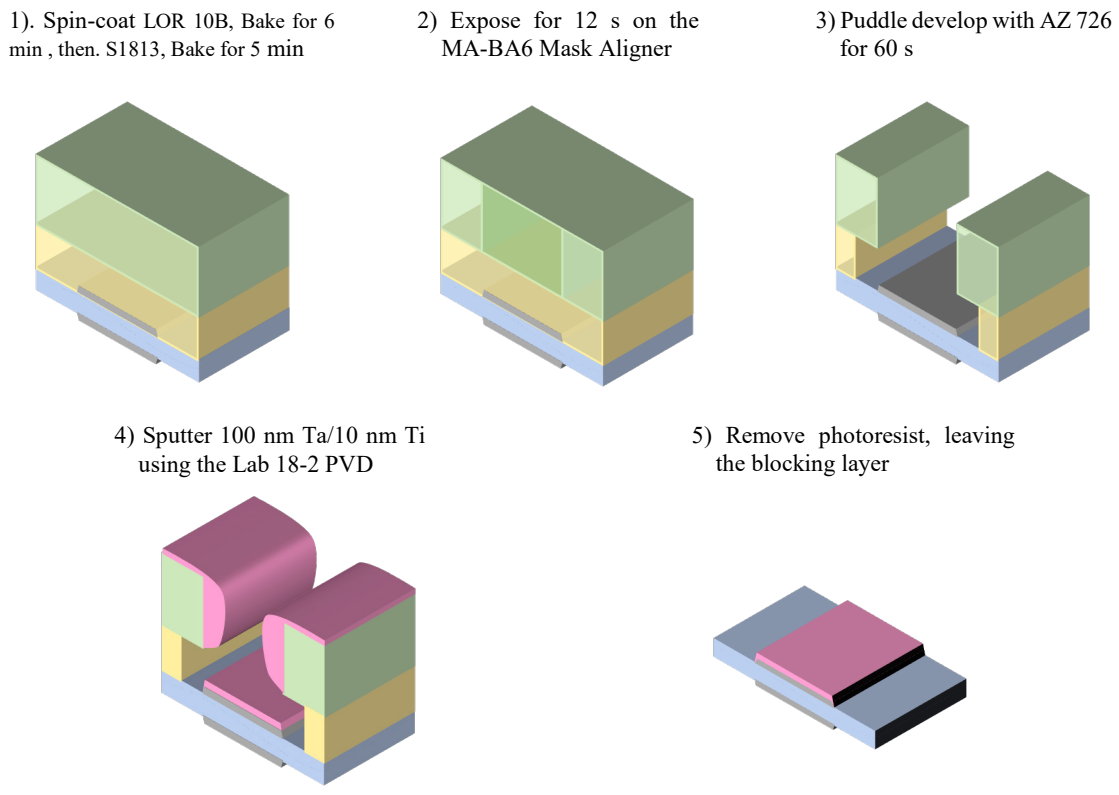

Figure 3-7 Fabrication Process for Optical Layers Part 1: P-Doped Silicon Blocking Layer (100 nm)

The process for fabricating the blocking layer is shown in Figure 3-7. The procedure for depositing the blocking layer is the same as that of the electrodes, except for two steps: the mask used is such that the developed area is confined to the overlap between the top and bottom electrodes, where the QCM oscillation will occur; and the material deposited is 100 nm of p-doped Si.

2) Fabricate the interferometric layer

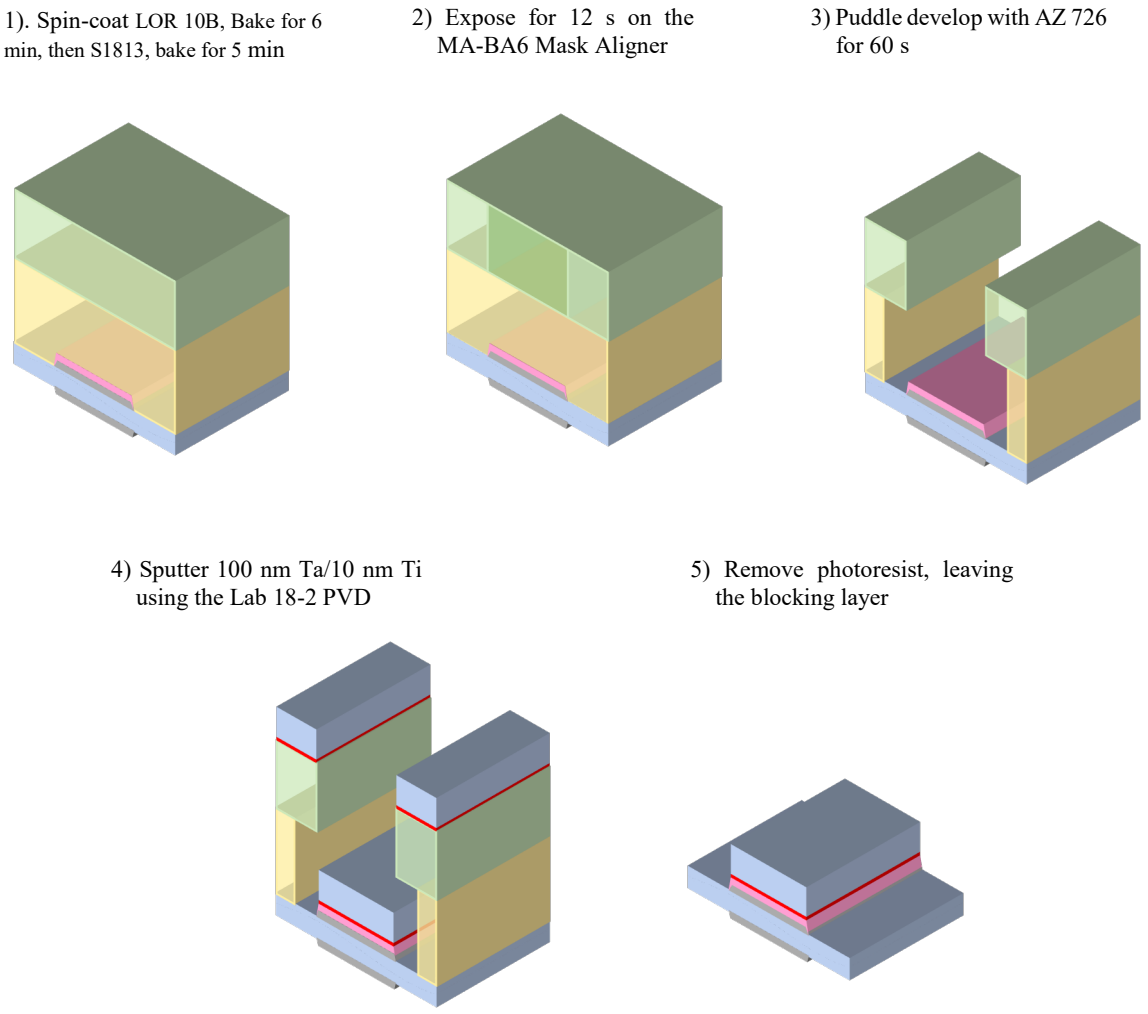

Figure 3-8 Fabrication Process for Optical Layers Part 2: Interferometric Layers of OQCM

The procedure for depositing the interferometric layer is similar to that of the bare QCM, and the process is shown in Figure 3-8. The mask used in this step is the same one used for the blocking layer. In step (4), the interferometric layer deposited consists of 400 nm SiO_2/30 nm TiO_2, evaporated using a SJ-26 evaporator, which was later changed to an Angstrom Evaporator. The TiO_2 served both as an adhesion layer, and a thin absorbing layer to reduce reflection from the blocking layer.

Finally, to complete the sensor, lead wires are bonded to the sensor at the top and bottom electrode pads (located at the edge of the wafer) with silver paste and allowed to dry for 24 hours.

3.5 Experimental Setup and Procedure

3.5.1 Experimental Setup

The experimental setup (Figure 3-9) consists of two branches for the 2 functions of the dual-modes: One branch is used to monitor the mechanical response, and the other to monitor the optical response.

The mechanical time-resolved response is logged via a RQCM machine from Maxtek Inc. The SMB cable leads from the channel on the RQCM are connected to the lead wires from the I-OQCM wafer to drive and monitor the mechanical response.

The optical branch of the experimental setup is configured for spectral interrogation. Light from a fiber-coupled halogen white light source (HL-2000 from Ocean Optics) is incident on the sensing area, with a beam diameter of 2 mm. The reflected light is collected by a lens and focused into the collection fiber (multimode, Ocean Optics), and sent to a HL-4000 custom spectrometer, with resolution 0.2 nm for the VIS-NIR range. The setup can be modified for intensity interrogation by switching the white light source for a laser with wavelength at the quadrature

point and replacing the spectrometer with a photodetector to monitor the reflected light intensity at that wavelength.

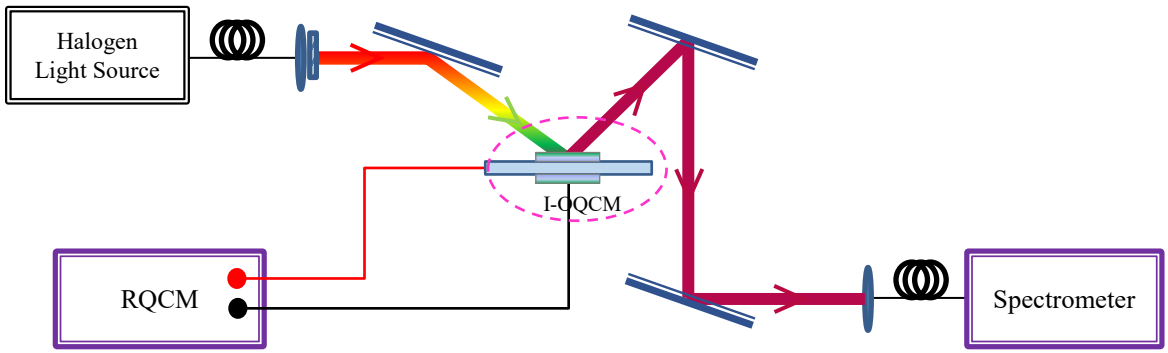

Figure 3-9 Experimental setup for testing the I-OQCM. White light from a fiber-coupled halogen light source is collimated with an asphere, then polarized and directed onto the OQCM sample. The reflected light is sent into a USB spectrometer. At the same time, the lead wires from the OQCM are connected via SMB connection to the RQCM machine to monitor the resonance frequency vs. time

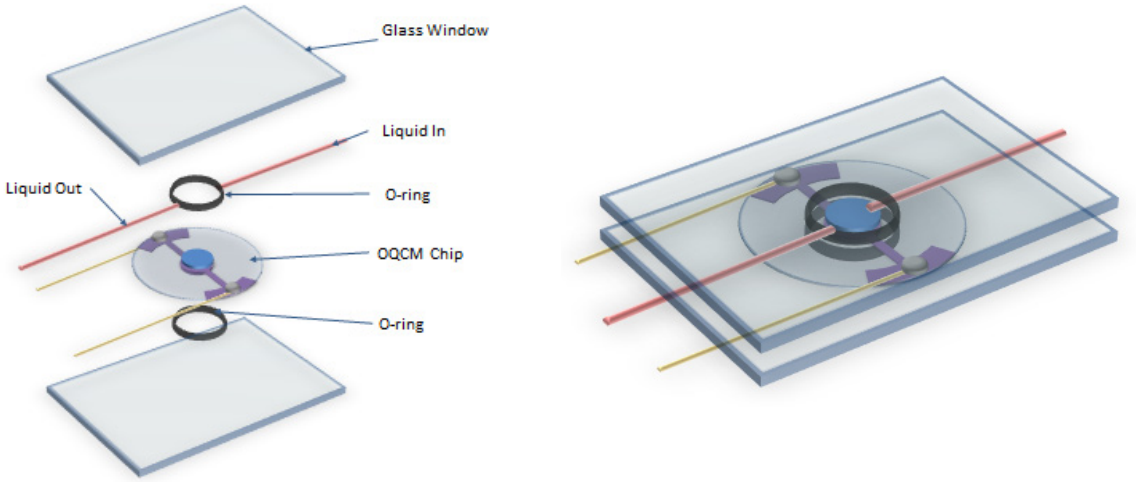

Figure 3-10 Fixture for the OQCM. For vapor sensing, a hole is cut in the glass window to allow vapor to be introduced and to escape. A test fixture is made from two slides and a pair of Viton fluoroelastomer o-rings, which are used to secure the OQCM chip. O-ring spacers (not shown) are added between the windows to prevent excessive pressure being applied to the OQCM via the o-ring and glass window

To conduct dual-mode tests, the OQCM is secured between two Viton fluoroelastomer o-rings to prevent contact of the remainder of the fixture with the sensing area. A polycarbonate slide with a central hole and channels is placed on top of the second o-ring to form the sensing chamber with liquid inlet/outlet channels. Finally, a glass cover slide with a hole drilled on each side is placed on top of the polycarbonate slide and glued with PDMS, in order to seal off the channels and define the liquid inlet and outlet ports. A set of o-ring pairs (Figure 3-11) are placed between the top and bottom slides to act as a spacer and prevent accidental application of excessive pressure on the OQCM crystal, and deformation of the cover slide. A schematic and photograph of the fixture are shown in Figure 3-10 and Figure 3-11 respectively.

If a large incidence angle is required, an N-BK7 prism is placed on top of the glass window, with index matching fluid (Norland, RI = 1.52) used between the prism and glass slide to prevent any TIR at the interface due to air gaps.

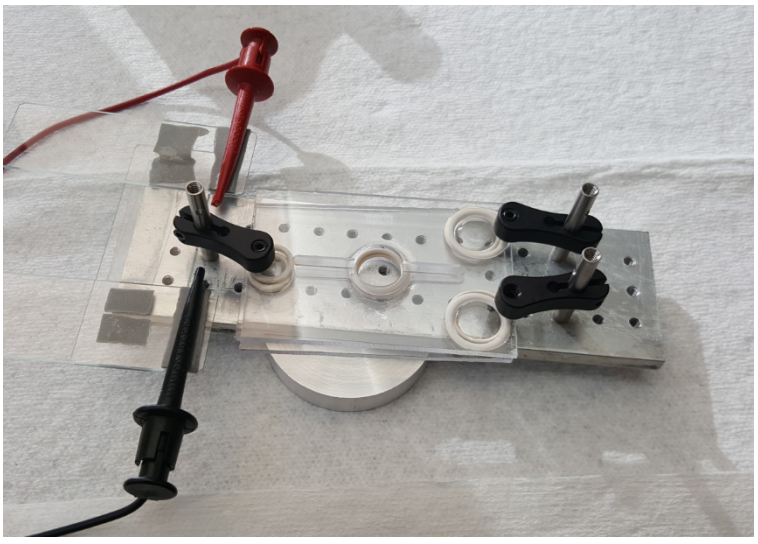

Figure 3-11 Photograph of fixture used for dual-mode measurements

3.5.2 Experimental Procedure

The sample is secured into the fixture. The procedures for the different experiments conducted are as follows.

1. *Mechanical characterization*: G (conductance) vs. frequency curves are acquired using the Agilent 4391A network analyzer. For liquid loading tests, preliminary tests were conducted with 4 uL of liquid in the center of the sensor, followed by covering the entire sensor area for the I-OQCM liquid loading test.
2. *Optical characterization*: Reflection spectra are collected via an HL-4000 Ocean Optics spectrometer
3. *Mechanical Response to Vapor Deposition*: Water vapor is introduced from the open window of the fixture onto the I-OQCM sensor surface and allowed to evaporate. Frequency and resistance data were collected at regular intervals using a Maxtek RQCM.
4. *Optical Response to Vapor Deposition*: Water vapor is introduced from the open window of the fixture onto the I-OQCM sensor surface and allowed to evaporate. Optical spectra are collected at regular intervals using the HL-4000. Peak wavelength and reflectance at 561 nm are then extracted from the spectrum at each point in time.
5. *Dual-Mode Measurements*: Water vapor is introduced from the open window of the fixture onto the I-OQCM sensor surface and allowed to evaporate. The I-OQCM is connected to both the RQCM after being placed into the optical setup, and both the mechanical and optical responses are monitored with the RQCM and HL-4000 respectively.

3.6 Results and Discussion

3.6.1 Mechanical Characterization

The frequency response of the bare Ta electrode QCM sensor and OQCM sensors were measured using the Agilent 4391A network analyzer with attached impedance module. Fitting was performed to obtain the equivalent BVD circuit parameters for each sensor, and the values obtained are listed in Table 3-2.

Table 3-2 Calculated BVD circuit parameters for Bare Ta Sensor and OQCM Sensor in Air

Sensor Type	**Resonant Frequency** (MHz)	**Resistance R_1** (Ohms)	**Inductance L_1** (H)	**Capacitance C_1** (fF)
Bare Ta Sensor	8.980600	55.10	0.0079272	39.6194
OQCM Sensor	8.960372	37.50	0.0076915	41.0392

The characterization results are plotted in Figure 3-12. The plots show 2 sources of frequency shifts:

1. Shift due to liquid medium
2. Shift to optical layers on the I-OQCM sensor

The baseline frequency shift due to the optical layers is 20.2 kHz, which is 15% lower than the predicted value. The discrepancy could be a result of differences in the density or thickness of deposited layers, as well as effects from the finite thickness and/or stress in the materials.

To calibrate the I-OQCM sensor response for bulk liquid loading, 4 µL of each liquid was placed onto the OQCM sensor using a pipette. For comparing the liquid loading response to literature, the entire sensor surface was covered with the bulk liquid. The sensor response for the

latter case was fitted according to the modified BVD circuit for liquid loading from Martin et al.[17]. The circuit parameters obtained are listed in Table 3-3. To compare the response to the standard model, the effective density-viscosity product is calculated from the frequency shift Δf_s using equation (12).

$$\rho\eta \approx \left(\frac{\sqrt{\bar{c}_{66}\rho_q}\Delta f_s}{2f_s^2}\right)^2 4\pi f_s \tag{12}$$

Table 3-3 Calculated BVD circuit parameters and liquid density and viscosity of the OQCM in three different liquids

Sensor	**f_s** (MHz)	**Δf_s** (kHz)	**R_2** (Ohms)	**L_2** (μH)	**ρη** (g^2/cm^4 s)	**ρη** (25C) (g^2/cm^4 s)
I-OQCM (Air)	8.960372	0.0000	0.00	0.0000	0.00000	0.00000
I-OQCM (Water)	8.958117	-2.2547	164.40	3.6500	0.01734	0.00890
I-OQCM (1:1 Water:Glycerol)	8.954723	-5.6491	493.80	9.1500	0.10887	0.06356[61]

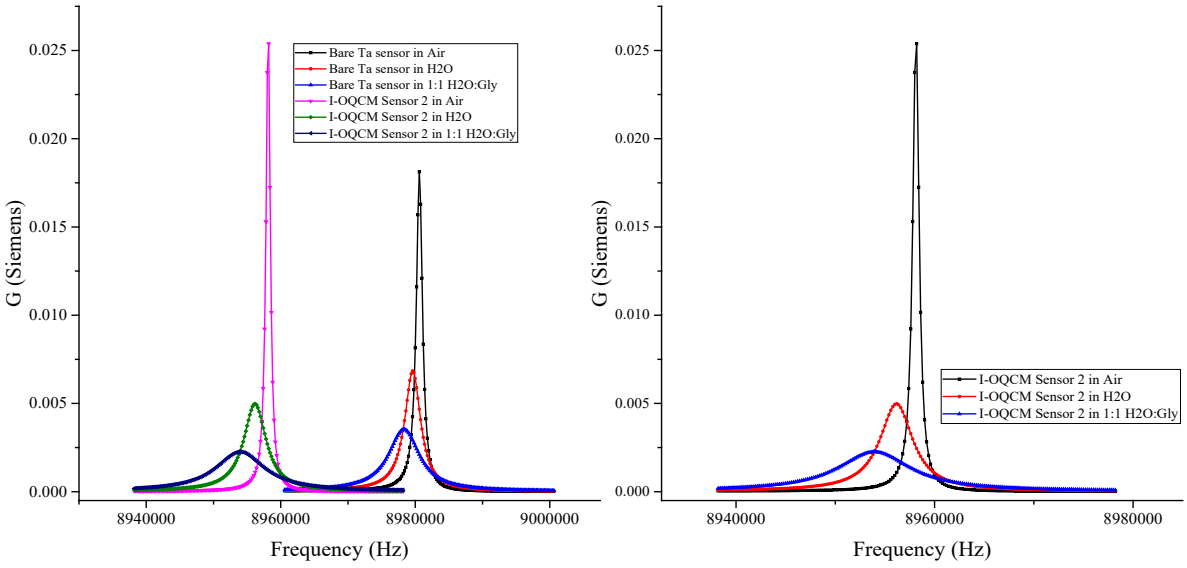

Figure 3-12 Left: G vs. frequency plot of Bare Ta and SiO_2 I-OQCM Sensor 2 response to 4 uL of liquid in center of sensor. Right: I-OQCM Sensor 10 response to full coverage of sensing area with bulk liquid

The calculated effective density-viscosity product is about 1.6 times the value expected from literature. This may be a result of the relatively thick layers on the I-OQCM (total thickness of blocking + interferometric layers exceeding 600 nm), which introduces a relatively large mass loading effect, such that the resulting liquid loading deviates from the liquid behavior for an uncoated or thinly coated QCM wafer.

3.6.2 Optical Characterization

The optical response of the OQCM sensor is measured using the HL-4000 USB Spectrometer (Ocean Optics). The results are plotted in Figure 3-13.

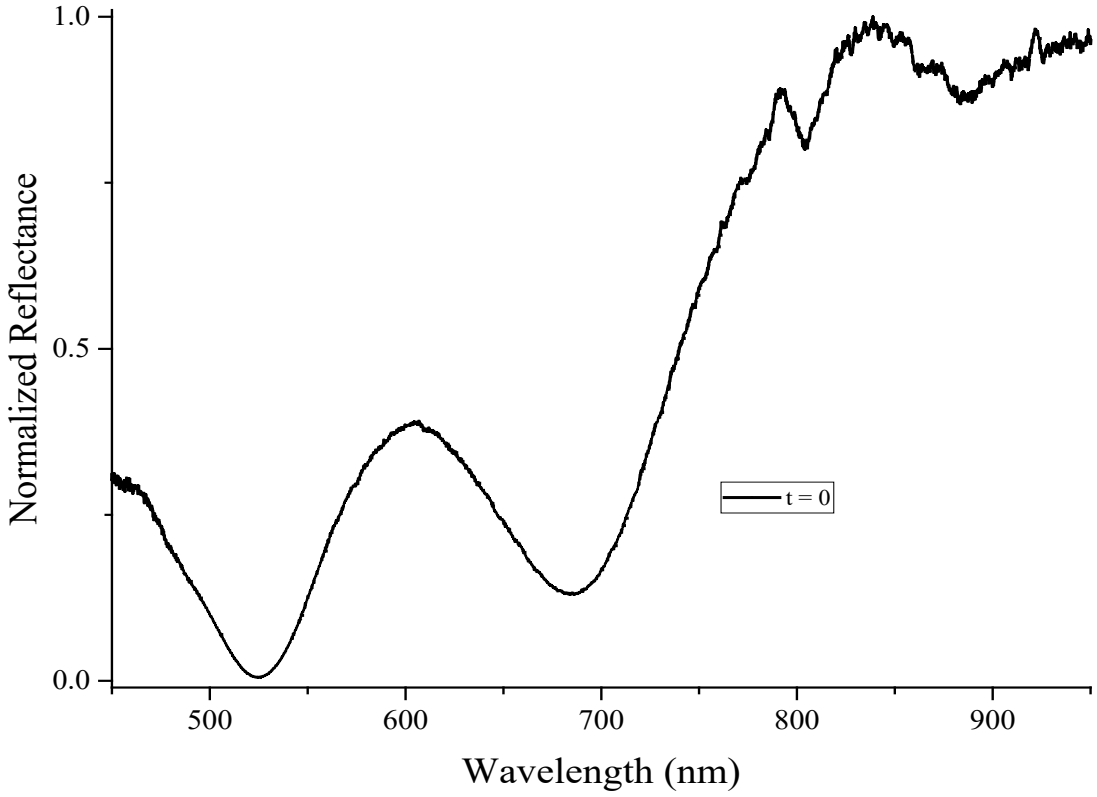

Figure 3-13 Broadband reflection spectra of an I-OQCM in air with s-polarized light

The interference fringes formed by the dielectric layers are clearly visible up to 700 nm in the broadband reflection spectrum. Beyond 700 nm, the fringe contrast is reduced as the contribution from the tantalum electrode becomes greater due to the decreasing absorption coefficient of the Si blocking layer at longer wavelengths.

3.6.3 Mechanical Response to Vapor Deposition and Evaporation

To demonstrate the real-time mechanical sensing capability of the I-OQCM sensor, the electrode pads are placed in contact with the lead wires from the SMB cables connected to the RQCM. The sample is exposed to human breath at irregular intervals, and the frequency and resistance are recorded on the RQCM. The real-time response is plotted in Figure 3-14.

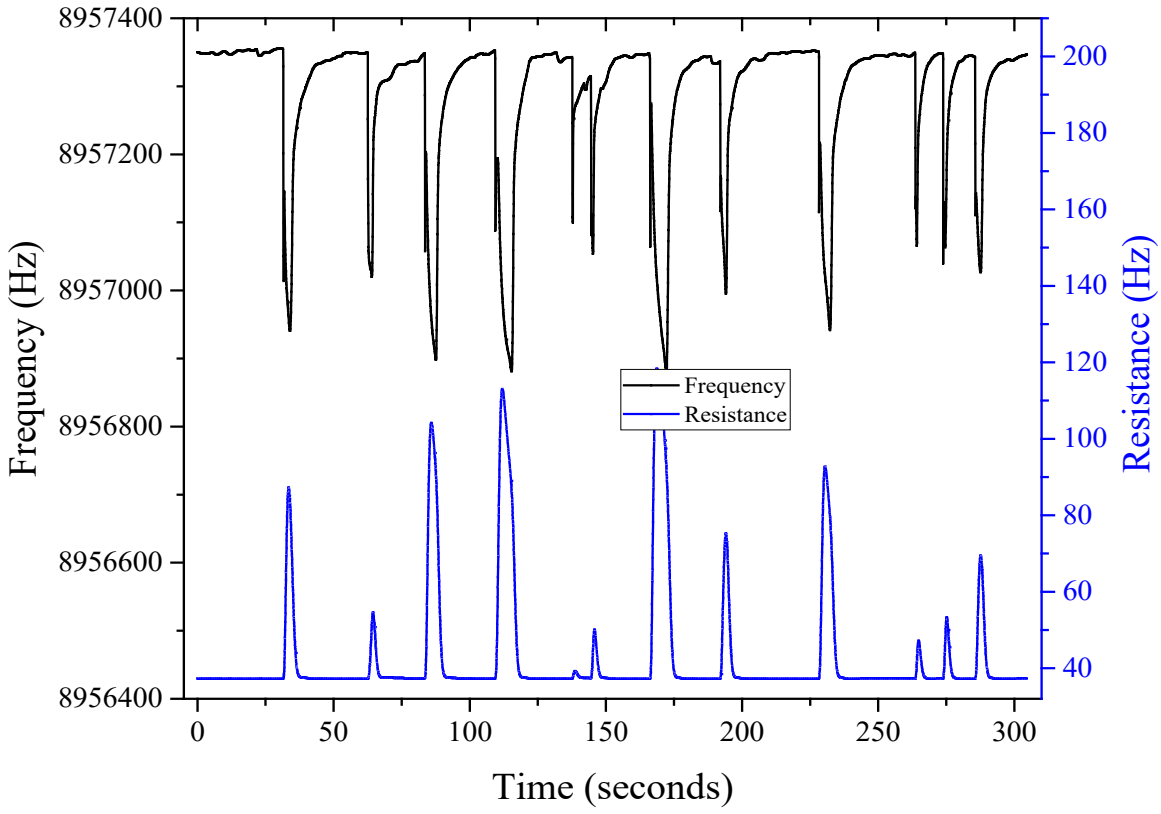

Figure 3-14 Mechanical response of an I-OQCM to vapor deposition and evaporation

The mechanical response to a single pulse of vapor can be separated into the following stages: condensation, equilibration, absorption/diffusion, and evaporation. A detailed analysis of the mechanical response at each stage is given in section 3.6.5.

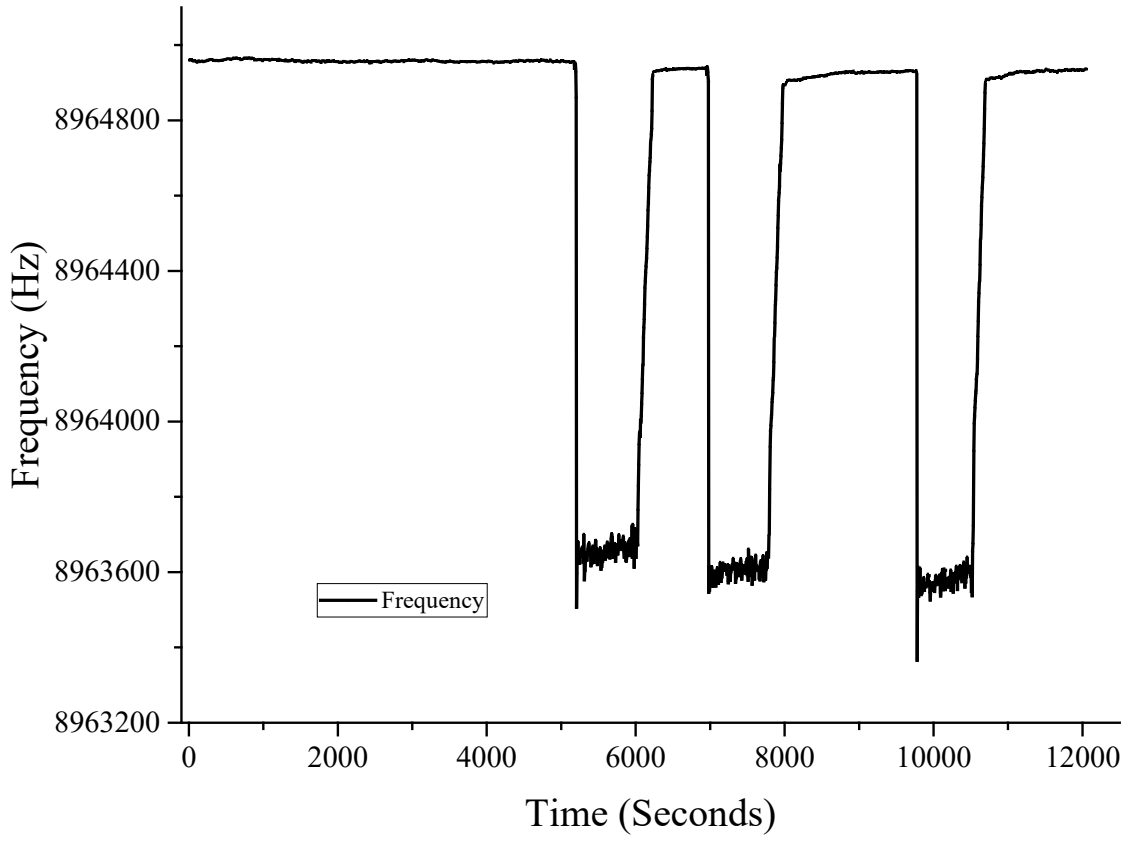

Figure 3-15 Mechanical response of I-OQCM sensor to liquid loading

A liquid loading experiment was performed on the I-OQCM, and the results are shown in Figure 3-15. Upon liquid being introduced to the surface of the sample, the frequency immediately decreased to the steady-state frequency due to bulk medium loading (water in this case). The frequency remains at this value until sufficient water has evaporated that the bulk loading approximation is no longer valid (liquid depth >> mechanical penetration depth (170 nm in DI

water at 9 MHz). At this point the frequency rises quickly, then slowly as the remaining thin film of water evaporates into air, returning to the original oscillation frequency.

3.6.4 Optical Response to Vapor Deposition and Evaporation

To demonstrate the real-time optical sensing capability of the I-OQCM, the fixture (with the sensor inside) is placed into the reflection setup, and the optical intensity spectrum is recorded on the Ocean Optics spectrometer. The resonance wavelength and reflectance at the quadrature point (561 nm) are extracted from the optical spectrum at each point in time (Figure 3-16).

The optical response to a single pulse of vapor can be separated into the following stages: condensation, equilibration, absorption/diffusion, and evaporation. Details of the optical response are given in Section 3.6.5.

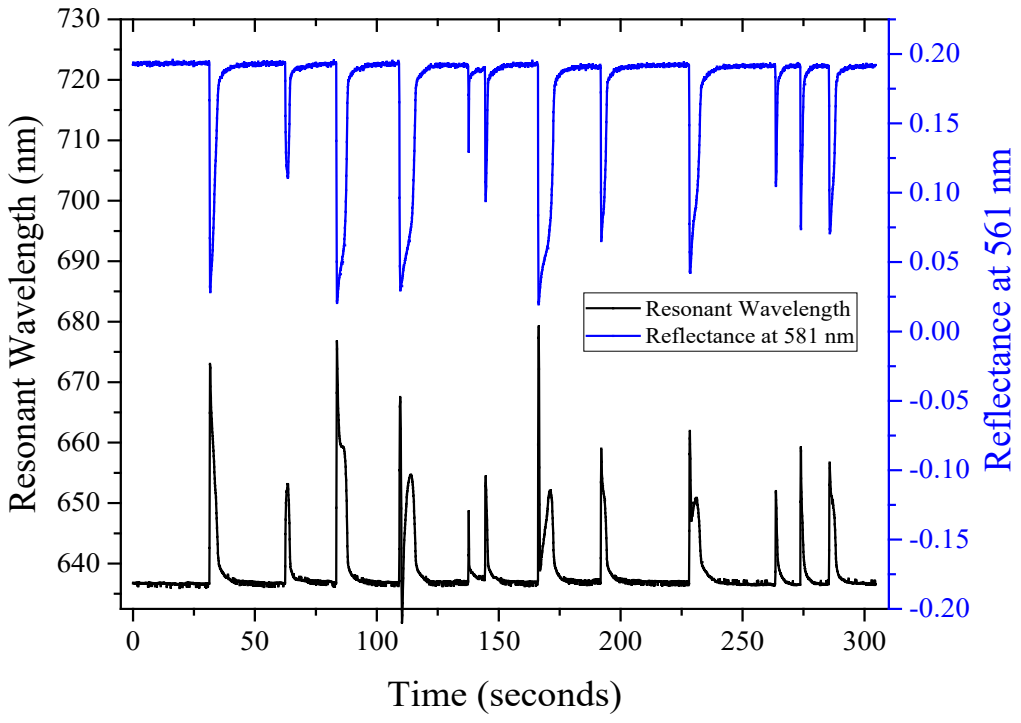

Figure 3-16 Optical response of the interferometric OQCM to vapor deposition and evaporation

3.6.5 Dual-Mode Measurement of Vapor Deposition and Evaporation

Next, dual-mode measurements of the I-OQCM were performed in air. The I-OQCM chip is secured into the fixture depicted in Figure 3-10. The optical spectrum was recorded using an Ocean Optics spectrometer with the following settings: 5 ms integration time, averaged over 3 scans. At the same time, the mechanical oscillation frequency and resistance are recorded using the Maxtek RQCM. The mechanical oscillation frequency, resistance, optical resonant wavelength and reflectance at 561 nm to irregular injections of water vapor are plotted in Figure 3-17. Figure 3-18 focuses on the details of a single vapor pulse between t = 75 seconds and t = 100 seconds.

1. Condensation (83.35 s – 83.65 s): Water vapor is introduced above the I-OQCM surface. As the humidity increases, the vapor starts to condense onto the I-OQCM surface.
    - Mechanical frequency **decreases** due to the increase in mass of the condensed vapor onto the sensor surface
    - Mechanical resistance **increases** slowly due to the viscosity of the condensed film
    - Optical resonance wavelength **increases** due to the increase in thickness of the condensed vapor onto the sensor surface
    - Reflectance at 581 nm **increases** as the vapor film increases in thickness
2. Equilibration (83.65 s – 83.95 s): As the humidity increases further, a small amount of the condensation on the OQCM surface evaporates to establish equilibrium with the water vapor above the sensor.
    - Mechanical frequency **increases** slightly due to the slight decrease in mass of the condensed vapor evaporating from the sensor surface

- Mechanical resistance **increases** slowly due to the humidity above the sensor surface
- Optical resonance wavelength **decreases** slightly due to the decrease in the thickness of the condensed vapor layer
- Reflectance at 581 nm **decreases** as the vapor film increases in thickness

3. Absorption/Diffusion (83.95 s – 87.65 s): The flow of water vapor is terminated. The condensed water vapor is adsorbed onto the sensor surface in liquid phase. The viscoelastic nature of the water film becomes more visible here.
    - Mechanical frequency **decreases** due to the absorption of the condensed water vapor onto the sensor surface, increasing the viscosity into the film
    - Mechanical resistance **increases** due to vapor adsorption onto sensor surface
    - Optical resonance wavelength **remains relatively stable** since the total optical thickness of the vapor layer has not changed significantly
    - Reflectance at 581 nm **decreases slightly** as the vapor film is adsorbed onto the sensor surface
4. Evaporation (87.65 s – 100 s): The condensed vapor evaporates. The evaporation process occurs in two phases: in the first phase, the water vapor above the sensor is evaporating at the same time as the condensed vapor. This accelerates the evaporation process and corresponding response in the mechanical and optical parameters below. In the second phase, after all the vapor above the sensor has evaporated, the remaining adsorbed water is released back into the atmosphere at a slower exponential rate.

- Mechanical frequency **increases** due to vapor evaporation (above sensor and from sensor surface) and diffusion of adsorbed vapor back to the sensor surface, reducing the mass of the condensed vapor on the sensor surface.
- Mechanical resistance **decreases** due to vapor evaporation (above sensor and from sensor surface) and diffusion of adsorbed water vapor back to the sensor surface
- Optical resonance wavelength **decreases** due to vapor evaporation, reducing the optical thickness of the condensed vapor on the sensor surface
- Reflectance at 581 nm **increases** as the vapor film is evaporating from the sensor surface

5. The sensor stabilizes at the initial conditions.
    - Mechanical frequency **stabilizes** at the initial value
    - Mechanical resistance **stabilizes** at the initial value
    - Optical resonance wavelength **stabilizes** at the initial value
    - Reflectance at 581 nm **stabilizes** at the initial value

Fitting the data at the second evaporation "tail" to an exponential decay curve, a decay time constant of τ_{freq} = 3.0979 seconds for the mechanical frequency and τ_{WLPeak} = 1.6263 seconds for the resonant wavelength is obtained for vapor absorption for the film on the I-OQCM sensor.

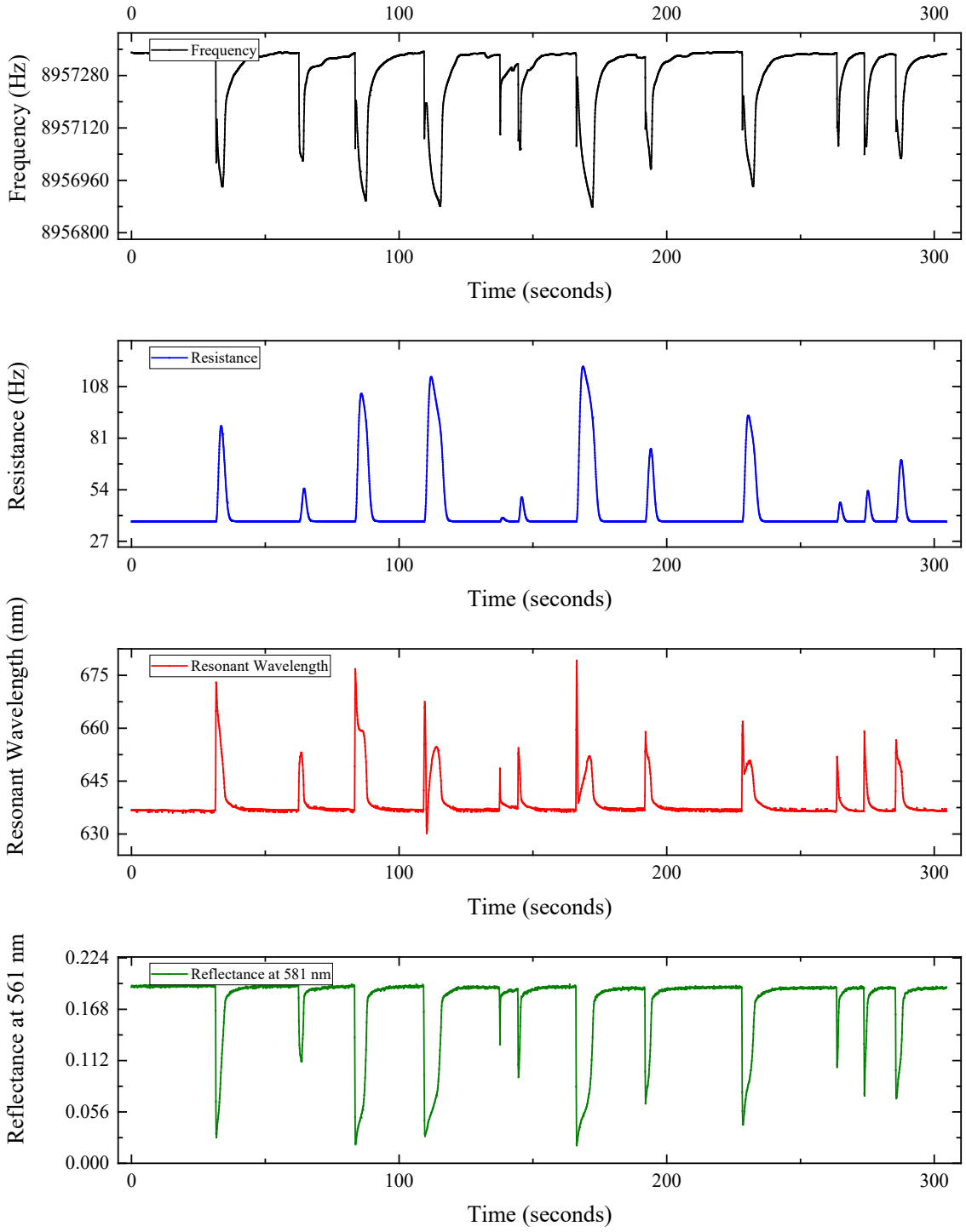

Figure 3-17 Dual-mode measurement of water vapor injection at irregular intervals. Frequency, Resistance, Resonant Wavelength and Reflectance at the quadrature point (561 nm) are plotted from top to bottom

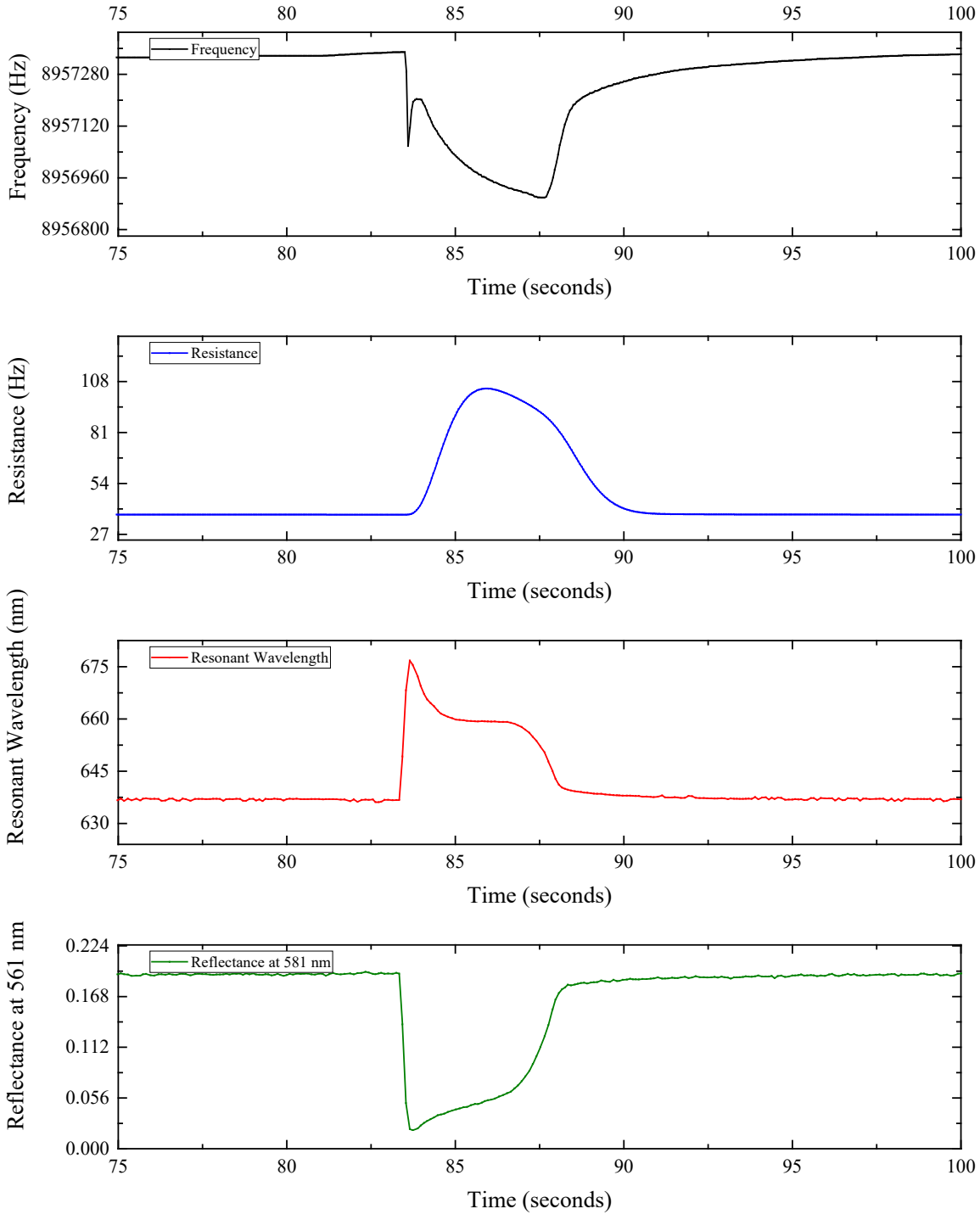

Figure 3-18 Dual-mode measurement of water vapor injection pulse at 83 seconds. Frequency, Resistance, Resonant Wavelength and Reflectance at the quadrature point (561 nm) are plotted from top to bottom

3.7 Summary

The interferometric OQCM (I-OQCM) is discussed in detail in this chapter. The theory and basic structures of the I-OQCM and the complete fabrication process are presented. The I-OQCM seeks to address the low contrast and insufficient range issues from current hybrid sensors by including a blocking layer, a thicker interferometric layer and higher refractive index (RI) layers to increase the reflection contrast in liquid. These help to set a baseline optical spectrum where a wavelength shift due to thin film thickness changes is easier to detect. A set of simulations was done first to find the optimal parameters and determine the direction of the experiments. The test results on the I-OQCM show the frequency and spectral shifts that were expected under different conditions and verify the theoretical analyses and simulation results.

The dual mode tests demonstrate the ability to collect both mechanical (frequency and resistance) and optical (resonance wavelength and reflectance) information simultaneously from a single I-OQCM sensor.

Chapter 4: Optical Quartz Crystal Microbalance Structure 2 – Plasmonically-Enhanced Grating OQCM Sensor

4.1 Motivation for the Plasmonically-Enhanced Grating OQCM Sensor

While the interferometric OQCM (I-OQCM) sensor developed in Chapter 3 is simple in structure and easy to fabricate, it has two weaknesses. First, there is an intrinsic tradeoff between reducing the linewidth of the optical reflection spectrum and increasing the wavelength sensitivity. As either the interferometric layer thickness or refractive index is increased, the relative phase change for a given thickness change is reduced, even as the linewidth of each resonance peak is decreased. In addition, a greater interferometric layer thickness will increase the mass loading on the I-OQCM. The second lies in the fact that the contrast of the interference fringes (in the reflection spectrum) is determined by the difference in amplitude between the interfering beams. For a low-index layer, the reduced refractive index difference at the liquid-solid interface makes measurements in water/aqueous solutions more difficult as a result of the low-contrast interference pattern.

The Plasmonic-Enhanced Grating OQCM (PEG-OQCM) sensor structure discussed in this chapter addresses both issues by employing a dielectric grating on a metal layer (the electrode on the PEG-OQCM). The dielectric grating coupler provides coupling to the surface plasmon at the grating-metal interface [62-69]. With the plasmonic grating, a linewidth of 25 nm is obtained in air, 15 nm in water – a factor of 3-6 improvement over current SPR/LSPR-based sensors, where the

linewidths are usually 50-100 nm[34, 70]. The reflectance dip yields a depth of 60% and can be optimized further by including additional layers to the structure described below to improve coupling to the plasmon. Additionally, the sensor can achieve near zero sensitivity to the bulk refractive index at an optimized incidence angle.

Several researchers (Abutoama et al.[71, 72] and Mizutani et al.[73]) have utilized this type of sensor, but primarily as a bulk refractive index sensor. Abutoama excited the grating-assisted plasmon mode with TM polarized light, while Mizutani et al. used TE polarized light to excite a waveguide mode in a taller grating. Jung et al.[74] have used this structure for DNA detection and surface sensing, but their configuration relies on prism coupling, which has the same issues as previous SPR-based hybrid sensors for a QCM device.

While the LSPR-based structure from Grab et al.[34] also has an angle where bulk sensitivity effectively vanishes, there are several disadvantages in their structure that are addressed in the PEG-OQCM.

1. The spectral response of the core-shell structures in the LSPR-based structure is highly sensitive to their dimensions, and the standard deviation for the diameter is listed as +/- 10% to 15% - this results in a broadened lineshape due to the large distribution in dimensions. In our structure, the duty cycle for the shape varies by only +/- 5 nm, corresponding to +/- 0.7% variance in the lateral grating ridge dimensions.

2. The spectral width of the peak in the LSPR sensor extinction spectrum is approximately 100 nm at full width half-maximum (FWHM) in water, which is 6.7 times broader than the 15 nm linewidth achieved by our PEG-OQCM.

3. Their fabrication method involves nanoparticle deposition via self-assembly and has a greater chance of resulting in non-uniform coverage of the QCM surface that will impact the sensor response. Our PEG structure, in contrast, is fabricated using standard semiconductor techniques, which have low manufacturing variance and high coverage uniformity[75, 76].

4. Our structure is fabricated using silicon dioxide, titanium dioxide and gold, and is completely open to the bulk medium. This makes our structure significantly more resistant to water absorption by the sensing medium, and more resistant to water trapping in cavities, both of which can impact the resulting measured absorbed mass[77].

4.2 Device Structure

The grating structure used in the PEG-OQCM sensor we developed is based on the structure by Abutoama et. al.[71], but our structure is designed specifically for surface sensing in aqueous media (RI around 1.33) at approximately 45 degrees, with an anti-resonance around 785 nm. The grating structure for this sensor is designed for a width w = 706 nm, period Λ = 1395 nm, and total height h = 120 nm. Each grating ridge has the following structure (from top to bottom): 110 nm SiO_2/10 nm TiO_2 (which serves as an adhesion layer). A further modification was made by adding a thin set of spacer layers: 15 nm SiO_2/10 nm TiO_2. The TiO_2 serves as an adhesion layer, while the SiO_2 is included such that the full sensing surface is exposed SiO_2, providing a uniform material for functionalizing the surface of the biosensor. The structure of the PEG-OQCM, with photos and top-view SEM image, are shown in Figure 4-1.

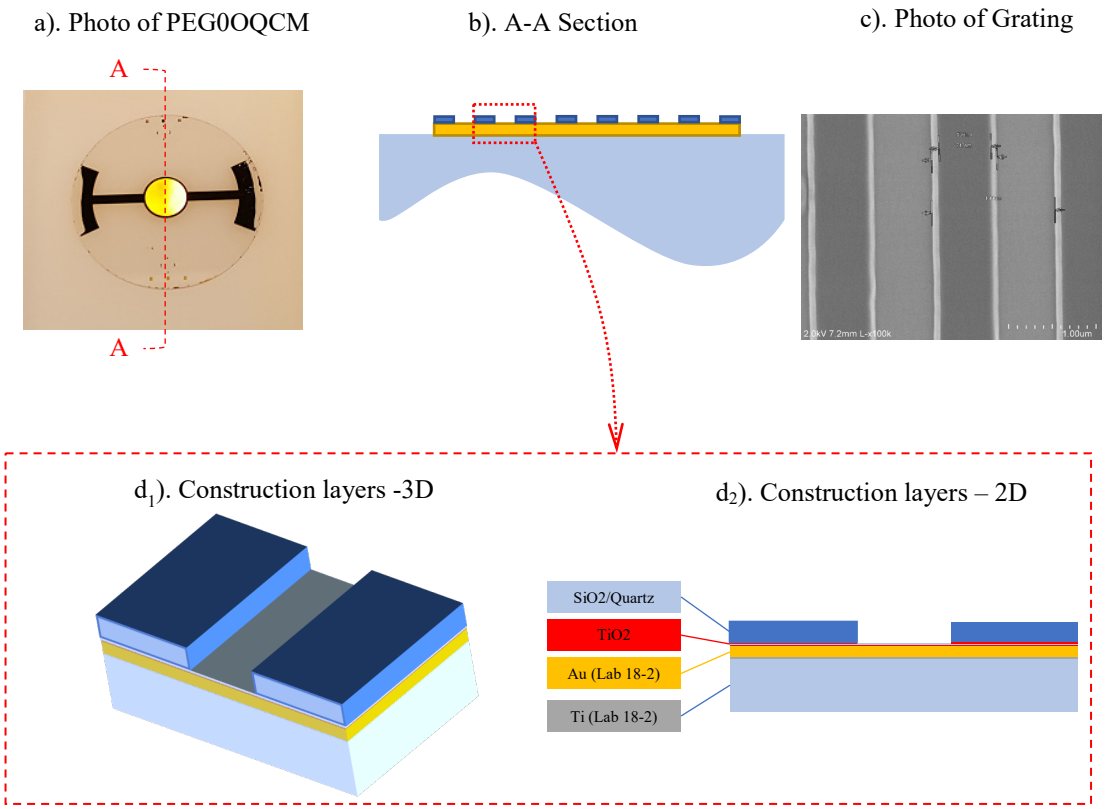

Figure 4-1 Structure of the Plasmonic Grating OQCM sensor. The structure is optically identical to that of the OQCM sensing area due to the Au film thickness being significantly higher than the skin depth.

4.3 Theory

In order to understand the PEG structure, we will first describe the principle of the 1D optical grating (the structure used in the PEG-OQCM), followed by the theory and operating principle of the PEG.

4.3.1 The 1-D Optical Grating

An optical grating (diffraction grating) consists of a periodic modulation at the interface between two (or more) materials[78]. Due to the periodic modulation, incident light at a wavelength λ is reflected at angles satisfying equation (13):

$$\sin\theta_i + \sin\theta_d = \frac{m\lambda}{d} \tag{13}$$

where θ_i is the angle of the incident beam, θ_d is the angle of the diffracted beam, m is the diffraction order, λ is the free-space wavelength, and d is the grating period. The diffraction grating is often used in spectrometers and monochromators to spatially separate the wavelengths of incident light, and is also used to couple light into a guided mode by providing the additional wavevector component needed to match the effective index of a SPP or waveguide mode, which cannot be achieved via direct coupling. The coupling condition is given[78] by equation (14):

$$k_0 N_{eff} = k_0 n_i \sin\theta_i + \boldsymbol{m}\frac{\boldsymbol{2\pi}}{\boldsymbol{\Lambda}}, \qquad m \in Z \tag{14}$$

where N_{eff} is the effective index of the SP or guided mode, n_i is the refractive index of the incident medium, $k_0 = \frac{2\pi}{\lambda_0}$ is the free-space wavevector, m is the order number and Λ is the period of the grating.

Optical gratings have been used as couplers in many plasmonic[79], interferometric[80] and waveguide-based sensors, but have also been used directly as the optical resonant structure in the resonant waveguide grating (RWG)[81, 82]. RWG sensors were used by Cunningham et al.[57, 58] to monitor the binding of anti-IgG.

4.3.2 The Plasmonically Enhanced Grating (PEG)

The simplest case of the PEG consists of a dielectric grating on a metal film or substrate. To analyze this structure, we examine the momentum matching equation (15) (Abutoama et al.[71]) for the surface plasmon at the grating-metal interface. Inserting the expressions for each wavevector in equation (16) and rearranging the expression, we obtain equation (17):

$$\vec{k}_{x\_inc\_light} + \vec{k}_{Grating} = \vec{k}_{SP} \tag{15}$$

$$k_0 n_a \sin\theta_a \pm m\frac{2\pi}{\Lambda} = k_0\sqrt{\frac{Re(\varepsilon_{metal})\cdot n_{eff}^2}{Re(\varepsilon_{metal}) + n_{eff}^2}} \tag{16}$$

$$\lambda_0 = \mp\frac{\Lambda}{m}\left(\sqrt{\frac{Re(\varepsilon_{metal})\cdot n_{eff}^2}{Re(\varepsilon_{metal}) + n_{eff}^2}} - n_a\, sin\,\theta_a\right) \tag{17}$$

Where $\vec{k}_{x\_inc\_light} = k_0 n_a \sin\theta_a$ is the incident wavevector in the x-direction, $\vec{k}_{Grating} = m\frac{2\pi}{\Lambda}$ is the grating contribution to the wavevector, $\vec{k}_{SP} = k_0\sqrt{\frac{Re(\varepsilon_{metal})\cdot n_{eff}^2}{Re(\varepsilon_{metal})+n_{eff}^2}}$ is the wavevector of the surface plasmon at the grating-metal interface, n_{eff} is the effective index of the medium above the metal layer, ε_{metal} is the dielectric constant of the metal, n_a is the bulk refractive index, k_0 is the incidence wavenumber in vacuum, λ_0 is the wavelength in vacuum, Λ is the period of the grating, m is the diffraction order number, and θ_a is the incidence angle in the bulk medium.

If the bulk refractive index is increased by Δn_a there will be a corresponding increase in the effective index Δn_{eff}. The wavelength bulk refractive index sensitivity is given by equation (18).

$$\frac{d\lambda_0}{dn_a} = \mp\frac{\Lambda}{m}\left(\left(\frac{Re(\varepsilon_{metal})}{Re(\varepsilon_{metal}) + n_{eff}^2}\right)^{3/2}\frac{dn_{eff}}{dn_a} - sin\,\theta_a\right) \quad (18)$$

If the condition below is satisfied:

$$\left(\frac{Re(\varepsilon_{metal})}{Re(\varepsilon_{metal}) + n_{eff}^2}\right)^{3/2}\frac{dn_{eff}}{dn_a} = sin\,\theta_a \quad (19)$$

(Where $n_{eff} = n_{eff}(n_G, n_{SP}, n_a, w, \Lambda, h)$ is a function of the grating parameters and bulk medium) the bulk refractive index sensitivity goes to zero. θ_a is the only parameter in the equation independent of the device, and can be optimized in combination with the device design, such that the device operates with zero bulk sensitivity in the RI of interest. The PEG-OQCM device in this paper is designed to minimize bulk RI sensitivity around RI = 1.33, the refractive index of DI water and salt solutions in which biosensing is performed.

4.3.3 Simulation Results

For the structure above, we calculate the reflection spectra using the rigorous coupled wave analysis (RCWA) method [83], with code written in MATLAB[84]. The device parameters used for the simulation are as follows: w = 700 nm, period Λ = 1395 nm, and total height h = 120 nm ($d_{SiO2,\ Grat}$ = 110 nm and $d_{TiO2,\ Adh}$ = 10 nm); spacer layer thicknesses $d_{SiO2,\ SP}$ = 15 nm, $d_{TiO2,\ SP}$ = 10 nm. An increase in protein thickness is modelled by a combination of increasing the protein thickness on top of the ridge and valley regions and increasing the duty cycle of the SiO_2 grating. The calculated reflection spectra of the PEG-OQCM in air and DI water at 45 degrees incidence angle (in the bulk medium) are plotted in Figure 4-2.

A reflectance dip in the optical spectrum is present in both spectra, which corresponds to the coupling of the incident wave to the surface plasmon at the metal-dielectric/bulk interface. In the case of air, multiple dips are present, corresponding to different grating orders supported by the structure. In water, there is only one grating order where the incident wave can couple to a surface plasmon – this is shown by the fact there is only one reflectance dip in the spectrum for RI = 1.33.

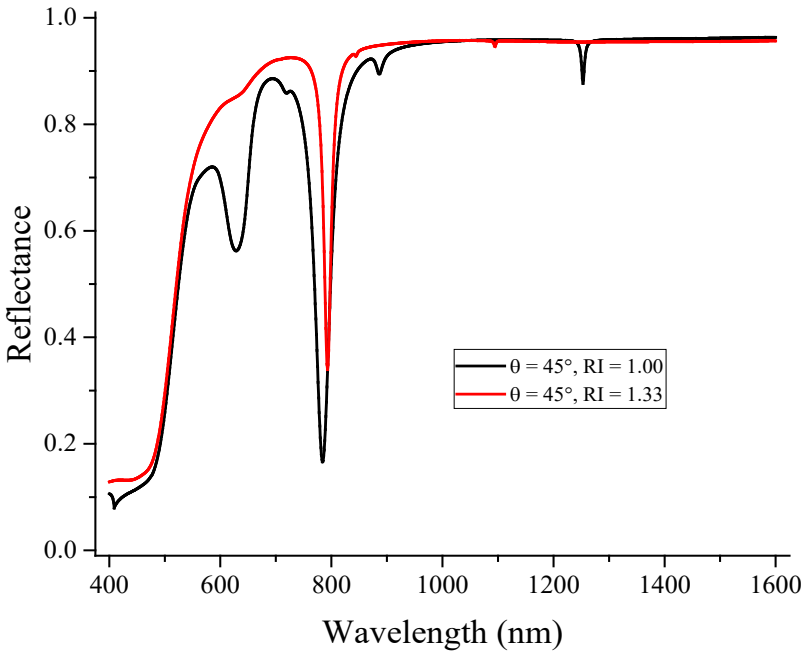

Figure 4-2 Comparison of the calculated reflection spectra of the PEG-OQCM in Air and Water

As the incidence angle is increased, the dip wavelength shifts toward shorter wavelengths due to the increasing contribution from the incident wavevector, as predicted by equation 13. Around θ = 45° and bulk RI = 1.33, the bulk RI sensitivity becomes zero, when the condition given by equation (14) is satisfied. The reflection spectra for $\theta = 45°$ for increasing bulk RI are plotted in Figure 4-4 to show this phenomenon.

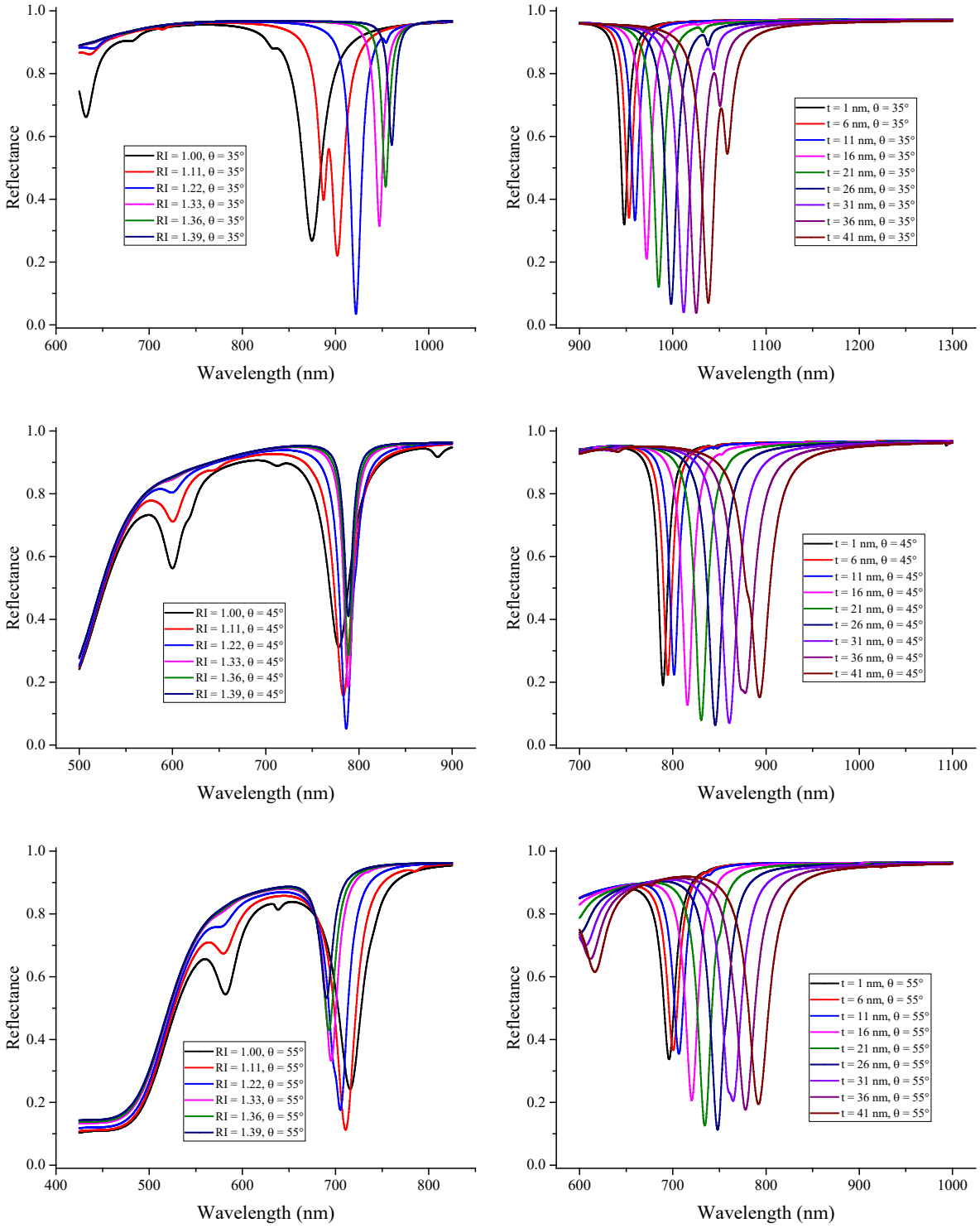

Figure 4-3 Effect of varying protein thickness and bulk refractive index - calculated reflection spectra for increasing bulk RI (left) and increasing biolayer thickness (right) for θ = 35°, 45°, and 55°° (top to bottom) for RI = 1.33. Note that the bulk refractive index sensitivity changes sign from positive to negative as the angle is increased

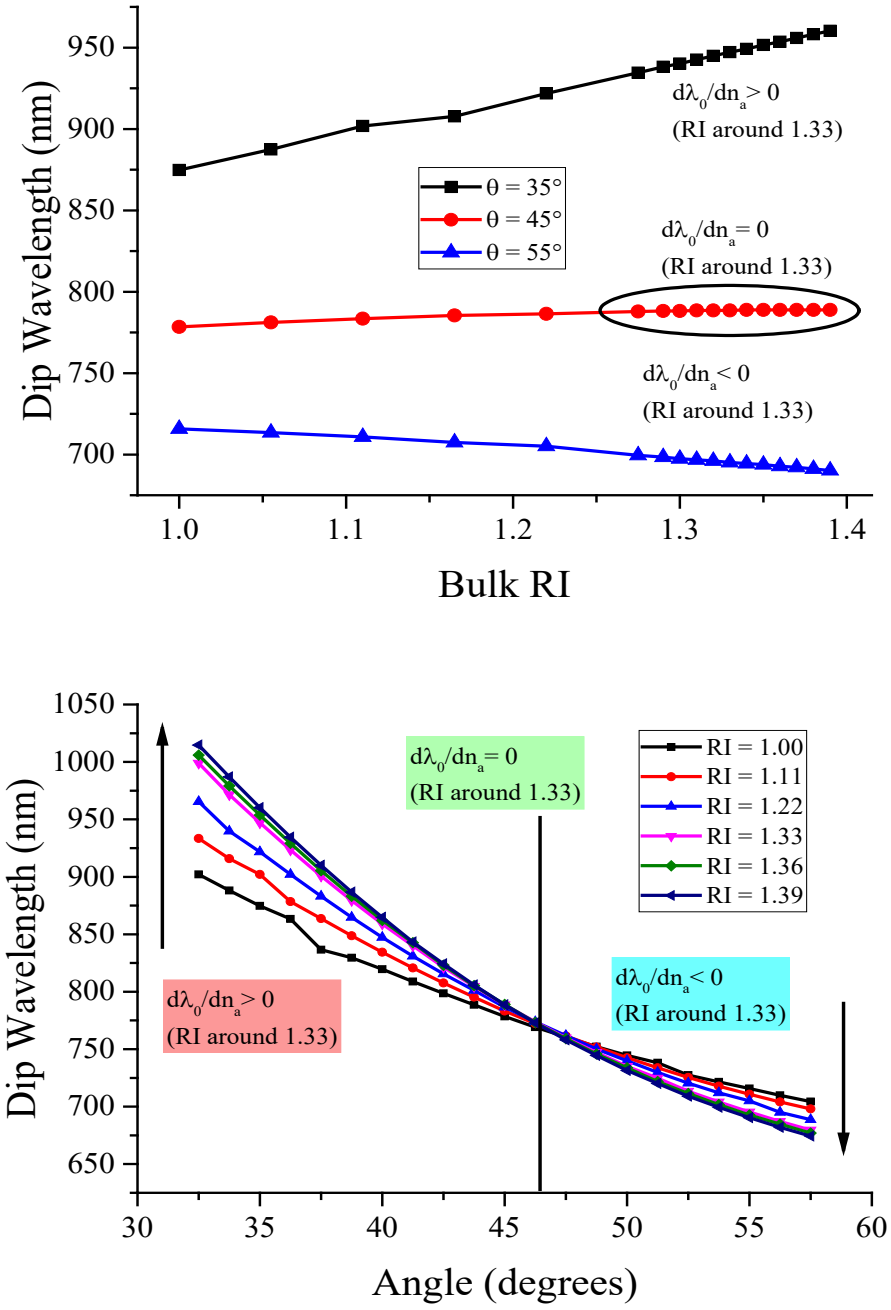

Figure 4-4 Dip wavelength vs. Bulk RI for varying incidence angles. Note that at an incident angle of 47 degrees, the bulk RI sensitivity approaches zero around bulk RI = 1.33

As the incidence angle is increased (Figure 4-4), the bulk refractive index wavelength sensitivity $d\lambda_0/dn_a$ for a fixed incidence angle changes sign from positive to negative. At a

certain angle (approximately 47 degrees for these device parameters), the bulk RI wavelength sensitivity at RI = 1.33 – corresponding to the intersection point of the different RI curves in Figure 4-4 - vanishes. As a result, any wavelength shift in the optical response at this angle can be attributed almost entirely to the accumulation of material on the surface of the grating, if the incidence angle is fixed at the optimal value.

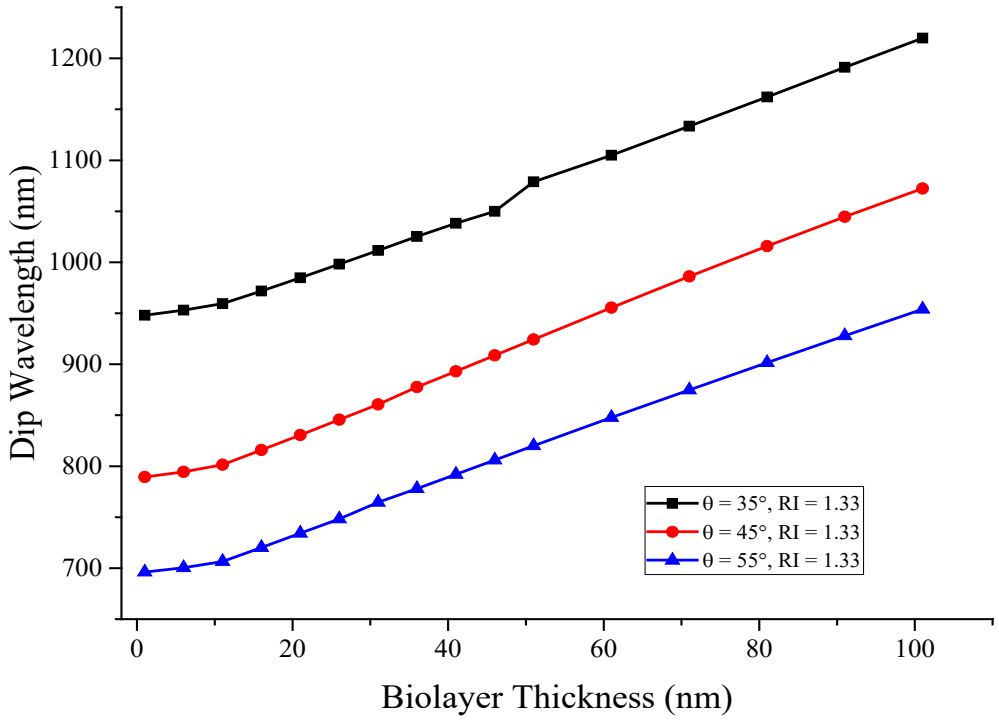

Figure 4-5 Dip Wavelength vs. Biolayer thickness in DI Water (RI = 1.33) at θ = 35°, θ = 45°, and θ = 55°

To determine the effect of incidence angle on surface sensitivity for biosensing applications, we simulate bio-molecular binding by increasing the width and height of the grating ridges while fixing the grating period. For a protein layer of refractive index 1.51, the surface sensitivity is calculated to be 2.1 nm/nm in air (RI = 1.00), and 1 nm/nm in DI water (RI = 1.33 – see Figure 4-5). Note that within this range, the surface sensitivity is relatively insensitive to incidence angle compared with that of the I-OQCM sensor. The narrow linewidth also makes single wavelength

tracking feasible in liquid, which is not easily done with the I-OQCM sensor. The simulation results are plotted in Figure 4-5.

For an experimental setup where the incidence angle for the material bordering the bulk medium is fixed, the wavelength shift is a function of two parameters: 1) the change in the incidence angle in the bulk liquid due to the refractive index change, and 2) the change resulting directly as a change of the bulk refractive index. In the biosensing experiment discussed later in this chapter, the shift for an RI change from 1.33 (DI water) to 1.362 (ethanol) is found to be 11 nm, when the incidence angle in water was calibrated to be approximately 45 degrees. For a refractive index change of $0.18 \cdot 5 \times 10^{-4}$ (corresponding to a 500 μg/mL solution of streptavidin in PBS), this corresponds to a wavelength shift of 9×10^{-3} nm, only 0.18% of the predicted 5 nm wavelength shift for a full monolayer of streptavidin on the grating. This shows that for biosensing applications, as long as the incidence angle in the material immediately before the bulk medium is near the optimal angle (crossover point), the impact of the bulk refractive index change is negligible even for a fixed external incidence angle (outside the bulk medium).

4.4 Device Fabrication

4.4.1 Base QCM Fabrication

The process for fabricating the base QCM for the PEG-OQCM sensor follows the same procedure as in Section 3.4.1 in Chapter 3, except that the Ta layer is replaced with gold from the Kurt J. Lesker Lab 18-2 sputterer.

4.4.2 Plasmonic Grating Fabrication

The key steps are illustrated in Figure 4-6. The first step is to deposit the planar spacer layers. The procedure for the spacer layers is similar to that for the interferometric layer in the I-OQCM structure, except the Si layer is replaced by 15 nm SiO_2/10 nm TiO_2, which are evaporated onto the wafer using the Angstrom Evaporator.

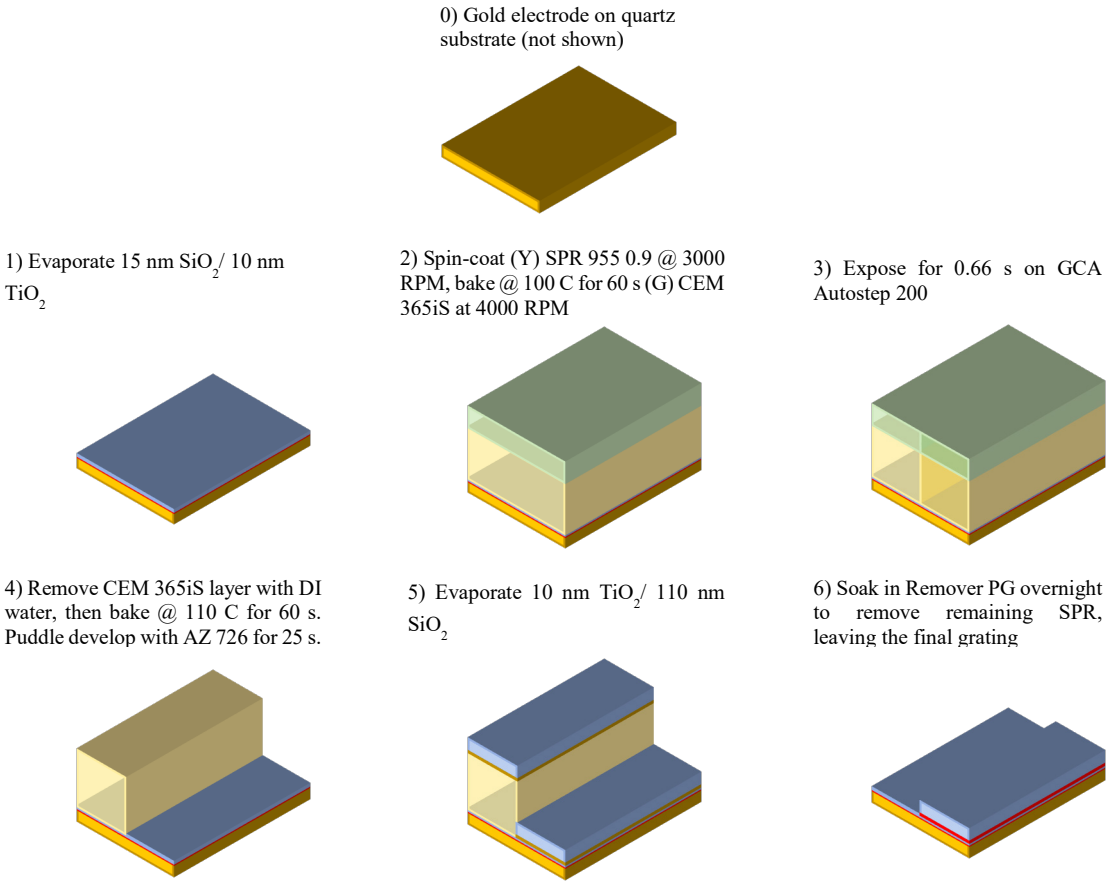

Figure 4-6 Fabrication process for plasmonically-enhanced grating layer

1) To fabricate the grating, the wafer is plasma cleaned for 180 seconds before being vapor primed with HMDS for 300 seconds using a YES Image Reversal Oven.

2) SPR 955 photoresist is then spun onto the wafer at 3000 RPM and soft-baked at 100°C for 60 seconds. Next, CEM 365iS (a contrast enhancement material (CEM)) is spun onto the wafer to enhance the sidewall profile and reduce diffusion effects during exposure.
3) Exposure is performed on a GCA Autostep for 0.66 seconds. The mask used for the grating was purchased from Compu-Graphics.
4) Next, the wafer is rinsed with DI water at 1000 RPM to remove the CEM, then baked at 110°C for 60 seconds before being puddle developed with AZ 726 for 25 s. The sample is plasma treated for 20 s at 60°C, 100 W RF Power, 35 sccm O_2 to remove residual photoresist.
5) 10 nm TiO_2/110 nm SiO_2 is evaporated onto the sample using an Angstrom Evaporator.
6) The photoresist is lifted off in Remover PG, then cleaned with IPA. Finally, the sample is cleaned with a 300 second plasma descum (100 W RF Power, 35 sccm O_2 on the YES Plasma Stripper) to remove any residual photoresist.

4.5 Experimental Setup and Procedure

4.5.1 Experimental Setup

The experimental setup (Figure 4-7) is the same as that in Section 3.5.1, consisting of two branches for each of the 2 measurement modes: one branch is used to monitor the mechanical response, and the other to monitor the optical response. The only difference is the device is now a PEG-OQCM.

For experiments conducted with a liquid medium (water, ethanol or phosphate buffered saline (PBS)), a prism is placed on top of the optical interrogation window to achieve 45 degrees

incidence angle in liquid. Index matching fluid of refractive index 1.52 is used between the prism and window to fill any potential air gaps.

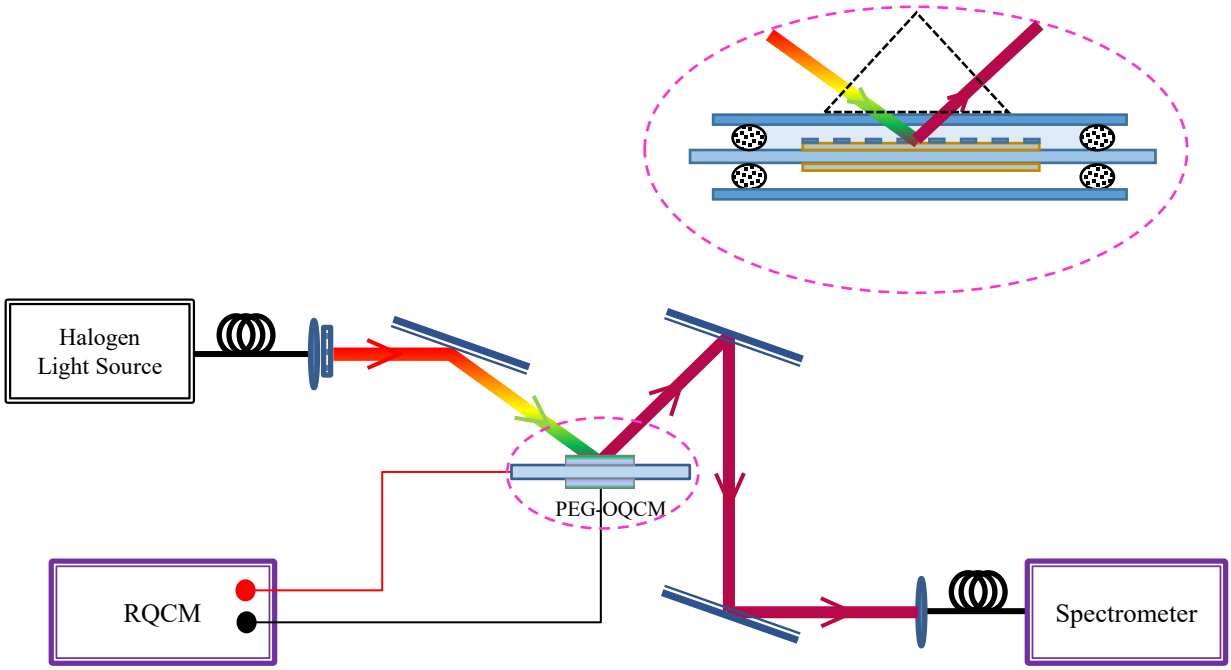

Figure 4-7 Experimental setup for the PEG-OQCM. White light from a fiber-coupled halogen light source is collimated with an asphere, then polarized and directed onto the OQCM sample. The reflected light is sent into a USB spectrometer. At the same time, the lead wires from the OQCM are connected via SMB connection to the RQCM machine to monitor the resonance frequency vs. time

4.5.2 Experimental Procedure

For mechanical and optical characterization, we follow the same procedure described in Section 3.5.2.

To demonstrate the PEG optical biosensing capability, a biosensing test is first performed on the PEG structure fabricated on a Si wafer. The Au thickness is much larger than the skin depth, such that the Au layer is effectively infinite for visible and NIR wavelengths.

The biotin-streptavidin system is chosen for this experiment for its high affinity. The sensor surface is first rinsed with ethanol, then a 1:1 v/v mixture of ethanol:HCl (1 N aqueous solution)

for 30 minutes to clean the surface, followed by a second ethanol rinse to remove the ethanol:HCl mixture. Next, a 5% solution of APTMS in ethanol is introduced to the sensor surface and allowed to incubate for 1.5 hours. The surface is then rinsed with ethanol to remove any unbound APTMS. The sensor is then baked at 70 C for a minimum of 45 minutes to cross-link the APTMS layer.

Next, the surface is rinsed with DI water. Phosphate buffered saline (PBS) (pH = 7.4, Gibco) is then introduced into the chamber to establish the baseline for the protein binding step(s). The PBS is then replaced with a solution of 0.5 mg/mL biotin in PBS and allowed to incubate for 1 hour. The biotin serves as a cross-linker between the silane layer and streptavidin. PBS is then flowed through the chamber to rinse any unbound biotin. Increasing concentrations of streptavidin in PBS are introduced, starting from 200 ng/mL, and allowed to incubate for 1 hour for each concentration. A 1-minute rinse step is added between the introduction of each new concentration to remove any unbound streptavidin.

4.6 Results and Discussion

4.6.1 Mechanical Characterization

Characterization of the mechanical response of the OQCM is performed using two instruments: the sensor response in the mechanical frequency domain is measured using an Agilent 43961A network analyzer, while the real-time frequency and resistance response of the sensor to liquid loading and vapor deposition and evaporation was measured using a RQCM machine from Maxtek Inc.

Table 6 shows the resonant frequency and calculated equivalent circuit parameters for the PEG-OQCM response in air, which are later used to characterize the PEG-OQCM liquid loading behavior.

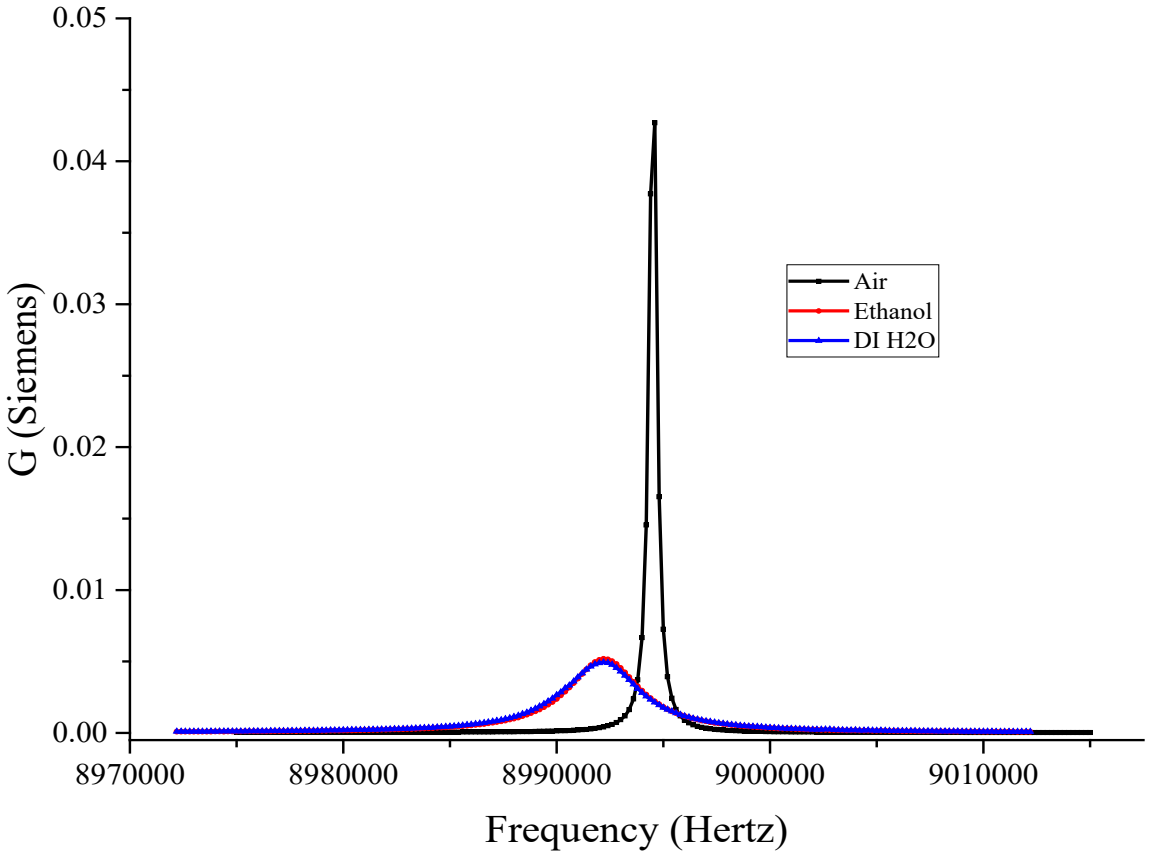

Figure 4-8 Mechanical frequency response of the PEG-OQCM in air, water and ethanol

Table 4-1 Calculated BVD circuit parameters of PEG-OQCM in air

	Resonant Frequency (MHz)	**Resistance R_1** (Ohms)	**Inductance L_1** (H)	**Capacitance C_1** (fF)
PEG-OQCM (Air)	8.9944501	25.90	0.0075402	41.52464

Table 4-2 contains the calculated equivalent circuit parameters obtained by fitting the data to the modified BVD circuit described in Chapter 1.

Table 4-2 Liquid Loading Response of PEG-OQCM and equivalent circuit elements

	$\mathbf{f_0}$ (MHz)	$\mathbf{\Delta f_0}$ (kHz)	$\mathbf{R_2}$ (Ohms)	$\mathbf{L_2}$ (μH)	$\boldsymbol{\rho\eta}$ (g^2/cm^4 s)	$\boldsymbol{\rho\eta}$ (expected) (g^2/cm^4 s)
PEG-OQCM (Air)	8.994450	0.000	0.0	0.000	0.0000	0.00000
PEG-OQCM (Ethanol)	8.992372	-2.078	177.1	3.486	0.01458	0.00890
PEG-OQCM (DI water)	8.991758	-2.950	193.1	4.515	0.02446	0.00816

The calculated density-viscosity product for DI water, using equation (6), exceeds that predicted by the model in [17] by 80% - a significant departure from the expected liquid loading frequency shift. This can be attributed to the increase in the effective surface roughness from the optical grating on the sensing area [85-87]. In Daikhin et al., the frequency shift for a given liquid as a function of the surface roughness is given by equation (20)[87] (in the limiting case where the rough layer is treated as having low permeability):

$$\Delta\omega = -\frac{\omega_0^2\rho}{\pi(\mu_q\rho_q)^{\frac{1}{2}}} Re\left\{\frac{1}{q_0} + \frac{L}{\xi_H^2 q_1^2} - \frac{1}{W}\frac{1}{\xi_H^2 q_1^2}\left[\frac{2q_0}{q_1}(\cosh(q_1 L) - 1) + \sinh(q_1 L)\right]\right\} \quad (20)$$

Where ρ is the liquid density, η the liquid viscosity, ξ_H the permeability length scale, ω_0 the crystal resonance frequency, ρ_q the quartz crystal density, and L the layer height.

For a quartz crystal of resonance frequency 9 MHz, the decay length in water for a planar surface is 186 nm. The height of the grating (120 nm) corresponds to 64 percent of the decay length. The calculated frequency shift is 2.4 kHz, which is slightly larger than the experimentally obtained value.

4.6.2 Optical Characterization

For the initial device characterization, the reflection spectra were measured for mixtures of ethanol/water at different ratios, with known refractive indices. To match the incidence angle for each medium, the angle in air was adjusted such that the angle in the bulk liquid would be the same for each substance. The spectra were measured using a Woollam 2000 ellipsometer. The spectra in air, DI water, phosphate buffered saline (PBS), and ethanol were also measured for a given incidence angle in air. The dip wavelengths were obtained from the reflection spectra in order to calculate the bulk refractive index wavelength sensitivity for a fixed external incidence angle. The reflection spectra are plotted in Figure 4-9, and the measured dip wavelengths in different media for a fixed external incidence angle (in air) are listed in Table 4-3.

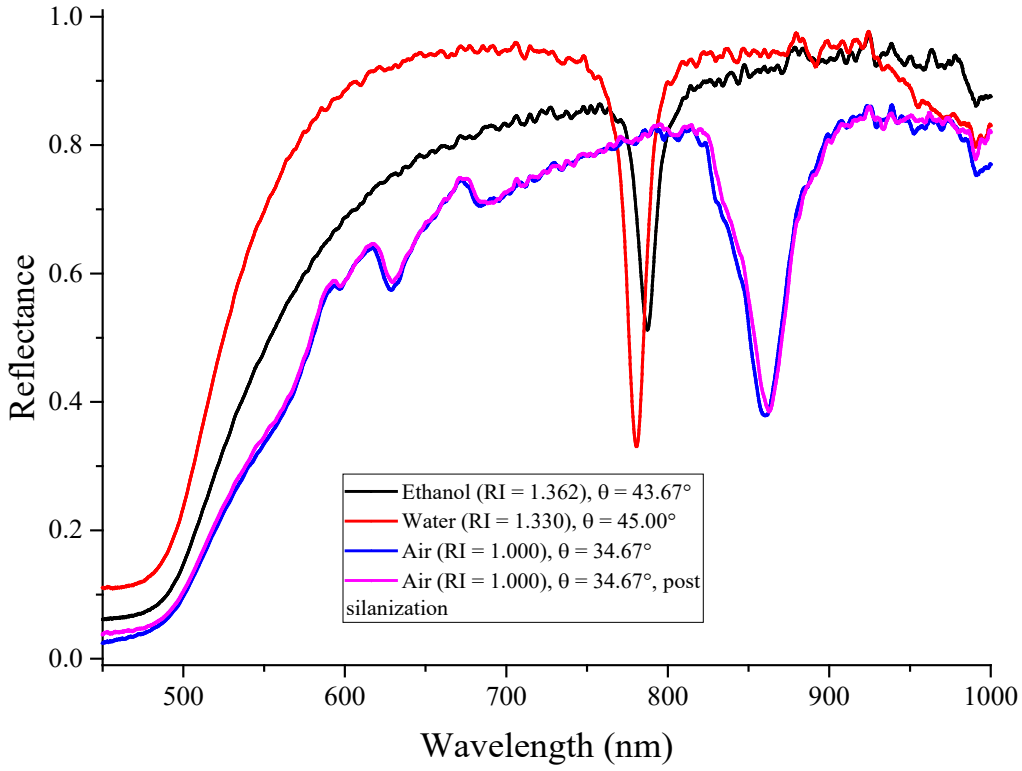

Figure 4-9 Optical Reflectance Spectra in Air, Ethanol, DI Water and Phosphate Buffered Saline (PBS)

Table 4-3 Dip wavelength in different media for fixed incidence angle in air

Medium	Angle in medium	Wavelength
Air	36.19	860.30
Water	46.27	780.63
Ethanol (RI = 1.362)	44.87	787.38

4.6.3 Mechanical Response to Vapor Deposition and Evaporation

To demonstrate the real-time mechanical sensing capability of the PEG-OQCM sensor, the sensor electrode pads are connected to the lead wires from the SMB cables to the RQCM. The sample is exposed to water vapor at irregular intervals, and the mechanical oscillation frequency and resistance are recorded by the RQCM. The real-time response is plotted in Figure 4-10. For each pulse in Figure 4-10, the condensation, equilibration absorption/diffusion and evaporation steps are clearly defined in the response. A detailed analysis is given in Section 4.6.6.

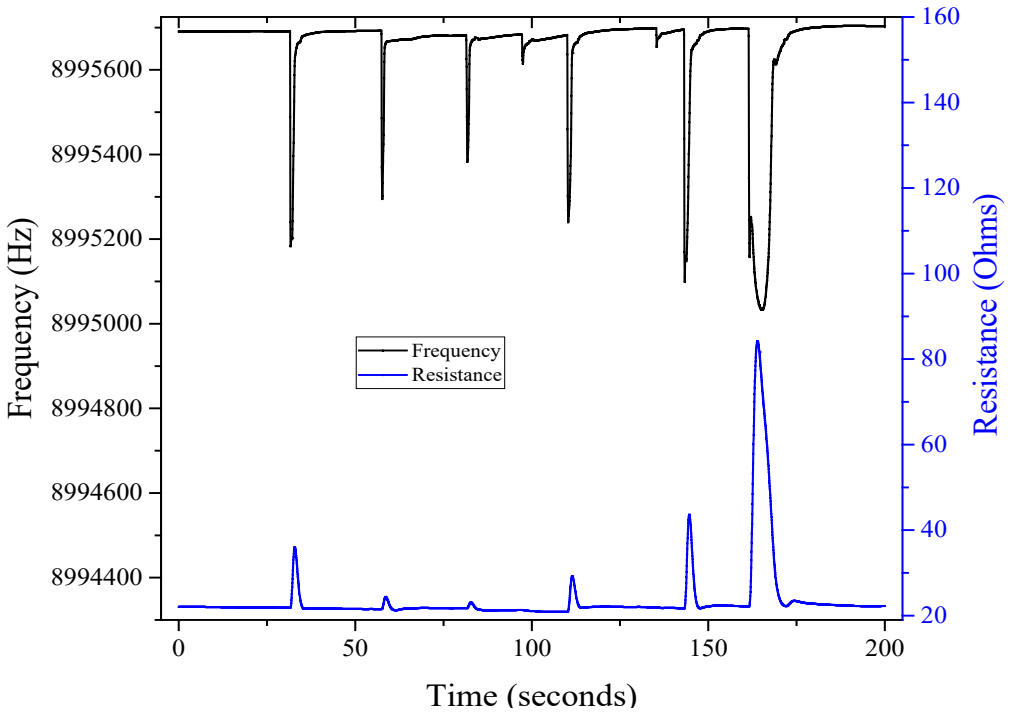

Figure 4-10 Real-time mechanical response to vapor deposition and evaporation at irregular intervals

4.6.4 Optical Response to Vapor Deposition and Evaporation

To verify the real-time optical sensing capability of the PEG-OQCM sensor, the sensor is placed into the sample mount for the optical setup. The sample is exposed to water vapor at irregular intervals, and the reflection spectrum is collected by the Ocean Optics spectrometer. The dip wavelength and reflectance (Figure 4-11) are extracted from the raw spectrum at each point in time, and the real-time response of the dip wavelength and reflectance are shown in Figure 4-12. A detailed analysis of the optical response is given in Section 4.6.6.

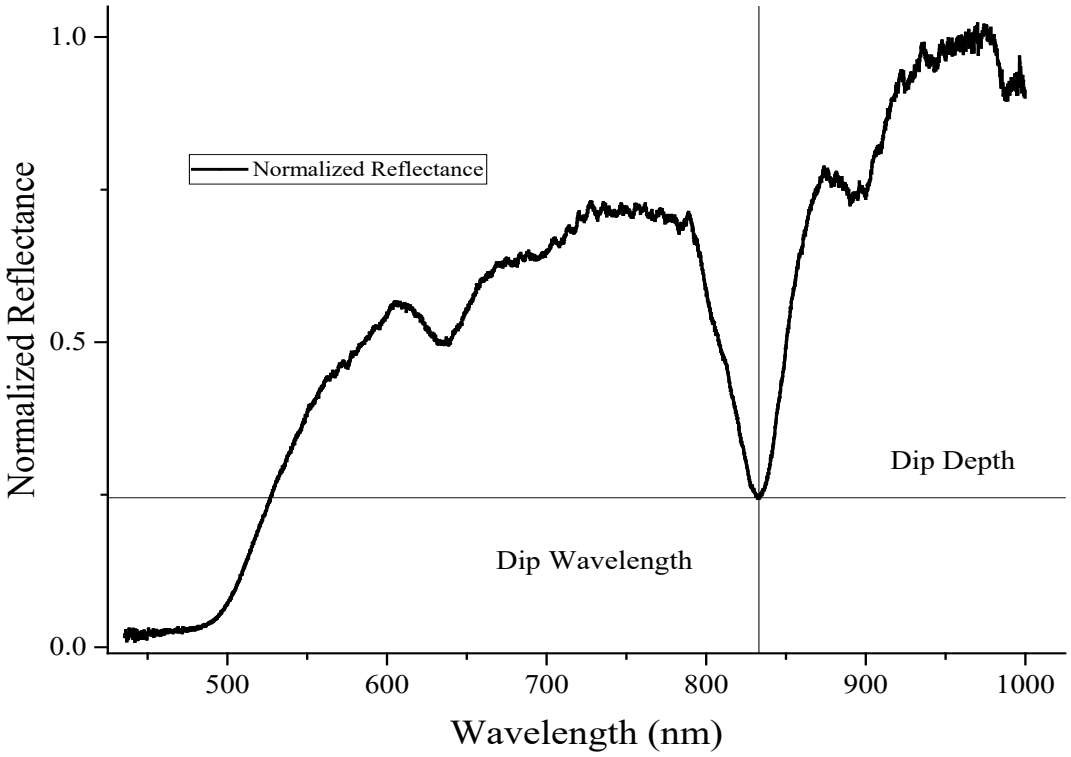

Figure 4-11 Reflection spectrum of the PEG-OQCM at 37 degrees. The parameters extracted from the optical spectra and plotted vs. time are indicated on the figure.

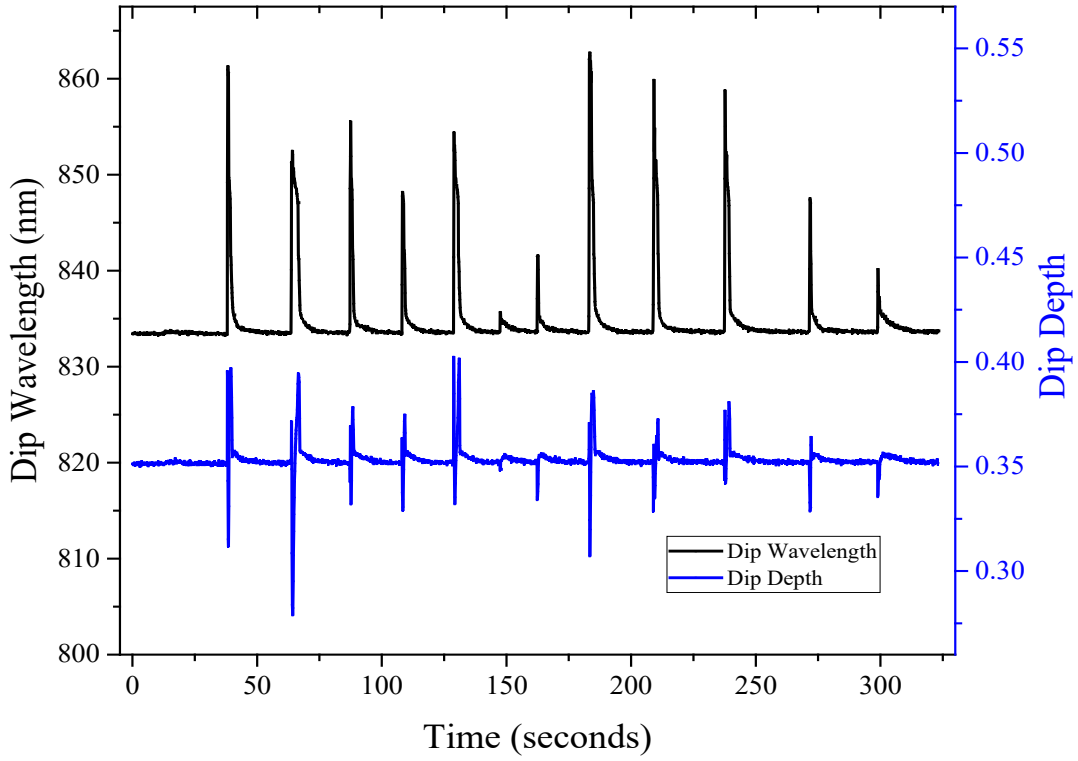

Figure 4-12 Real-time optical response to vapor deposition and evaporation at irregular intervals. The top figure shows the optical spectrum with lines indicating the two quantities, which are plotted in the bottom figure vs. time.

4.6.5 Biosensing Test – Optical

A biosensing experiment was also performed on a PEG sample fabricated on a silicon wafer using the procedure detailed in section 4.5.2. Optically, this sensor is identical to the structure fabricated on the QCM wafer (the Au layer is much thicker (100 nm) than the skin depth and can be treated as infinite for determining the optical response). The optical reflection spectra in air, ethanol, DI water, and phosphate buffered saline (PBS) were measured using the HL-4000 spectrometer (Ocean Optics).

From Figure 4-9, we can see that there is an 11 nm shift between the resonant dip wavelength for PBS and for ethanol. As shown in Section 4.3.3, this yields an expected change of 0.0009 nm for a 500 μg/mL solution of streptavidin, which is far below the expected 5 nm

wavelength shift due to protein binding. The effect of the bulk RI change is therefore negligible for this biosensing test.

The response of the system was calculated using the integrated response (IR), which is given[7] by equation (21):

$$IR = \sum_{\lambda=\lambda_1}^{\lambda=\lambda_2} \frac{I(\lambda) - I_0(\lambda)}{I_0(\lambda)} \tag{21}$$

Where $I(\lambda)$ is the intensity at wavelength λ, $I_0(\lambda)$ is the reference intensity at wavelength λ, and λ_1 and λ_2 are the lower and upper limits of the wavelength range for integration. For the biosensing experiment, $\lambda_1 = 759.90\ nm$ and $\lambda_2 = 780.25\ nm$. These limits are indicated in the reflection spectrum shown in Figure 4-13. $I_0(\lambda)$ is the reflectance spectrum for pure PBS, prior to the injection of 0.5 mg/mL biotin in PBS solution.

Table 4-4 Table showing the integrated response and wavelength shift after each step in the biosensing test

Step	**Integrated Response** (Step only)	**Integrated Response** (Total)	**Wavelength Shift (Gaussian fit, step only)** (nm)	**Wavelength Shift (Gaussian fit/Total)** (nm)
Biotin binding	7.37	7.37	0.75	0.75 (780.47 nm - 781.22 nm)
200 ng/mL streptavidin in PBS	1.07	8.44	0.12	0.87 (781.25 - 781.37 nm)
2 µg/mL streptavidin in PBS	8.22	16.66	0.92	1.79 (781.37 - 782.29 nm)
20 µg/mL streptavidin in PBS	19.24	35.90	1.66	3.45 (783.95 nm)

The integrated response during each step is plotted in Figure 4-14, and the total integrated response at the end of each step is listed in Table 4-4. The resonant wavelengths obtained from a Gaussian fit of the reflectance spectra are also included in Table 4-4 for comparison. The IR for

all steps are plotted sequentially in a single curve in Figure 4-15, and the reflection spectra at the end of each step are shown in Figure 4-16.

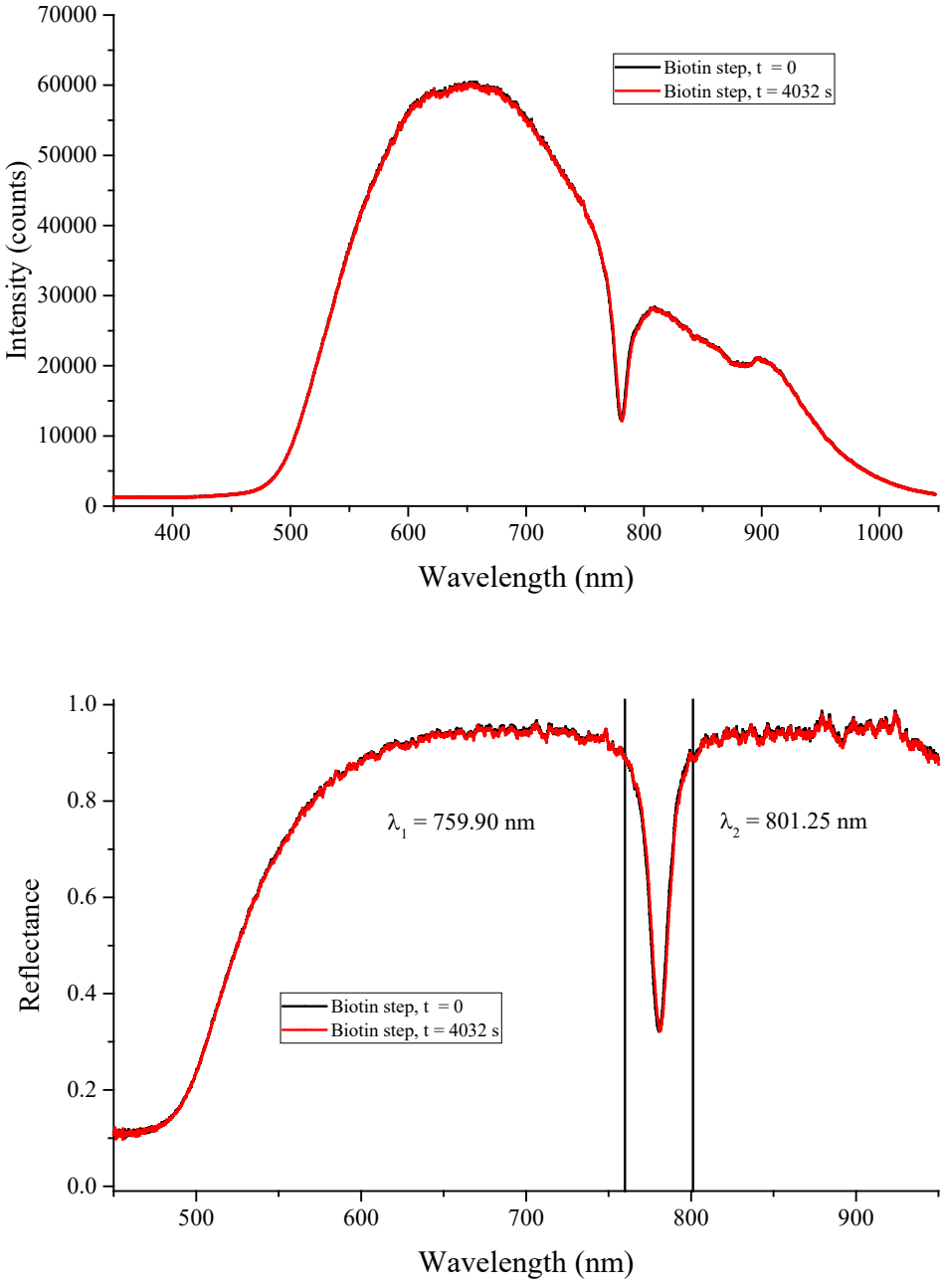

Figure 4-13 Intensity and Reflection Spectra at the beginning and end of the 0.5 mg/mL biotin binding step. The vertical lines show the wavelength range used for calculating the integrated response (IR) during each step

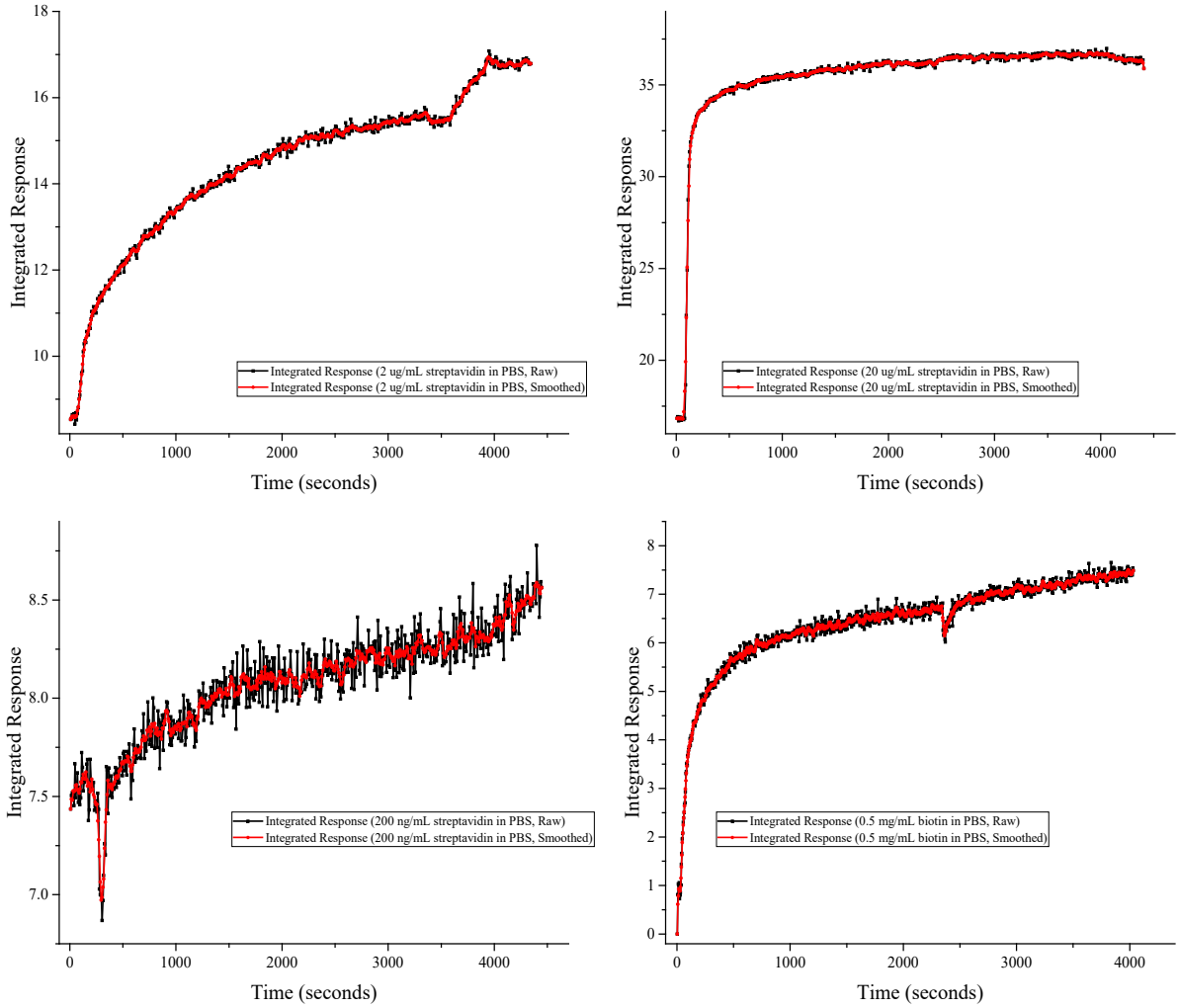

Figure 4-14 Integrated Response (IR) vs. time for the cross-linking and protein-binding steps. From Top to Bottom, Left to Right: 1) After 0.5 mg/mL biotin in PBS; 2) after 200 ng/mL streptavidin in PBS; 3) After 2 µg/mL streptavidin in PBS; 4) after 20 µg/mL streptavidin in PBS. Saturation of the response occurs after injection of the 20 µg/mL solution, as seen by the nonlinear increase in signal compared to the previous steps.

The size of a biotin molecule is 1.1 nm with a molecular weight of 443 Da, and approximately 5 nm for streptavidin with a molecular weight of approximately 55 kDa. From our simulations, for a 100 percent packed monolayer of streptavidin, the expected wavelength shift is

5 nm in a bulk medium with RI = 1.33. In our biosensing test, we observe a total of 3.12 nm shift at 20 µg/mL concentration, where the response has saturated. The observed shift is equivalent to a 60 percent coverage of the sample. The incomplete coverage could be due to the spacing between adjacent molecules, the number of binding sites on the biotin layer, and/or a portion of the streptavidin molecules being oriented randomly.

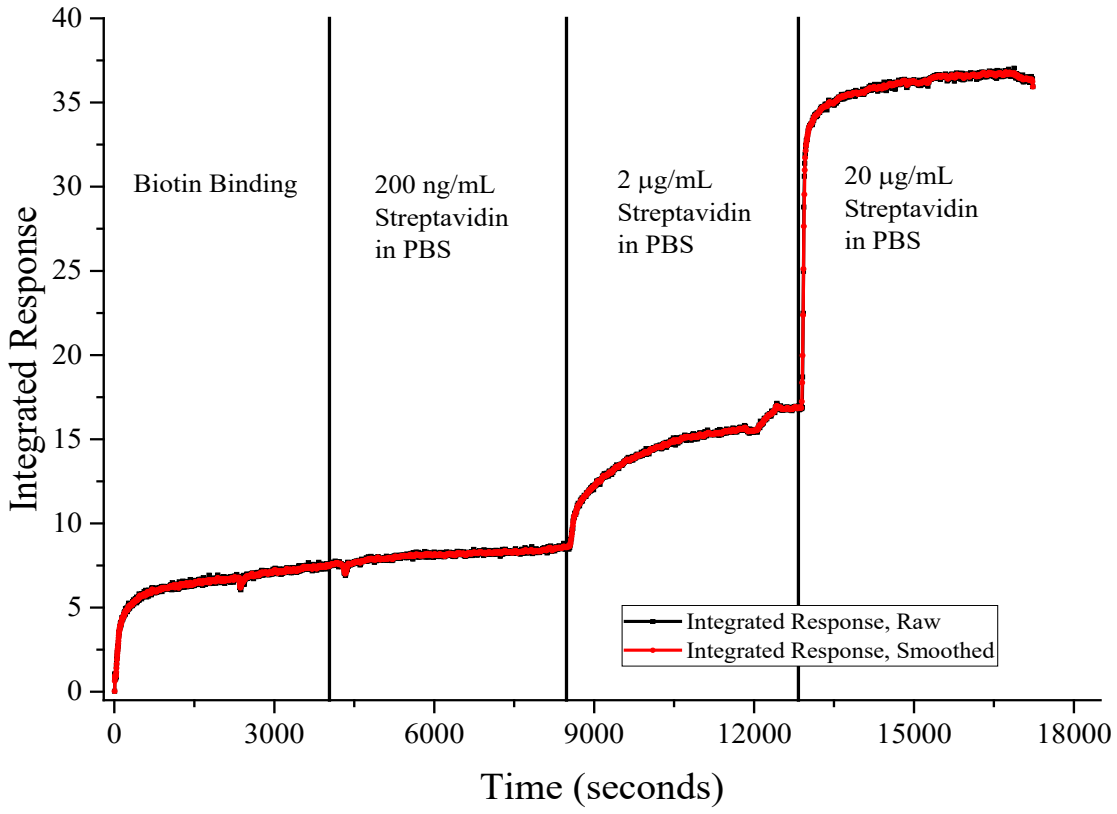

Figure 4-15 Integrated Response (IR) vs. time for all cross-linking and protein-binding steps. From Left to Right: 1) After 0.5 mg/mL biotin in PBS; 2) after 200 ng/mL streptavidin in PBS; 3) After 2 µg/mL streptavidin in PBS; 4) after 20 µg/mL streptavidin

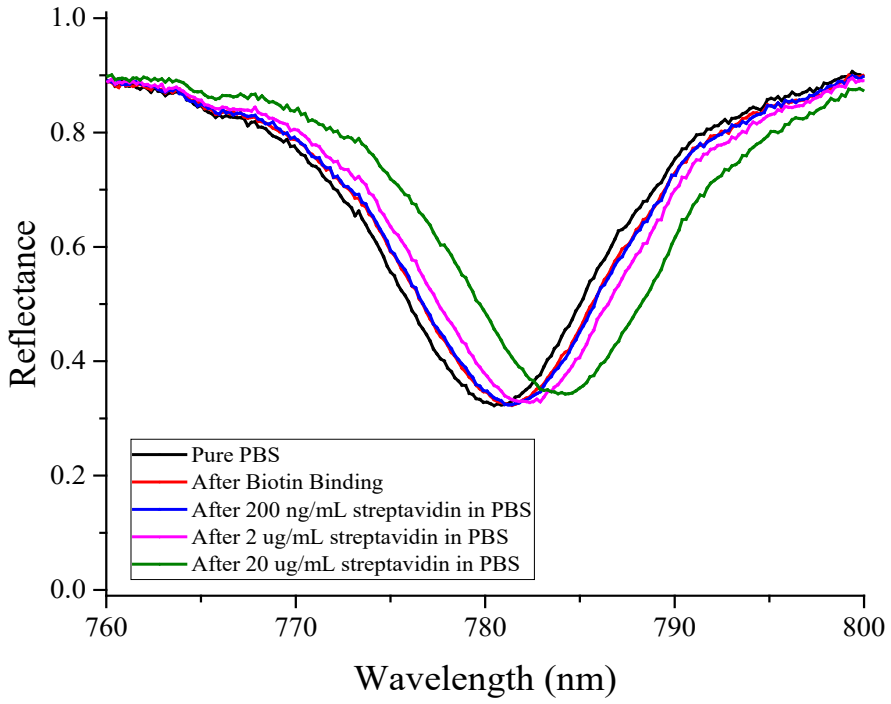

Figure 4-16 Reflectance spectra of the sensor at the end of each step. From Left to Right: 1) Phosphate Buffered Saline (PBS); 2) After 0.5 mg/mL biotin in PBS; 3) after 200 ng/mL streptavidin in PBS; 4) After 2 µg/mL streptavidin in PBS; 5) after 20 µg/mL streptavidin

4.6.6 Dual-Mode Measurement of Vapor Condensation and Evaporation

Next, dual-mode measurements of the PEG-OQCM were performed in air. The PEG-OQCM chip is secured into the fixture depicted in Figure 3-10. The optical spectrum was recorded using an Ocean Optics spectrometer with the following settings: 5 ms integration time, averaged over 3 scans. At the same time, the mechanical oscillation frequency and resistance are recorded using the Maxtek RQCM. The mechanical oscillation frequency, resistance, optical reflectance dip wavelength and dip depth response to irregular injections of water vapor are plotted in Figure 4-17. Figure 4-18 focuses on the details of the single vapor pulse between t = 105 seconds and t = 120 seconds.

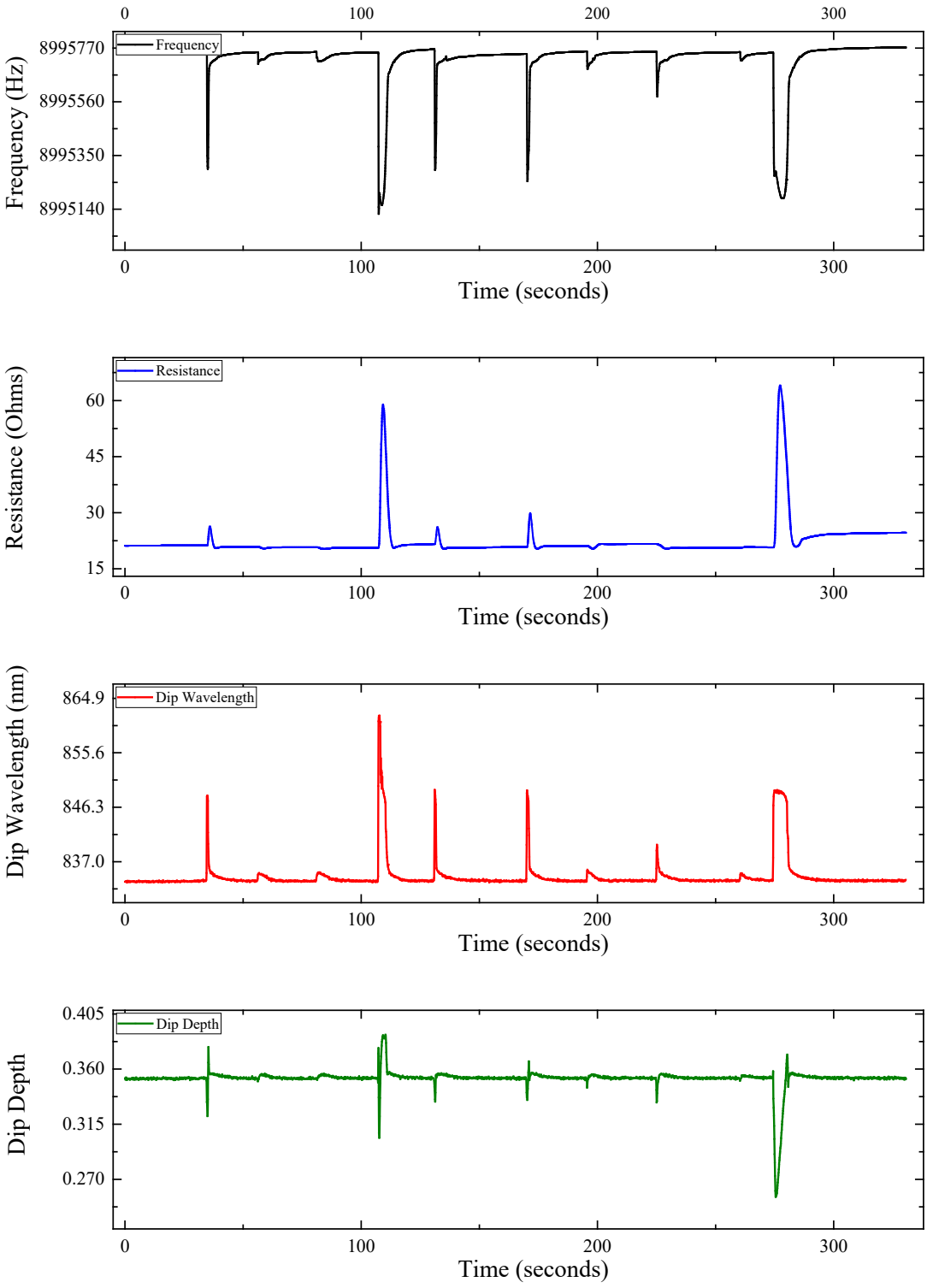

Figure 4-17 Frequency + Resistance vs. time and Dip Wavelength + Dip Depth vs. time for irregular injections of water vapor onto the PEG-OQCM surface

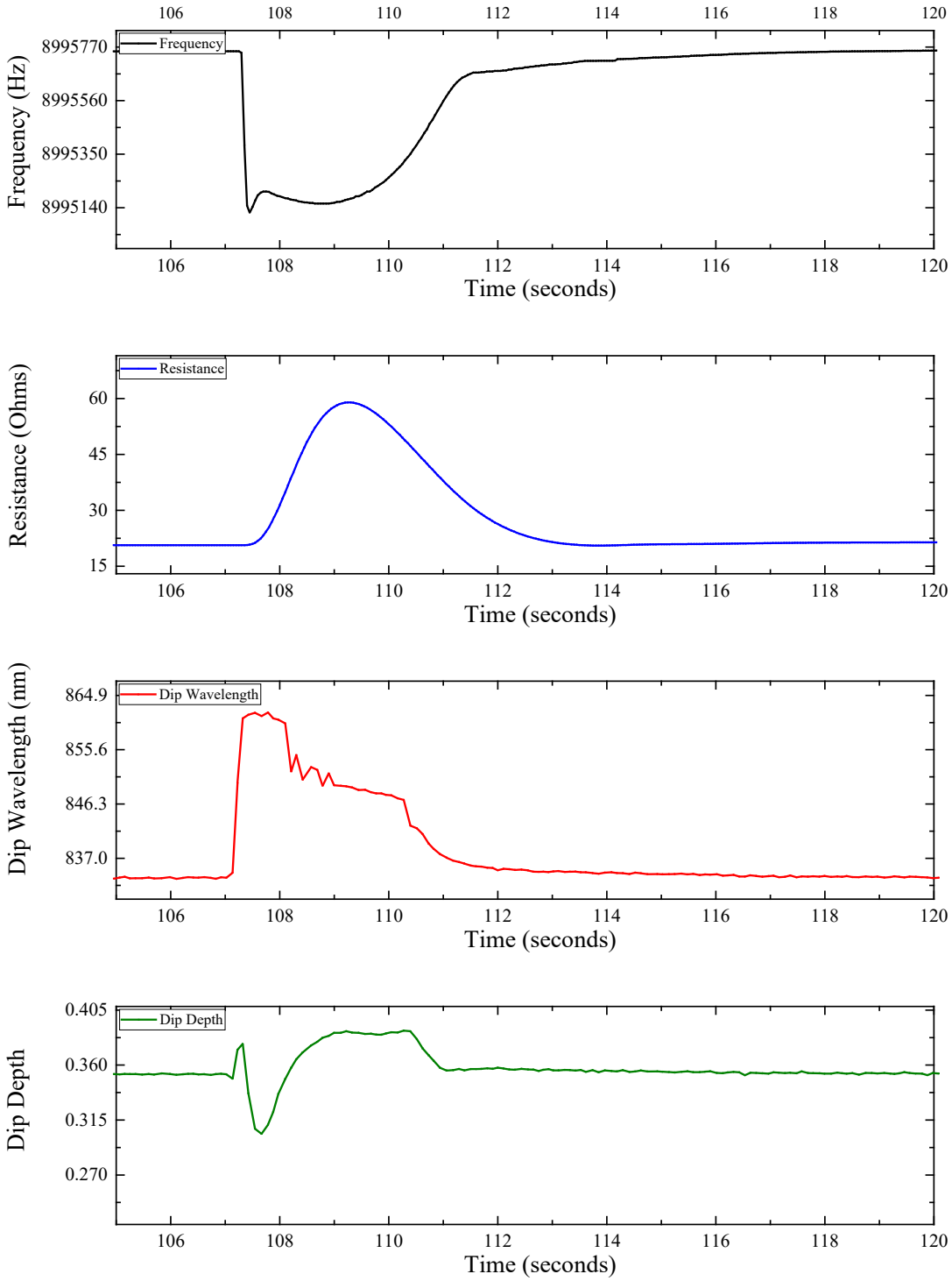

Figure 4-18 Plot of Frequency + Resistance vs. time and Dip Wavelength + Depth vs. time between 105 to 120 seconds

There is a clear correlation between the mechanical and optical response to water vapor condensation on the PEG-OQCM. A thin layer of dried ethanol residue is present on the PEG-OQCM, which adsorbs and releases water vapor from the air. To analyze the response of each mode, we focus on the injected vapor pulse between t = 107 seconds to t = 117 seconds. The response can be decomposed into the following stages:

1. Condensation (107.11 s – 107.47 s): Water vapor is introduced above the OQCM surface. As the humidity increases, the vapor starts to condense onto the PEG-OQCM surface due to 1) higher humidity, 2) higher temperature of the water vapor (breath).
    - Mechanical frequency **decreases** due to condensation of vapor on the surface (107.29 s – 107.47 s).
    - Mechanical resistance **remains constant, then increases slightly**, since the liquid layer here is thin enough such that the viscoelastic nature of water is not significant
    - Dip wavelength **increases** due to condensation of water vapor on the sensor surface.
    - Dip depth **increases, then decreases** as the vapor condenses onto the surface
2. Equilibration (107.47 s – 107.70 s): A small amount of the condensation on the OQCM surface evaporates to establish equilibrium with the water vapor above the sensor.
    - Mechanical frequency **increases** slightly due to condensed vapor evaporating back into the gas phase
    - Mechanical resistance starts to **increase** slowly as the ethanol film starts to absorb the condensed vapor
    - Dip wavelength **decreases** slightly as a small amount of the vapor film evaporates; at the same time, the ethanol film is starting to absorb the condensed vapor

- Dip depth **decreases** slightly as the vapor film thickness decreases

3. Absorption/Diffusion (107.70 s – 108.82 s): The condensed water, now in liquid phase, is absorbed by the ethanol film on the sensor surface. The viscoelastic nature of the water film becomes stronger here.
    - Mechanical frequency **decreases** due to vapor absorption by the ethanol film, increasing its viscoelasticity and inducing an additional frequency shift
    - Mechanical resistance **increases** due to vapor absorption by the rigid ethanol film, increasing its viscoelasticity and resulting in damping of the signal
    - Dip wavelength **decreases**: due to vapor absorption by the ethanol film. From 108.13 s - 108.82 s, there is a rapid exponential drop-off as the condensed vapor is rapidly absorbed by the ethanol film, reducing the optical thickness of the condensed vapor.
    - Dip depth **increases**
4. Evaporation (108.82 s – 120 s): The condensed vapor evaporates. The evaporation process occurs in two phases: in the first phase, the water vapor above the sensor is evaporating at the same time as the condensed vapor. This accelerates the evaporation process and corresponding response in the mechanical and optical parameters below. In the second phase, after all the vapor above the sensor is gone, the remaining adsorbed water evaporates back into the atmosphere at a slower exponential rate to re-establish equilibrium conditions.
    - Mechanical frequency **increases** due to a combination of evaporation from sensor surface and diffusion of absorbed vapor back to the sensor surface
    - Mechanical resistance **decreases** due to vapor evaporation (above sensor and from sensor surface) and diffusion of adsorbed vapor back to the sensor surface

- Dip wavelength **decreases** in two stages:
  1) (108.82 s – 110.28 s) Vapor evaporates from the space above the sensor. As a result, the condensed vapor on the sensor surface also evaporates, following the response of the space above the sensor. The absorption of the condensed vapor by the ethanol film limits the evaporation into the atmosphere, resulting in a slow decay of the dip wavelength.
  2) (110.28 s – 120.00 s) At this point, all vapor above the sensor surface has evaporated, and the decrease in the dip wavelength is due primarily to the condensed vapor evaporating from the surface.
- Dip depth **decreases** as the vapor film is evaporating from the sensor surface

5. Stabilization: The water vapor above the sensor has fully evaporated. The vapor on the sensor surface evaporates to re-establish initial conditions
   - Mechanical frequency **increases** towards the initial value
   - Mechanical resistance **decreases** back to the initial value
   - Dip wavelength **decreases** back to the initial value
   - Dip depth **decreases** back to the initial value

Fitting the data at the second evaporation "tail" to an exponential decay curve, a decay time constant of τ_{freq} = 2.4808 seconds for the mechanical frequency and τ_{WLPeak} = 2.5151 seconds for the dip wavelength is obtained during the final evaporation phase (using a single exponential fit).

4.7 Summary

The second structure, the PEG-OQCM, seeks to addresses two weaknesses of I-OQCM: An intrinsic tradeoff between reducing the linewidth of the optical reflection spectrum and increasing the wavelength sensitivity, and low-contrast interference pattern, by employing the plasmonic grating. The PEG-OQCM structure is fabricated using silicon dioxide, titanium dioxide and gold, and is completely exposed to the bulk medium. This makes our structure significantly more resistant to water absorption by the sensing medium, and more resistant to water trapping in cavities.

With this structure, a linewidth of 25 nm is obtained in air, 15 nm in water – up to 6 times narrower than that of SPR/LSPR (50-100 nm in water). The reflectance dip yields a depth of 60% and can be optimized further by including additional layers to the structure. Furthermore, the theory and simulation analyses indicate that the PEG-OQCM can achieve near zero sensitivity to the bulk refractive index by optimizing the incidence angle. Simulation results show that at an incident angle of 47 degrees, the bulk RI sensitivity becomes near zero around bulk RI = 1.33. The impact of the bulk refractive index change would be negligible. Experimental results in vapor deposition, water and biosensing (solution of streptavidin) match well with the simulation results.

Chapter 5: Optical Quartz Crystal Microbalance Array

5.1 Overview of Quartz Crystal Microbalance Array Sensors

The need for low-cost, simple-to-use sensors for biomedical applications ranging from health care to defense continues to grow. One of the most common approaches taken is fabricating multiple sensors onto a single chip for multiplexed detection.

Abe et al.[88], Kao et al.[89, 90] and Hung et al.[91] have fabricated multiple high-frequency QCM sensors on a single chip by etching the quartz wafer to define the QCM sensing areas. The unetched regions between each sensing area isolate the individual sensors. The thickness of the quartz wafer is reduced in the etched regions, resulting in a higher oscillation frequency. Jaruwongrunsee et al.[92] and Thies et al.[93] utilize polydimethylsiloxane (PDMS) walls to suppress interference in the multi-channel QCM and separate fluidic chambers. Jin et al.[94] and Tao et al.[95] took an alternative approach and fabricated multiple sensors on a chip without etching the original wafer, preserving the structural integrity of the crystal. In this case, the crystals are separated by a sufficient distance in order to minimize cross-talk[94, 95] between adjacent sensors[96, 97]. The last approach is used for the OQCM array in this chapter.

5.2 OQCM Array Device Structure

An OQCM array (OQCM-A) consists of multiple OQCM sensors and is fabricated on a single chip, enabling multiplexed multi-mode sensing on a single device. The OQCM-A structure

presented in this chapter has 3 I-OQCM sensors (described in Chapter 3) on a single wafer. Each sensing area is 5 mm in diameter. The individual I-OQCM sensors are arranged in an equilateral triangle, 5 mm apart to ensure that there is minimal cross-talk between the sensors.

5.3 Device Fabrication

The procedure used to fabricate the OQCM-A is the same as that used for the interferometric OQCM structure described in Chapter 3, except for the set of masks used to define the electrode and sensing areas – the masks for the OQCM-A define 3 I-OQCM sensors on the same chip. A fabricated OQCM-A sensor before and after wire bonding is shown in Figure 5-1.

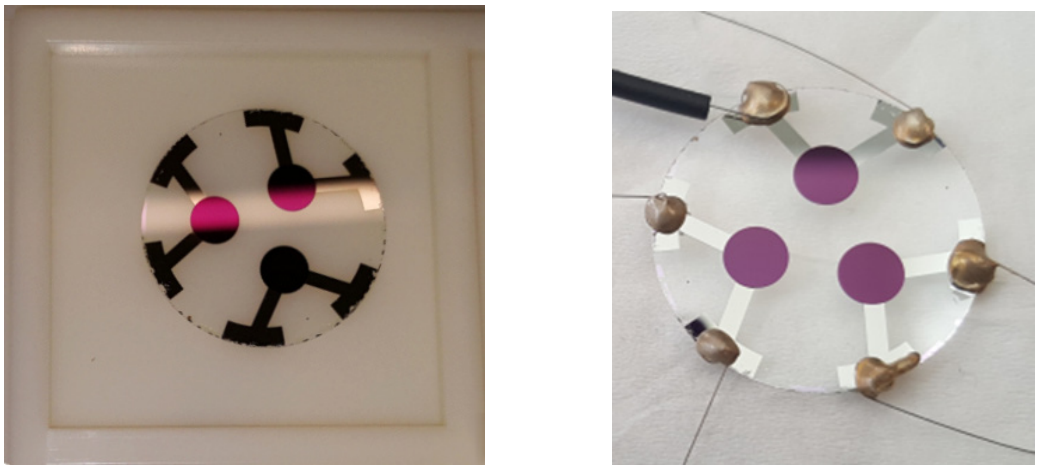

Figure 5-1 Fabricated OQCM-A sensor before (left) and after wire bonding (right)

5.4 Experimental Setup

The experimental setup for the OQCM array is similar to that of the single OQCM, with two additions:

1) For the optical branch of the setup, a beam expander (consisting of two lenses separated by the sum of their focal lengths) is placed between the first collimating lens and the polarizer, in order to illuminate all sensing areas.
2) For the mechanical branch, the electrodes on each I-OQCM sensor are connected in parallel to different channels on the RQCM.

5.5 Preliminary Results

For multiplexed dual-mode measurements, where each OQCM is treated as an individual sensor, calibration is needed to determine the mechanical resonance frequency for each sensor on the OQCM-A.

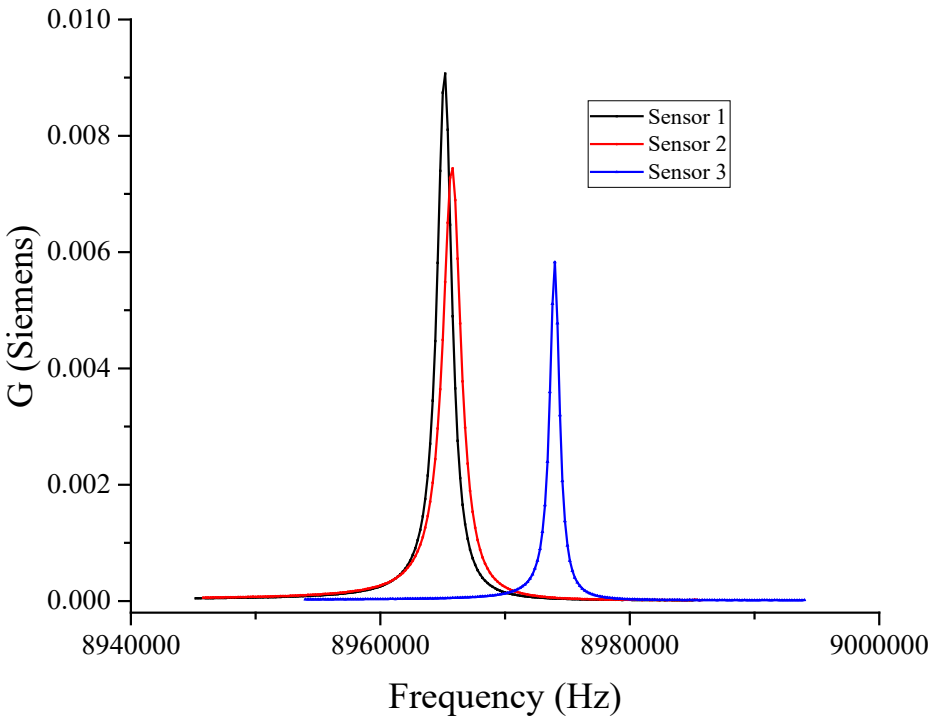

Figure 5-2 G vs. frequency plot of sensors 1, 2, and 3 on the I-OQCM array.

Tests were conducted using the Agilent network analyzer to obtain the G (conductance) vs. frequency curves for each sensor on the array. The results are plotted in Figure 5-2.

The results show that the resonance frequency for sensor 3 is separated by approximately 10 kHz from that of sensors 1 and 2. This may be due to a bonding issue with sensor 3, which in-turn affects the resistance, as seen by the lower peak conductance value (given by $1/R_1$), where R_1 is the mechanical resistance of the OQCM. This difference will not have an effect since the frequency shifts are measured relative to the base frequency of each individual sensor.

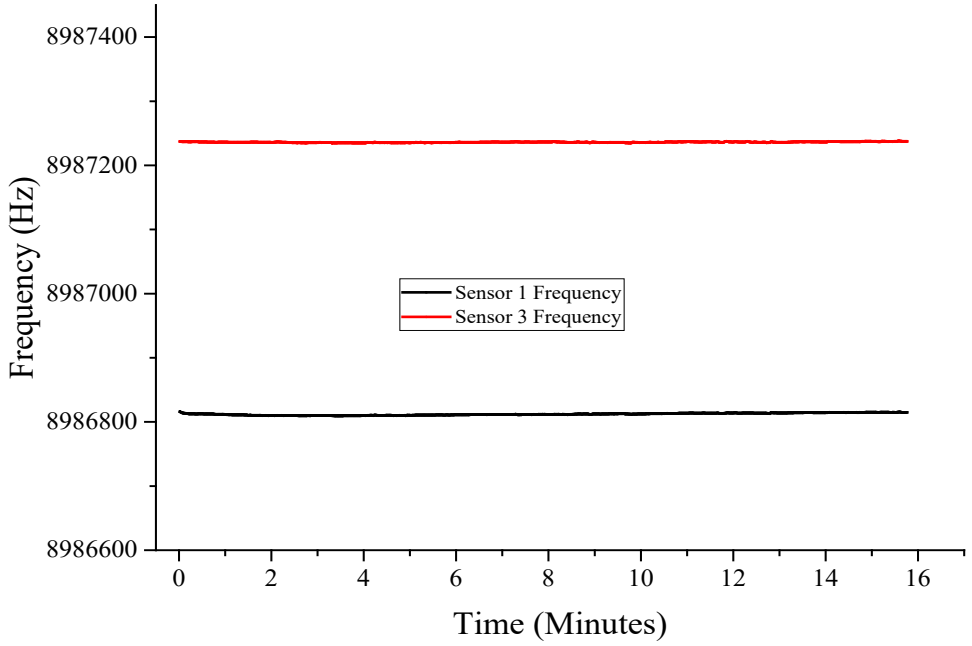

Figure 5-3 Stability test in air for bare Ta array to confirm sensor independence in the selected array layout

The key for successful operation of the OQCM-A is to ensure there is no cross-talk (or minimal) between any two sensors. To confirm the independence of the individual sensors in this array, a frequency stability test in air is performed on the Ta QCM array to show that the oscillation

of sensor 1 is unaffected by the oscillation of sensor 3. The results for the stability test in air (Figure 5-3) show that sensor 1 oscillates fully independently of sensor 3 in the absence of any loading.

To confirm that there was no cross-talk between adjacent sensors upon disturbance to a single sensor, tests were performed where one sensor was left exposed to air, while 4 microliters of DI water was pipetted onto the center of an adjacent sensor on the same chip. This test was performed for both the bare Ta array and the OQCM-A. The results (Figure 5-4) further validate the independence of each sensor.

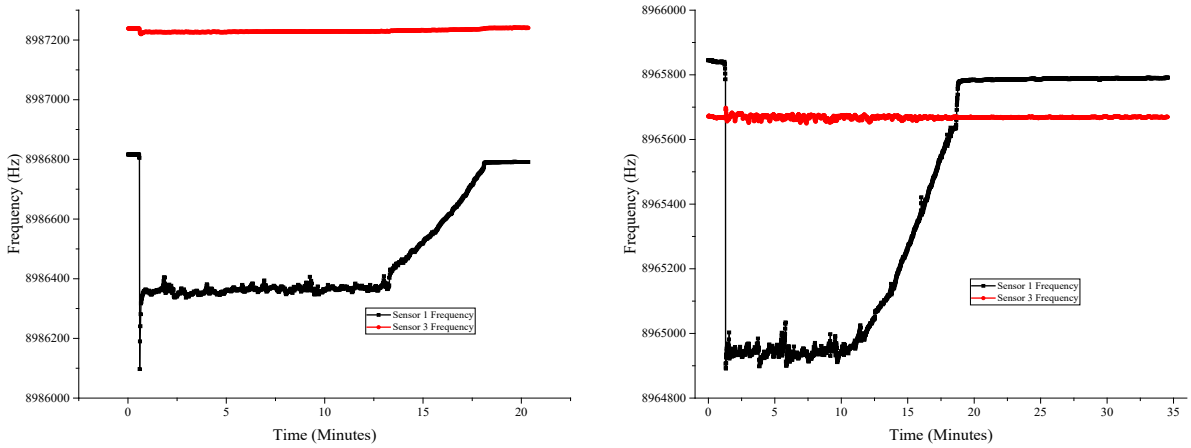

Figure 5-4 Liquid loading tests between two adjacent sensors. Left: Bare Ta sensor array - used to verify that the separation between sensors is sufficiently large to prevent cross-talk between sensors. Right I-OQCM array showing minimal cross-talk between sensors

5.6 Summary

The OQCM-A structure with 3 single I-OQCMs on a single chip was designed, fabricated and discussed in this chapter. Even though there is some variation between individual sensors due to variation during fabrication and assembly, each sensor can be characterized independently of the others. Mechanical response tests performed on the OQCM-A indicate that 1) each sensor responds independently of the other sensors; 2) the cross-talk between on adjacent sensors is

negligible. Each sensor on the OQCM-A can therefore be used as an independent dual-mode sensor for multiplexed multi-mode detection.

Chapter 6: Summary and Future Work

6.1 Summary

In this research project, we developed Optical Quartz Crystal Microbalance (OQCM) sensors that are capable of simultaneously measuring both optical and mechanical properties, while addressing the issues of similar existing sensors. Two types of single-OQCM structure were designed, fabricated and explored. The first structure is an interferometric OQCM sensor (I-OQCM) with a multilayer planar optical structure. The interference between reflections at the interfaces between layers generates an interference pattern in the optical spectrum that shifts upon accumulation of additional films on the structure. The common detection surface is the top of the multilayer structure. The I-OQCM is designed for top-side optical interrogation, which allows for monitoring of the distribution of binding material on the sensing surface.

The second structure is a plasmonically-enhanced grating OQCM sensor (PEG-OQCM), where the optical structure is a dielectric grating patterned on top of the electrode. The PEG-OQCM has a narrower optical response linewidth compared to standard SPR, while maintaining the same advantages as the I-OQCM. Additionally, the PEG-OQCM structure can be optically optimized to minimize the bulk refractive index sensitivity for a specific incidence angle, allowing the optical interrogation to decouple bulk and surface effects due to thin film accumulation. Simulation results show that at an incident angle of 47 degrees, the bulk RI sensitivity becomes near zero around bulk RI = 1.33. Experimental results for vapor deposition, water and biosensing

(of streptavidin to biotin) match well with the simulation results. With this PEG-OQCM structure, an optical linewidth of 25 nm was obtained in air, 15 nm in water – up to 6 times narrower than that of SPR/LSPR (50-100 nm in water).

The OQCM sensors were characterized separately to calibrate the operating parameters in each mode for each structure. Tests were performed in each mode under different conditions to demonstrate operation in air and liquid media, as well as biosensing capability. Dual-mode tests were then conducted for both the I-OQCM and PEG-OQCM to show the capability of simultaneous measurement of both optical and mechanical properties and responses of a system. The test results validate the simulation analyses and correlation between the optical and mechanical responses that would provide corroborating information for more reliable, robust cross-examination/confirmation for the evaluation of test systems.

OQCM-As with 3 I-OQCM sensors on a single quartz wafer were also designed, fabricated and tested for this project. The experimental data showing minimal cross-talk between adjacent sensors in air, and during liquid loading and evaporation validates the independence among sensors.

6.2 Next Steps/Future Work

For single I-OQCM and PEG-OQCM sensors:

Both sensors have successfully demonstrated dual-mode measurement capability under basic conditions. More biosensing tests need to be done on these sensors.

Some factors could have a significant impact on the sensor performance and are worth investigating further:

- Size and shape of the sensing area – one of the difficulties encountered is “dead volume”. Because the sizes of the input and output openings are smaller than the sensing diameter, some liquid from the previous step gets trapped inside the fluidic chamber (dead volume) and is difficult to remove. A smaller sensing area, properly shaped, would improve liquid flow to increase the efficiency.
- Optical incidence angle – the current experimental setup is fixed at an angle close to the optimized angle per simulations. The incidence angle can be optimized further through additional experiments to improve the device performance. One option is to have automated angle adjustment in real time to optimize/maximize the response via hardware and software to improve its performance.

For the OQCM-A:

- To construct fluidic chambers to perform multiplexed measurements on the OQCM arrays in dual optical and mechanical modes under liquid loading conditions.
- To optimize the distance among the single sensors on an array.

Bibliography

[1] X. Fan, I. M. White, S. I. Shopova, H. Zhu, J. D. Suter, and Y. Sun, "Sensitive optical biosensors for unlabeled targets: A review," *Analytica Chimica Acta,* vol. 620, pp. 8-26, 2008/07// 2008.

[2] S. Mukherji and N. Punjabi, "Label—Free Integrated Optical Biosensors for Multiplexed Analysis," *Journal of the Indian Institute of Science,* vol. 92, pp. 253-294, 2012/12/03/ 2012.

[3] A. J. Qavi, A. L. Washburn, J.-Y. Byeon, and R. C. Bailey, "Label-free technologies for quantitative multiparameter biological analysis," *Analytical and Bioanalytical Chemistry,* vol. 394, pp. 121-135, 2009/05// 2009.

[4] R. Monošík, M. Streďanský, and E. Šturdík, "Biosensors — classification, characterization and new trends," *Acta Chimica Slovaca,* vol. 5, pp. 109-120, 2012 2012.

[5] C. Ciminelli, C. M. Campanella, F. Dell'Olio, C. E. Campanella, and M. N. Armenise, "Label-free optical resonant sensors for biochemical applications," *Progress in Quantum Electronics,* vol. 37, pp. 51-107, 2013/03// 2013.

[6] G. Ruffato, G. Zacco, and F. Romanato, "Innovative Exploitation of Grating-Coupled Surface Plasmon Resonance for Sensing," in *Plasmonics - Principles and Applications*, K. Y. Kim, Ed., ed: InTech, 2012.

[7] Y. Gao, Z. Xin, B. Zeng, Q. Gan, X. Cheng, and F. J. Bartoli, "Plasmonic interferometric sensor arrays for high-performance label-free biomolecular detection," *Lab on a Chip,* vol. 13, pp. 4755-4764, 2013/11/12/ 2013.

[8] B. Zeng, Y. Gao, and F. J. Bartoli, "Differentiating surface and bulk interactions in nanoplasmonic interferometric sensor arrays," *Nanoscale,* vol. 7, pp. 166-170, 2015 2015.

[9] O. Avci, N. L. Ünlü, A. Y. Özkumur, and M. S. Ünlü, "Interferometric Reflectance Imaging Sensor (IRIS)—A Platform Technology for Multiplexed Diagnostics and Digital Detection," *Sensors,* vol. 15, pp. 17649-17665, 2015/07/20/ 2015.

[10] X. R. Cheng, G. G. Daaboul, M. S. Ünlü, and K. Kerman, "LED-based interferometric reflectance imaging sensor for the detection of amyloid-β aggregation," *Analyst,* vol. 139, pp. 59-65, 2013/11/25/ 2013.

[11] E. Özkumur, J. W. Needham, D. A. Bergstein, R. Gonzalez, M. Cabodi, J. M. Gershoni*, et al.*, "Label-free and dynamic detection of biomolecular interactions for high-throughput microarray applications," *Proceedings of the National Academy of Sciences,* vol. 105, pp. 7988-7992, 2008/06/10/ 2008.

[12] C. Hänel and G. Gauglitz, "Comparison of reflectometric interference spectroscopy with other instruments for label-free optical detection," *Analytical and Bioanalytical Chemistry,* vol. 372, pp. 91-100, 2002/01/01/ 2002.

[13] L. Tetard, A. Passian, R. H. Farahi, T. Thundat, and B. H. Davison, "Opto-nanomechanical spectroscopic material characterization," *Nature Nanotechnology,* vol. 10, p. 870, 2015/10// 2015.

[14] A. Janshoff, H.-J. Galla, and C. Steinem, "Piezoelectric Mass-Sensing Devices as Biosensors—An Alternative to Optical Biosensors?," *Angewandte Chemie International Edition,* vol. 39, pp. 4004-4032, 2000/11/17/ 2000.

[15] K. A. Marx, "Quartz Crystal Microbalance: A Useful Tool for Studying Thin Polymer Films and Complex Biomolecular Systems at the Solution−Surface Interface," *Biomacromolecules,* vol. 4, pp. 1099-1120, 2003/09/01/ 2003.

[16] C. K. O'Sullivan and G. G. Guilbault, "Commercial quartz crystal microbalances – theory and applications," *Biosensors and Bioelectronics,* vol. 14, pp. 663-670, 1999/12/01/ 1999.

[17] S. J. Martin, V. E. Granstaff, and G. C. Frye, "Characterization of a quartz crystal microbalance with simultaneous mass and liquid loading," *Analytical Chemistry,* vol. 63, pp. 2272-2281, 1991/10/15/ 1991.

[18] A. Arnau, Y. Jimenez, and T. Sogorb, "An extended Butterworth Van Dyke model for quartz crystal microbalance applications in viscoelastic fluid media," *IEEE Transactions on Ultrasonics, Ferroelectrics, and Frequency Control,* vol. 48, pp. 1367-1382, 2001/09// 2001.

[19] R. Konradi, M. Textor, and E. Reimhult, "Using Complementary Acoustic and Optical Techniques for Quantitative Monitoring of Biomolecular Adsorption at Interfaces," *Biosensors,* vol. 2, pp. 341-376, 2012/09/26/ 2012.

[20] J. Fang, C. Ren, T. Zhu, K. Wang, Z. Jiang, and Y. Ma, "Comparison of the different responses of surface plasmon resonance and quartz crystal microbalance techniques at solid–liquid interfaces under various experimental conditions," *Analyst,* vol. 140, pp. 1323-1336, 2015 2015.

[21] X. Su and J. Zhang, "Comparison of surface plasmon resonance spectroscopy and quartz crystal microbalance for human IgE quantification," *Sensors and Actuators B: Chemical,* vol. 100, pp. 309-314, 2004/05/15/ 2004.

[22] G. Diaconu and T. Schäfer, "Study of the interactions of proteins with a solid surface using complementary acoustic and optical techniques," *Biointerphases,* vol. 9, p. 029015, 2014/05/06/ 2014.

[23] E. Reimhult, C. Larsson, B. Kasemo, and F. Höök, "Simultaneous Surface Plasmon Resonance and Quartz Crystal Microbalance with Dissipation Monitoring Measurements of Biomolecular Adsorption Events Involving Structural Transformations and Variations in Coupled Water," *Analytical Chemistry,* vol. 76, pp. 7211-7220, 2004/12/01/ 2004.

[24] A. Baba, S. Tian, F. Stefani, C. Xia, Z. Wang, R. C. Advincula*, et al.*, "Electropolymerization and doping/dedoping properties of polyaniline thin films as studied by electrochemical-surface plasmon

spectroscopy and by the quartz crystal microbalance," *Journal of Electroanalytical Chemistry,* vol. 562, pp. 95-103, 2004/01/15/ 2004.

[25] M. F. Danışman and B. Özkan, "Simultaneous detection of surface coverage and structure of krypton films on gold by helium atom diffraction and quartz crystal microbalance techniques," *Review of Scientific Instruments,* vol. 82, p. 115104, 2011/11/01/ 2011.

[26] F. Liu, F. Li, A. N. Nordin, and I. Voiculescu, "A Novel Cell-Based Hybrid Acoustic Wave Biosensor with Impedimetric Sensing Capabilities," *Sensors,* vol. 13, pp. 3039-3055, 2013/03/04/ 2013.

[27] P. M. Kosaka, V. Pini, J. J. Ruz, R. A. d. Silva, M. U. González, D. Ramos*, et al.*, "Detection of cancer biomarkers in serum using a hybrid mechanical and optoplasmonic nanosensor," *Nature Nanotechnology,* vol. 9, p. 1047, 2014/12// 2014.

[28] K. Shinbo, H. Ishikawa, A. Baba, Y. Ohdaira, K. Kato, and F. Kaneko, "Fabrication of a Quartz-Crystal-Microbalance/Surface-Plasmon-Resonance Hybrid Sensor and Its Use for Detection of Polymer Thin-Film Deposition and Evaluation of Moisture Sorption Phenomena," *Applied Physics Express,* vol. 5, p. 036603, 2012/03/09/ 2012.

[29] M. A. Plunkett, Z. Wang, M. W. Rutland, and D. Johannsmann, "Adsorption of pNIPAM Layers on Hydrophobic Gold Surfaces, Measured in Situ by QCM and SPR," *Langmuir,* vol. 19, pp. 6837-6844, 2003/08/01/ 2003.

[30] A. Bund, A. Baba, S. Berg, D. Johannsmann, J. Lübben, Z. Wang*, et al.*, "Combining Surface Plasmon Resonance and Quartz Crystal Microbalance for the in Situ Investigation of the Electropolymerization and Doping/Dedoping of Poly(pyrrole)," *The Journal of Physical Chemistry B,* vol. 107, pp. 6743-6747, 2003/07/01/ 2003.

[31] Y. Zong, F. Xu, X. Su, and W. Knoll, "Quartz Crystal Microbalance with Integrated Surface Plasmon Grating Coupler," *Analytical Chemistry,* vol. 80, pp. 5246-5250, 2008/07/01/ 2008.

[32] A. Laschitsch, B. Menges, and D. Johannsmann, "Simultaneous determination of optical and acoustic thicknesses of protein layers using surface plasmon resonance spectroscopy and quartz crystal microweighing," *Applied Physics Letters,* vol. 77, pp. 2252-2254, 2000/09/26/ 2000.

[33] L. E. Bailey, D. Kambhampati, K. K. Kanazawa, W. Knoll, and C. W. Frank, "Using Surface Plasmon Resonance and the Quartz Crystal Microbalance to Monitor in Situ the Interfacial Behavior of Thin Organic Films," *Langmuir,* vol. 18, pp. 479-489, 2002/01/01/ 2002.

[34] A. L. Grab, A. Brink, M. Himmelhaus, and R. Dahint, "Integration of core/shell nanoparticle and QCM-D sensors in a single device: A new approach to the in situ detection of solvent content in thin adsorbed films with minimized response to spurious bulk refractive index changes," *Sensors and Actuators B: Chemical,* vol. 251, pp. 396-403, 2017/11/01/ 2017.

[35] J. Zhu, S. Huang, J. Ye, X. Zhang, and G. Liu, "Design of a quartz crystal with transparent electrode used for both QCM-D and LSPR technology," *Sensors and Actuators A: Physical,* vol. 229, pp. 141-146, 2015/06/15/ 2015.

[36] K. Shinbo, A. Uno, R. Hirakawa, A. Baba, Y. Ohdaira, K. Kato*, et al.*, "Fabrication of a Quartz-Crystal-Microbalance/Optical-Waveguide Hybrid Sensor and In situ Evaluation of Vacuum-Evaporated Lead Phthalocyanine Thin Film," *Japanese Journal of Applied Physics,* vol. 52, p. 05DC20, 2013/05/20/ 2013.

[37] K. Shinbo, S. Otuki, Y. Kanbayashi, Y. Ohdaira, A. Baba, K. Kato*, et al.*, "A hybrid humidity sensor using optical waveguides on a quartz crystal microbalance," *Thin Solid Films,* vol. 518, pp. 629-633, 2009/11/30/ 2009.

[38] K. B. Rodenhausen, T. Kasputis, A. K. Pannier, J. Y. Gerasimov, R. Y. Lai, M. Solinsky*, et al.*, "Combined optical and acoustical method for determination of thickness and porosity of transparent organic layers below the ultra-thin film limit," *Review of Scientific Instruments,* vol. 82, p. 103111, 2011/10/01/ 2011.

[39] K. B. Rodenhausen, M. Guericke, A. Sarkar, T. Hofmann, N. Ianno, M. Schubert*, et al.*, "Micelle-assisted bilayer formation of cetyltrimethylammonium bromide thin films studied with combinatorial spectroscopic ellipsometry and quartz crystal microbalance techniques," *Thin Solid Films,* vol. 519, pp. 2821-2824, 2011/02/28/ 2011.

[40] K. B. Rodenhausen, B. A. Duensing, T. Kasputis, A. K. Pannier, T. Hofmann, M. Schubert*, et al.*, "In-situ monitoring of alkanethiol self-assembled monolayer chemisorption with combined spectroscopic ellipsometry and quartz crystal microbalance techniques," *Thin Solid Films,* vol. 519, pp. 2817-2820, 2011/02/28/ 2011.

[41] E. Bittrich, K. B. Rodenhausen, K.-J. Eichhorn, T. Hofmann, M. Schubert, M. Stamm*, et al.*, "Protein adsorption on and swelling of polyelectrolyte brushes: A simultaneous ellipsometry-quartz crystal microbalance study," *Biointerphases,* vol. 5, pp. 159-167, 2010/12/01/ 2010.

[42] K. B. Rodenhausen and M. Schubert, "Virtual separation approach to study porous ultra-thin films by combined spectroscopic ellipsometry and quartz crystal microbalance methods," *Thin Solid Films,* vol. 519, pp. 2772-2776, 2011/02/28/ 2011.

[43] H. T. M. Phan, S. Bartelt-Hunt, K. B. Rodenhausen, M. Schubert, and J. C. Bartz, "Investigation of Bovine Serum Albumin (BSA) Attachment onto Self-Assembled Monolayers (SAMs) Using Combinatorial Quartz Crystal Microbalance with Dissipation (QCM-D) and Spectroscopic Ellipsometry (SE)," *PLOS ONE,* vol. 10, p. e0141282, 2015/10/27/ 2015.

[44] M. Koenig, T. Kasputis, D. Schmidt, K. B. Rodenhausen, K.-J. Eichhorn, A. K. Pannier*, et al.*, "Combined QCM-D/GE as a tool to characterize stimuli-responsive swelling of and protein adsorption on polymer brushes grafted onto 3D-nanostructures," *Analytical and Bioanalytical Chemistry,* vol. 406, pp. 7233-7242, 2014/11/01/ 2014.

[45] K.K and H. Photonics. (2018-03-12 22:46:07). *Spectroscopic / Light interferometry technology*. Available: http://www.hamamatsu.com/us/en/technology/innovation/spectroscopic/index.html

[46] "What is Ellipsometry? - J.A. Woollam," ed.

[47] N. Kananizadeh, C. Rice, J. Lee, K. B. Rodenhausen, D. Sekora, M. Schubert*, et al.*, "Combined quartz crystal microbalance with dissipation (QCM-D) and generalized ellipsometry (GE) to

characterize the deposition of titanium dioxide nanoparticles on model rough surfaces," *Journal of Hazardous Materials,* vol. 322, pp. 118-128, 2017/01/15/ 2017.

[48] M. Edvardsson, S. Svedhem, G. Wang, R. Richter, M. Rodahl, and B. Kasemo, "QCM-D and Reflectometry Instrument: Applications to Supported Lipid Structures and Their Biomolecular Interactions," *Analytical Chemistry,* vol. 81, pp. 349-361, 2009/01/01/ 2009.

[49] H. Guleryuz, I. Kaus, C. C. Buron, C. Filiâtre, N. Hedin, L. Bergström*, et al.*, "Deposition of silica nanoparticles onto alumina measured by optical reflectometry and quartz crystal microbalance with dissipation techniques," *Colloids and Surfaces A: Physicochemical and Engineering Aspects,* vol. 443, pp. 384-390, 2014/02/20/ 2014.

[50] C. C. Buron, C. Filiâtre, F. Membrey, H. Perrot, and A. Foissy, "Mass and charge balance in self-assembled multilayer films on gold. Measurements with optical reflectometry and quartz crystal microbalance," *Journal of Colloid and Interface Science,* vol. 296, pp. 409-418, 2006/04/15/ 2006.

[51] V. H. Niri, B. K. Flatt, Z. Fakhraai, and J. A. Forrest, "Simultaneous monitoring of electroformation of phospholipid vesicles by quartz crystal microbalance and optical microscopy," *Chemistry and Physics of Lipids,* vol. 163, pp. 36-41, 2010/01/01/ 2010.

[52] G. G. Daaboul, R. S. Vedula, S. Ahn, C. A. Lopez, A. Reddington, E. Ozkumur*, et al.*, "LED-based Interferometric Reflectance Imaging Sensor for quantitative dynamic monitoring of biomolecular interactions," *Biosensors and Bioelectronics,* vol. 26, pp. 2221-2227, 2011/01/15/ 2011.

[53] S.-H. Kim, W. Chegal, J. Doh, Hyun M. Cho, and Dae W. Moon, "Study of Cell-Matrix Adhesion Dynamics Using Surface Plasmon Resonance Imaging Ellipsometry," *Biophysical Journal,* vol. 100, pp. 1819-1828, 2011/04// 2011.

[54] L. Malic, B. Cui, M. Tabrizian, and T. Veres, "Nanoimprinted plastic substrates for enhanced surface plasmon resonance imaging detection," *Optics Express,* vol. 17, pp. 20386-20392, 2009/10/26/ 2009.

[55] D. Wang, L. Ding, W. Zhang, Z. Luo, H. Ou, E. Zhang*, et al.*, "A high-throughput surface plasmon resonance biosensor based on differential interferometric imaging," *Measurement Science and Technology,* vol. 23, p. 065701, 2012 2012.

[56] L. L. Chan, S. L. Gosangari, K. L. Watkin, and B. T. Cunningham, "A label-free photonic crystal biosensor imaging method for detection of cancer cell cytotoxicity and proliferation," *Apoptosis,* vol. 12, pp. 1061-1068, 2007/06/01/ 2007.

[57] B. Cunningham, P. Li, B. Lin, and J. Pepper, "Colorimetric resonant reflection as a direct biochemical assay technique," *Sensors and Actuators B: Chemical,* vol. 81, pp. 316-328, 2002/01/05/ 2002.

[58] B. Cunningham, B. Lin, J. Qiu, P. Li, J. Pepper, and B. Hugh, "A plastic colorimetric resonant optical biosensor for multiparallel detection of label-free biochemical interactions," *Sensors and Actuators B: Chemical,* vol. 85, pp. 219-226, 2002/07// 2002.

[59] M. Born and E. Wolf, *Principles of Optics Electromagnetic Theory of Propagation, Interference and Diffraction of Light*, 7 ed.: Cambridge University Press, 1999.

[60] W. S. M. Werner, K. Glantschnig, and C. Ambrosch-Draxl, "Optical Constants and Inelastic Electron-Scattering Data for 17 Elemental Metals," *Journal of Physical and Chemical Reference Data,* vol. 38, pp. 1013-1092, 2009/12// 2009.

[61] M. L. sheely, "Glycerol Viscosity Tables," *Industrial & Engineering Chemistry,* vol. 24, pp. 1060-1064, 1932/09/01/ 1932.

[62] R. Magnusson, H. G. Svavarsson, J. Yoon, M. Shokooh-Saremi, and S. H. Song, "Experimental observation of leaky modes and plasmons in a hybrid resonance element," *Applied Physics Letters,* vol. 100, p. 091106, 2012/02/27/ 2012.

[63] A. P. Hibbins, J. R. Sambles, and C. R. Lawrence, "Coupling of near-grazing microwave photons to surface plasmon polaritons via a dielectric grating," *Physical Review E,* vol. 61, pp. 5900-5906, 2000/05/01/ 2000.

[64] R. Magnusson and S. S. Wang, "New principle for optical filters," *Applied Physics Letters,* vol. 61, pp. 1022-1024, 1992/08/31/ 1992.

[65] K. G. Müller, M. Veith, S. Mittler-Neher, and W. Knoll, "Plasmon surface polariton coupling with dielectric gratings and the thermal decomposition of these dielectric gratings," *Journal of Applied Physics,* vol. 82, pp. 4172-4176, 1997/11/01/ 1997.

[66] S. R. Seshadri, "Quasi-optics of a planar dielectric waveguide with a dispersive substrate," *JOSA A,* vol. 15, pp. 1952-1958, 1998/07/01/ 1998.

[67] Y.-L. Liao, Y. Zhao, X. Zhang, and Z. Chen, "An ultra-narrowband absorber with a compound dielectric grating and metal substrate," *Optics Communications,* vol. 385, pp. 172-176, 2017/02/15/ 2017.

[68] W. K. Jung, N.-H. Kim, and K. M. Byun, "Development of a Large-Area Plasmonic Sensor Substrate with Dielectric Subwavelength Gratings Using Nanoimprint Lithography," *Journal of Biomedical Nanotechnology,* vol. 9, pp. 685-688, 2013/04/01/ 2013.

[69] K. M. Byun, S. J. Kim, and D. Kim, "Grating-coupled transmission-type surface plasmon resonance sensors based on dielectric and metallic gratings," *Applied Optics,* vol. 46, pp. 5703-5708, 2007/08/10/ 2007.

[70] J. Homola, "Present and future of surface plasmon resonance biosensors," *Analytical and Bioanalytical Chemistry,* vol. 377, pp. 528-539, 2003/10/01/ 2003.

[71] M. Abutoama and I. Abdulhalim, "Self-referenced biosensor based on thin dielectric grating combined with thin metal film," *Optics Express,* vol. 23, pp. 28667-28682, 2015/11/02/ 2015.

[72] M. Abutoama and I. Abdulhalim, "Angular and Intensity Modes Self-Referenced Refractive Index Sensor Based on Thin Dielectric Grating Combined With Thin Metal Film," *IEEE Journal of Selected Topics in Quantum Electronics,* vol. 23, pp. 72-80, 2017/03// 2017.

[73] A. Mizutani, S. Urakawa, and H. Kikuta, "Highly sensitive refractive index sensor using a resonant grating waveguide on a metal substrate," *Applied Optics,* vol. 54, pp. 4161-4166, 2015/05/01/ 2015.

[74] W. K. Jung, N.-H. Kim, and K. M. Byun, "Numerical study on an application of subwavelength dielectric gratings for high-sensitivity plasmonic detection," *Applied Optics,* vol. 51, pp. 4722-4729, 2012/07/10/ 2012.

[75] J. R. Vig and A. Ballato, "Comments on the effects of nonuniform mass loading on a quartz crystal microbalance," *IEEE Transactions on Ultrasonics, Ferroelectrics, and Frequency Control,* vol. 45, pp. 1123-1124, 1998/09// 1998.

[76] P. Li and F. Jin, "The anti-plane vibration of a quartz plate with an additional partial non-uniform mass layer for acoustic wave sensing," *Acta Mechanica,* vol. 224, pp. 1397-1414, 2013/07/01/ 2013.

[77] L. Macakova, E. Blomberg, and P. M. Claesson, "Effect of Adsorbed Layer Surface Roughness on the QCM-D Response: Focus on Trapped Water," *Langmuir,* vol. 23, pp. 12436-12444, 2007/11/01/ 2007.

[78] N. Bonod and J. Neauport, "Diffraction gratings: from principles to applications in high-intensity lasers," *Advances in Optics and Photonics,* vol. 8, pp. 156-199, 2016/03/31/ 2016.

[79] J. Dutta, S. A. Ramakrishna, and A. Lakhtakia, "Asymmetric coupling and dispersion of surface-plasmon-polariton waves on a periodically patterned anisotropic metal film," *Journal of Applied Physics,* vol. 117, p. 013102, 2015/01/05/ 2015.

[80] A. Demeter and S. Ruschin, "Back-reflecting interferometeric sensor based on grating coupler on a planar waveguide," 2015/07/14/ 2015.

[81] D. Rosenblatt, A. Sharon, and A. A. Friesem, "Resonant grating waveguide structures," *IEEE Journal of Quantum Electronics,* vol. 33, pp. 2038-2059, 1997/11// 1997.

[82] A. Sharon, S. Glasberg, D. Rosenblatt, and A. A. Friesem, "Metal-based resonant grating waveguide structures," *JOSA A,* vol. 14, pp. 588-595, 1997/03/01/ 1997.

[83] M. G. Moharam, E. B. Grann, D. A. Pommet, and T. K. Gaylord, "Formulation for stable and efficient implementation of the rigorous coupled-wave analysis of binary gratings," *JOSA A,* vol. 12, pp. 1068-1076, 1995/05/01/ 1995.

[84] *Download files*. Available: http://zhang-nano.gatech.edu/Rad_Pro.htm

[85] K. Rechendorff, M. B. Hovgaard, M. Foss, and F. Besenbacher, "Influence of surface roughness on quartz crystal microbalance measurements in liquids," *Journal of Applied Physics,* vol. 101, p. 114502, 2007/06/01/ 2007.

[86] L. Daikhin, E. Gileadi, G. Katz, V. Tsionsky, M. Urbakh, and D. Zagidulin, "Influence of Roughness on the Admittance of the Quartz Crystal Microbalance Immersed in Liquids," *Analytical Chemistry,* vol. 74, pp. 554-561, 2002/02/01/ 2002.

[87] L. Daikhin and M. Urbakh, "Effect of Surface Film Structure on the Quartz Crystal Microbalance Response in Liquids," *Langmuir,* vol. 12, pp. 6354-6360, 1996/01/01/ 1996.

[88] T. Abe and M. Esashi, "One-chip multichannel quartz crystal microbalance (QCM) fabricated by Deep RIE," *Sensors and Actuators A: Physical,* vol. 82, pp. 139-143, 2000/05// 2000.

[89] P. Kao, S. Doerner, T. Schneider, D. Allara, P. Hauptmann, and S. Tadigadapa, "A Micromachined Quartz Resonator Array for Biosensing Applications," *Journal of Microelectromechanical Systems,* vol. 18, pp. 522-530, 2009/06// 2009.

[90] P. Kao, D. Allara, and S. Tadigadapa, "Fabrication and performance characteristics of high-frequency micromachined bulk acoustic wave quartz resonator arrays," *Measurement Science and Technology,* vol. 20, p. 124007, 2009 2009.

[91] V. N. Hung, T. Abe, P. N. Minh, and M. Esashi, "Miniaturized, highly sensitive single-chip multichannel quartz-crystal microbalance," *Applied Physics Letters,* vol. 81, pp. 5069-5071, 2002/12/17/ 2002.

[92] K. Jaruwongrungsee, U. Waiwijit, A. Wisitsoraat, M. Sangworasil, C. Pintavirooj, and A. Tuantranont, "Real-time multianalyte biosensors based on interference-free multichannel monolithic quartz crystal microbalance," *Biosensors and Bioelectronics,* vol. 67, pp. 576-581, 2015/05// 2015.

[93] J. W. Thies, P. Kuhn, B. Thürmann, S. Dübel, and A. Dietzel, "Microfluidic quartz-crystal-microbalance (QCM) sensors with specialized immunoassays for extended measurement range and improved reusability," *Microelectronic Engineering,* vol. 179, pp. 25-30, 2017/07// 2017.

[94] X. Jin, Y. Huang, A. Mason, and X. Zeng, "Multichannel Monolithic Quartz Crystal Microbalance Gas Sensor Array," *Analytical Chemistry,* vol. 81, pp. 595-603, 2009/01/15/ 2009.

[95] W. Tao, P. Lin, Y. Ai, H. Wang, S. Ke, and X. Zeng, "Multichannel quartz crystal microbalance array: Fabrication, evaluation, application in biomarker detection," *Analytical Biochemistry,* vol. 494, pp. 85-92, 2016/02/01/ 2016.

[96] F. Shen, K. H. Lee, S. J. O'Shea, P. Lu, and T. Y. Ng, "Frequency interference between two quartz crystal microbalances," *IEEE Sensors Journal,* vol. 3, pp. 274-281, 2003/06// 2003.

[97] F. Shen and P. Lu, "Influence of interchannel spacing on the dynamical properties of multichannel quartz crystal microbalance," *IEEE Transactions on Ultrasonics, Ferroelectrics, and Frequency Control,* vol. 51, pp. 249-253, 2004/02// 2004.